Title
Stability, and Robustness of Three-dimensional Gaussian Vortices in a Rotating, Stratified, Boussinesq flow: Linear and Nonlinear Analyses

Author
Mahdinia, Mani

Publication Date
2017

Peer reviewed|Thesis/dissertation

Stability, and Robustness of Three-dimensional Gaussian Vortices in a Rotating, Stratified, Boussinesq flow: Linear and Nonlinear Analyses

by

Mani Mahdinia

A dissertation submitted in partial satisfaction of the

requirements for the degree of

Doctor of Philosophy

in

Engineering – Mechanical Engineering

in the

Graduate Division

of the

University of California, Berkeley

Committee in charge:

Professor Philip S. Marcus, Chair
Professor Ömer Savaş
Professor Tarek I. Zohdi
Professor Edgar Knobloch

Fall 2017

Stability, and Robustness of Three-dimensional Gaussian Vortices in a Rotating, Stratified, Boussinesq flow: Linear and Nonlinear Analyses

Abstract

Stability, and Robustness of Three-dimensional Gaussian Vortices in a Rotating, Stratified, Boussinesq flow: Linear and Nonlinear Analyses

by

Mani Mahdinia

Doctor of Philosophy in Engineering – Mechanical Engineering

University of California, Berkeley

Professor Philip S. Marcus, Chair

Large coherent vortices are the abundant features of geophysical and astrophysical turbulent flows. Here we explore and investigate a widely-used model for these vortices, that uses an axisymmetric Gaussian structure for pressure distribution. We discuss the linear stability of the vortices, their long-term evolution, and their robustness in the ocean. It has been suggested by other studies that these vortices can strongly affect their surroundings, for example by efficiently mixing and transporting heat, momentum, and material, and so understanding the dynamics of these vortices, such as their formation, robustness, and stability, is of great interest. The first chapter discusses the introductory material and summarizes the results of this work.

In the first part of this work (i.e., in chapter 2 of the thesis), the linear stability of three-dimensional (3D) vortices in rotating, stratified flows is studied by analyzing the non-hydrostatic inviscid Boussinesq equations. We have focused on a widely-used model of geophysical and astrophysical vortices, which assumes an axisymmetric Gaussian structure for pressure anomalies in the horizontal and vertical directions. For a range of Rossby number ($-0.5 < Ro < 0.5$) and Burger number ($0.02 < Bu < 2.3$) relevant to observed long-lived vortices, the growth rate and spatial structure of the most unstable eigenmodes have been numerically calculated and presented as a function of $Ro - Bu$. We have found neutrally-stable vortices only over a small region of the $Ro - Bu$ parameter space: cyclones with $Ro \sim 0.02 - 0.05$ and $Bu \sim 0.85 - 0.95$. However, we have also found that anticyclones in general have slower growth rates compared to cyclones. In particular, the growth rate of the most unstable eigenmode for anticyclones in a large region of the parameter space (e.g., $Ro < 0$ and $0.5 \lesssim Bu \lesssim 1.3$) is slower than 50 turn-around times of the vortex (which often corresponds to several years for ocean eddies). For cyclones, the region with such slow growth rates is confined to $0 < Ro < 0.1$ and $0.5 \lesssim Bu \lesssim 1.3$. While most calculations have been done for $f/\bar{N} = 0.1$ (where f and $\bar{N}$ are the Coriolis and background Brunt-Väisälä frequencies), we have numerically verified and explained analytically, using non-dimensionalized equations, the insensitivity of the results to reducing $f/\bar{N}$ to the more

ocean-relevant value of 0.01. The results of our stability analysis of Gaussian vortices both support and contradict findings of earlier studies with QG or multi-layer models or with other families of vortices. The results of this study provide a steppingstone to study the more complicated problems of the stability of geophysical (e.g., those in the atmospheres of giant planets) and astrophysical vortices (in accretion disks).

In the second part of this work (i.e., in chapter 3 of the thesis), the evolution and finite-amplitude stability of 3D vortices has been studied with an initial value code in a rotating stratified flow. Focusing on axisymmetric Gaussian vortices, the chapter 2 analysis showed, by analyzing the vortices' linear stability, that anticyclones have slower growth rates than those of cyclones. Here we examine the nonlinear stability for vortices that have growth rates faster than 50 turnaround times of the vortex, and for different finite amplitude perturbations (i.e., with different types, and/or amplitudes), for a range of Rossby number ($-0.5 < Ro < 0.5$) and Burger number ($0.07 < Bu < 2$), that are again relevant to the observations. We demonstrate that despite these vortices' fast growth rates, the perturbations quickly plateau – at a constant value, and the vortices usually have small-sized attracting basins (with only one vortex splitting radially, i.e., into tripoles), and for almost all cases we examined the initial and final equilibria remain close. For the non-splitting cases, the vortex's core always remains close to a Gaussian state. All the calculations here have been done for $f/\bar{N} = 0.1$, and effects of changing $f/\bar{N}$ is therefore forwarded to a future study. While we mostly use enstrophy measures to describe the vortex dynamics (i.e., as they evolve towards their final equilibria), we also show, for the vortices with close initial unperturbed and final equilibria, that their long-term evolution is represented entirely by a simple analytical solution, with the deviations from this representation shown to be small (that is after the flow reaches quasi-steady state). It should be noted as well that, while generally a fast instability growth rate can destroy a vortex via nonlinear finite-amplitude instabilities, it also is possible that the perturbations quickly saturate, such that the initial *unperturbed* and final equilibria remain close to each other. Our goal here has been to demonstrate the latter. Our explanation for the equilibria's robustness does not require a direct forcing mechanism; it only involves damping of velocity and density far from the initial conditions' position and at our numerically implemented sponge layers.

As far as the laws of mathematics refer to reality, they are not certain;
and as far as they are certain, they do not refer to reality.

A. Einstein

Contents

Acknowledgments

I had a truly great time as a Ph.D. student at UC Berkeley. I owe this great experience to a group of extraordinary people, and here I would like to try and thank them, or at least mention their contributions.

First, and foremost, I would like to thank my Ph.D. advisor Philip Marcus. Phil's passion, devotion, intellectual perception of reality, attention to detail, energy, and kindness, truly made him the greatest advisor that I could ever ask for. Not only he taught me how to do research, but also the basics of fluid mechanics, computation, math, and geophysical fluid dynamics. Specifically (and consistently), Phil showed me the way to examine new problems. I learned from Phil that to solve a problem often the simplest and most immediate approaches (but of course not too simple to not represent the reality) can be the most useful ones. This way of effective problem solving proved to be useful when I was a Ph.D. student, and I am sure, it will in the future. Phil was simply always there for me (as he is for most of the students in his lab), and for that I would like to thank him. For this wonderful experience, and what I learned during all this time, I am eternally grateful.

I am very grateful to my old labmate Chung-Hsiang Jiang. Rather than telling me what to do, Chung-Hsiang's help and advice (that is during the time we worked together) was mostly on what not to do. That is why I always thought of him as an older brother; one whose help was indispensable to me. Of course, I also learned from him about computation, research, and math, which in fact was very useful during the later steps of this work. I would like to thank my other old labmate Meng Wang, who was at times very hard on me (specially during our few last years together). Nevertheless his help always motivated me to strive for perfection, and as such I am very thankful to him. I also am thankful to my other old labmate Sahuck Oh, for being a truly great colleague in the lab, and also a good friend during our time together.

The first course for which I was a graduate student instructor (GSI) was Phil's ME106 – fluid mechanics course. After that I was the GSI, reader, or instructor, for several courses (i.e., that include CE100 – elementary fluid mechanics; ME120 – computational biomechanics across multiple scales; BioE10 – introduction to biomedicine for engineers; BioE104 – biological transport phenomena; MSE113 – mechanical behavior of engineering materials; and Math53 – multivariable calculus). I would like to thank these courses' instructors, Tina Chow, Mohammad Mofrad, Terry Johnson, Aaron Streets, and Robert Ritchie; with whom I worked closely, when I was the courses' GSI, or reader. I would also like to thank my students from whom I learned quite a lot, and I hope that I had a positive effect on their scientific development and well-being.

Much appreciation goes to the members of my qualifying exam and dissertation committees: Ömer Savaş, Tarek Zohdi, Reza Alam, James Sethian, and Edgar Knobloch. I am grateful to Edgar for his comments on my dissertation.

I would like to thank Ömer Savaş, for teaching me fluid mechanics, for several courses that I had with him, and also for chairing my qualifying exam. I am grateful to Reza Alam for teaching me about wave dynamics, and for his advice and support over the times that

we met. I truly enjoyed and learned from the great courses I took in UC Berkeley, and so I would like to thank George Johnson, Tarek Zohdi, James Sethian, Francisco Grünbaum, and David Steigmann for them.

I would like to thank the current and former members of our lab: Joe Barranco, Pedram Hassanzadeh, Suyang Pei, Caleb Levy, Nelson Chen, Chiyu Jiang, Andrew Sanville, Anzhu Sun, Haris Moazam Sheikh, and Aidi Zhang. Specifically, I am grateful to Joe for providing the Spectral parallel code that I used (and modified) for my Ph.D. research. I would like to thank Pedram, for helping me choose my thesis' topic, for his contribution in preparing the first part of this work, and for his advice and support throughout the years. I am also grateful to Suyang for his help and support at the beginning of my Ph.D., and to Caleb for helping run and post-process some of the simulations. I appreciate scholarships and fellowships I received from Graduate Division Block Fellowship, and Jonathan Laitone Memorial Scholarship.

I would like to thank my Bachelor's and Master's degree advisor Bahar Firoozabadi, who introduced me to the world of fluid mechanics, and who provided me with invaluable help and support when I was her student. I would like to thank my other Master's degree advisor Mohammad Farshchi, for providing research support when I was his student. I as well am thankful to Bahar Firoozabadi and Mohammad Farshchi for providing me with great opportunities to do research and obtain valuable skills. Furthermore, I am grateful to Hossein Afshin, and Amir Ghassemi with whom I collaborated during my Master's degree's work, for being great supporters and friends. I am also grateful to Bijan Farhanieh and Hossein Afshin for providing me an opportunity to work on a real world problem (i.e., about design and CFD calculations for the subway ventilation systems) during my Master's degree's work.

I as well am thankful to all my friends (I would prefer not to list their names here, as I may miss some of them). I really can't thank them enough for their support and friendship, and for simply being there for me.

Finally I am thankful beyond words to my family Nahid and Abbas, for their never-ending love and support, and for always being there for me. I can't begin to describe how appreciative I am for their presence within my life and for what they have done for me.

Chapter 1

Introduction

Coherent long-lived vortices are the well distinguished identities of geophysical and astrophysical flows. Possible examples are Gulf Stream rings (see figure 1.1) [Olson 1991] , vortices near strong oceanic currents [Lai & Richardson 1977; Lutjeharms et al. 2003; Kurian et al. 2011] and Meddies (see figure 1.2) [McWilliams 1985; Armi et al. 1988] in the ocean [also Chelton et al. 2011], similar vortices in other regions including the Ulleung Basin, Red Sea, and bay of Biscay [Meschanov & Shapiro 1998; Carton 2001; Chang et al. 2004], as well as vortices in the atmosphere of Jupiter [Marcus 1993], and other planets [Garate-Lopez et al. 2013; O'Neill et al. 2015], geophysical atmospheric vortices [Tyrlis & Hoskins 2008; Hassanzadeh et al. 2014; Hassanzadeh & Kuang 2015] and vortices in the protoplanetary disks [Barge & Sommeria 1995; Barranco & Marcus 2005; Marcus et al. 2013]. Understanding the dynamics of these vortices, such as their formation, longevity, and stability, are of great interest as these vortices can strongly affect their surroundings, for example, by efficiently mixing and transporting heat, momentum, and material [Provenzale 1999; Gascard et al. 2002; Marcus 2004; de Pater et al. 2010; Dong et al. 2014; Marcus et al. 2015]. There is a growing need to understand the attributes of these vortices, such as their nonlinear stability (i.e., their finite-amplitude evolution).

The linear and nonlinear (i.e., finite-amplitude) stability of vortices in rotating, stratified flows has been extensively studied in the past 30 years. However, the majority of those studies have used idealized models for the vortices or for the governing equations. For example, Ikeda [1981], Helfrich & Send [1988], and Benilov [2005a] studied quasi-geostrophic (QG) vortices in discrete two-layer flows; Gent & McWilliams [1986] studied columnar (i.e., with no variation in the vertical direction) QG vortices; Flierl [1988] examined columnar and 3D QG vortices; Nguyen et al. [2012] studied 3D QG vortices; Carton & McWilliams [1989] investigated one and two-layer QG vortices; Dewar & Killworth [1995], Killworth et al. [1997], Dewar et al. [1999], Baey & Carton [2002], Benilov [2004], Benilov [2005b], Benilov & Flanagan [2008], Lahaye & Zeitlin [2015], and Benilov et al. [1998] examined two-layer ageostrophic vortices (the latter also studied geostrophic vortices); Katsman et al. [2003] examined multi-layer ageostrophic vortices; Smyth & McWilliams [1998], Billant et al. [2006], and Yim & Billant [2015] studied columnar ageostrophic vortices; Stegner & Dritschel [2000] examined shallow-

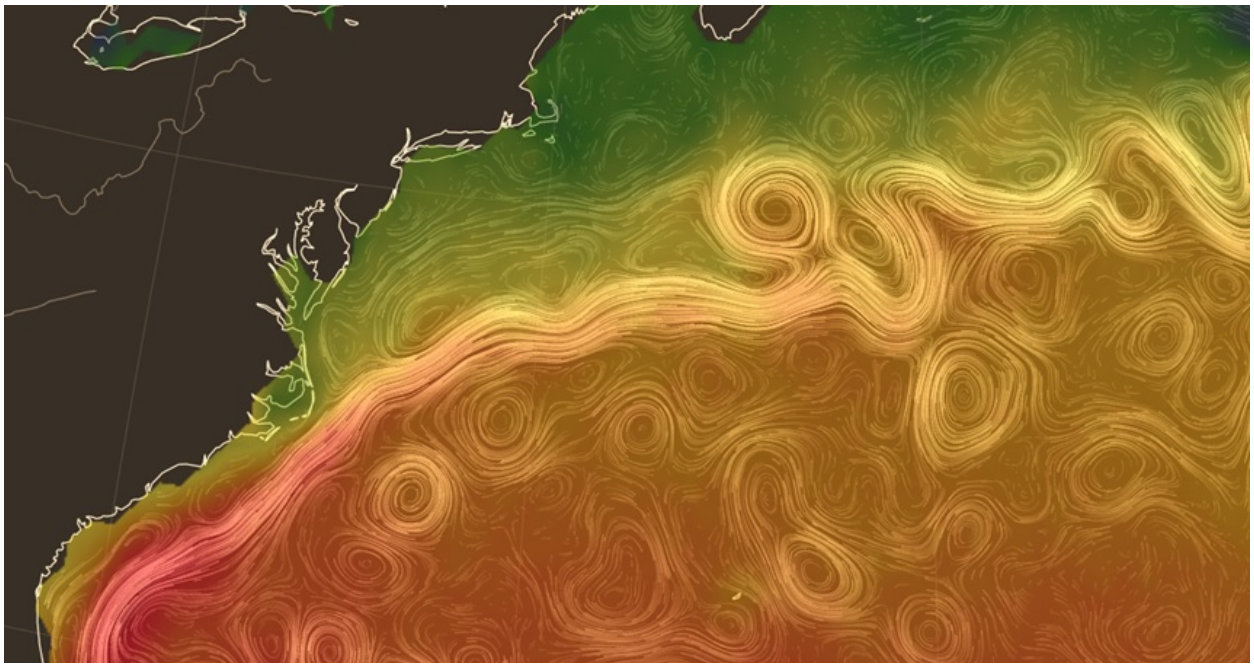

Figure 1.1: (Colour online) Vortices at the surface of the Gulf Stream off the US east coast. The different gray shades (different colours, in colour) demonstrate sea surface temperature anomaly, light gray (red, in colour) showing largest values and dark gray (green, in colour) demonstrating smallest ones, near current. The current is illustrated with the straight lines on the top right, and the vortices are shown as closed loops (Credit: Ocean Surface Current Analyses Real-time - a NASA supported research project).

water ageostrophic vortices; Lazar et al. [2013a], and Lazar et al. [2013b] studied shallow-water inertially-unstable vortices; Sutyrin [2015] examined two and three-layer ageostrophic vortices; Brunner-Suzuki et al. [2012] investigated the evolution of 3D ageostrophic vortices (but this was not technically a stability study because the initial vortices were created through geostrophic adjustment and thus out-of-equilibrium); and Tsang & Dritschel [2015] also studied the evolution, rather than the stability, of 3D ageostrophic vortices made from piecewise-constant elements of potential vorticity that were not exact equilibrium solutions of their equations of motion. One study focused on 3D equilibrium vortices using the full 3D Boussinesq equation is that of Yim et al. [2016] who examined the linear stability of a specific family of vortices with Gaussian angular velocity.

While valuable information on the stability of vortices in rotating stratified flows, vortices in planetary atmospheres, and oceanic eddies has been gained through the aforementioned studies, further investigation of the linear and nonlinear stability that extends beyond the simplifications and limitations of these studies is still needed.

Vortices in ocean and atmosphere (to several of which we referred above) have various length and time scales, and exist in different environments. However, a common aspect of these vortices is that their dynamics are predominantly controlled by the rotation, stratifi-

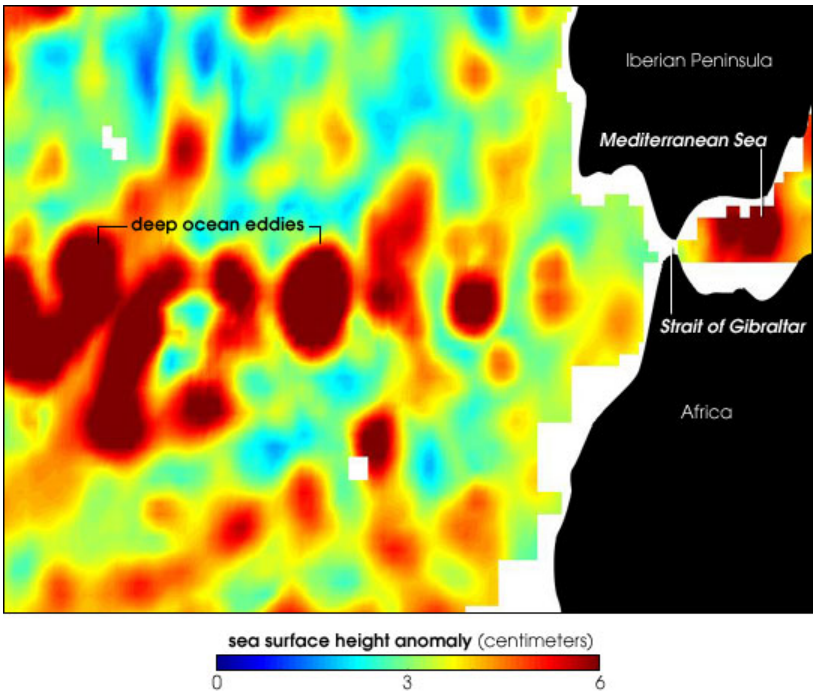

Figure 1.2: (Colour online) Meddies shown via the sea surface temperature anomaly. The dark gray (red, in colour) shows meddies entering into ocean, which is demonstrated over the left, where light gray (green, in colour) shows ocean temperature anomaly. Meddies usually are anticyclonic (i.e., their rotation direction is the opposite of the earth's rotation direction) (Credit: University of Delaware).

cation, and (in some cases) shear of their environment. Therefore, here we propose a study of these vortices, that is specifically planned to examine the vortex dynamics in a rotating stratified flow. Some of the questions about these vortices that we will answer in this thesis:

- Long lives: why some vortices have loner life times than others?
- Size: what controls the horizontal and vertical length scales of the vortices?
- Cyclone/anticyclone asymmetry: observed cyclones and anticyclones differ in terms of their life times, and populations. How can this asymmetry be explained?
- Critical layers: how do singular critical layers affect vortex dynamics?
- Robustness: why do some vortices remain robust, despite conditions (i.e., perturbations, fast growth rates, etc) that suggest that they should be quickly destroyed?
- Finite-amplitude perturbations: how do finite-amplitude perturbations (interaction with waves, other vortices, currents, topography, etc) affect vortex dynamics?
- Other possible items that are not discussed here, but are included in our work below.

This study's purpose is to address the linear and nonlinear stability of three dimensional (3D) axisymmetric vortices in rotating, stably-stratified, inviscid flows by analyzing the non-hydrostatic Boussinesq equations with an f-plane approximation in a 3D domain with periodic boundary conditions (and with numerical sponge layers implemented as Rayleigh drag and Newtonian cooling at distances far from the vortices). We focus on a widely-used model of geophysical and astrophysical vortices, which have pressure anomalies that are Gaussian in the radial and vertical directions and are in exact equilibrium. Our work extends the analyses of the previous studies in several ways:

(i) We examine the vortices with finite Rossby numbers and with internal stratifications that significantly differ from the stratification of the background flow.

(ii) We examine three-dimensional vortices (rather than 2D Taylor column).

(iii) The 3D baroclinic vortices studied here are exact equilibrium solutions of the 3D non-hydrostatic Boussinesq equations.

(iv) Our domain has as boundary conditions, numerically implemented sponge layers, which allow us to simulate a flow that is in fact unbounded.

In chapter 2, that appears in Mahdinia et al. [2017], we examine the vortices' linear stability, by calculating their most unstable eigenmodes' eigenvalues and eigenvectors, as function of the Rossby number Ro (i.e., which shows rotation), and Burger number Bu (i.e., which shows stratification). We show that neutrally-stable vortices exist over a small Ro-Bu parameter space region, and the cyclones have faster growth rates than those of the anticyclones. In particular most cyclones (i.e., for the parameter values that we examine in this study) have growth rates faster than 50 vortex turn around times (which for ocean eddies can corresponds to several years), and a confined anticyclonic region has growth rates slower than this value. This might explain the cyclone-anticyclone asymmetry of the vortices in the oceans. Furthermore, we examine the eigenmodes with critical layers, and show that when the eigenvalues go from unstable to neutrally-stable, the eigenmode family continues to exist, due to its phase speed being continuous across this transition, rather than ceasing to exist. Further proof is provided by showing that the unstable and neutrally stable eigenmodes have similar vertical structures, and are therefore clearly part of the same family. While most calculations here were done for $f/\bar{N} = 0.1$ (where f and $\bar{N}$ are the Coriolis and background Brunt-Väisälä frequencies), we also numerically verify and explain analytically, using non-dimensionalized equations; the insensitivity of the results to reducing $f/\bar{N}$ to the more ocean-relevant value of 0.01.

In chapter 3, we continue the chapter 2's analysis, by examining vortex nonlinear stability. For vortices that have growth rates faster than 50 vortex turnaround times, the evolution and finite-amplitude stability of the vortices, as they move towards their final equilibria, is studied with an initial value code. The initial-value calculations are for different vortex finite-amplitude perturbations (i.e., with different types, and/or amplitudes), and

it is demonstrated that, the initially large linear growth rates for some vortices (mentioned above) does not mean that vortices are destroyed or disintegrated; but rather that perturbations quickly saturate and the initial unperturbed and final equilibria remain close to each other. Our initial-value calculations above are carried out for a range (see chapter 3, §3.1) of Rossby number, Ro, and Burger number, Bu, that are relevant to the observations. We demonstrate that despite vortices being perturbed, the perturbations quickly plateau – at a constant value, and the vortices almost always have small-sized attraction basins (with only one vortex splitting radially, i.e., into tripoles), and for nearly all cases we examined here the final equilibria remain close to each other. All the above calculations are done for $f/\bar{N} = 0.1$, and effects of changing $f/\bar{N}$ is therefore forwarded to a future study. We also show for the vortices that have close initial unperturbed and final equilibria; that the long-term evolution is simply represented by an analytical solution, with the deviations from this representation shown to be small (that is after the flow reaches quasi-steady state). It should be noted as well that, our explanation for the equilibria's robustness does not require a direct forcing mechanism; it only involves damping of velocity and density far from the initial conditions' position and at our numerically implemented sponge layers.

Although our work above discusses in detail about linear and nonlinear stability of three-dimensional Gaussian axisymmetric vortices in a rotating stratified flow, perhaps the most important physical result of our work here is that, while a fast instability growth rate can destroy a vortex via nonlinear finite-amplitude instabilities (i.e., as might be suggested by some other studies), it also is possible that the perturbations quickly saturate, such that the initial unperturbed and final equilibria remain close to each other. Our goal here has been to demonstrate the latter.

Chapter 2

Linear analysis

2.1 Introduction

Two of the main motivations for some of the previous stability studies (see chapter 1) have been (a) the observed stability of the long-lived, approximately axisymmetric vortices in the oceans, and (b) the observed cyclone-anticyclone asymmetry in the oceans and planetary atmospheres. It has been observed through tracking individual vortices and by satellite observations that coherent oceanic vortices with radii of tens to hundreds of kilometers can last for months and even years ($\sim 1/2\text{-}3$) while remaining nearly axisymmetric [Lai & Richardson 1977; Armi et al. 1989; Olson 1991; Chelton et al. 2011]. However, most theoretical studies of axisymmetric vortices in rotating stratified flows have found them to be linearly unstable (usually with fast growth rates that are incompatible with the observed longevity of these vortices), unless unrealistic parameters or vertical structures are assumed [see the discussions in Stegner & Dritschel 2000; Benilov 2004; Benilov 2005a; Sutyrin 2015]. Observations of planetary atmospheres [Mac Low & Ingersoll 1986; Cho & Polvani 1996], and oceans at the mesoscales [McWilliams 1985; Chelton et al. 2007; Chelton et al. 2011; Mkhinini et al. 2014] show that long-lived vortices are predominantly anticyclones. Whether this asymmetry is due to differences between the stability (linear or nonlinear) properties of cyclones and anticyclones requires a better understanding of how stability changes with the Rossby number. It should be noted that factors other than stability can be responsible for, or at least contribute to, the observed cyclone-anticyclone asymmetry; for example, the creation mechanisms might favor anticyclones [Perret et al. 2011], anticyclones might decay slower than cyclones [Hoskins et al. 1985, §7; Graves et al. 2006], or coherent cyclones might be harder to observe in planetary atmospheres than anticyclones [Marcus 2004].

In the current study, we address the stability of isolated, 3D, axisymmetric vortices in rotating, stably-stratified, inviscid flows by analyzing the full non-hydrostatic Boussinesq

With minor modifications, some chapter 1 parts and chapter 2 are reprinted with permission from: Mahdinia M., P. Hassanzadeh, P. S. Marcus, & C.-H. Jiang. "Stability of three-dimensional Gaussian vortices in an unbounded, rotating, vertically stratified, Boussinesq flow: linear analysis". In: *J. Fluid Mech.* 824 (2017), pp. 97–134.

equations with an f-plane approximation in a 3D domain with periodic boundary conditions (modified to simulate an unbounded flow). We focus on a widely-used model of geophysical and astrophysical vortices, which have pressure anomalies that are Gaussian in the radial and vertical directions and are in exact equilibrium [e.g., McWilliams 1985; van Heijst & Clercx 2009; Chelton et al. 2011; Hassanzadeh et al. 2012]. Our work extends the analyses of the previous studies in several ways, including:

(i) By using the Boussinesq equations, we can study vortex dynamics with any Rossby number and internal stratification. Here we focus on cyclones and anticyclones in the geostrophic balance regime ($-0.5 < Ro < 0.5$), which is the range of Ro relevant to most long-lived geophysical and astrophysical vortices [e.g., Olson 1991; Aubert et al. 2012] (all parameters and dimensionless numbers are defined in §2.2). The vertical stratification inside the 3D equilibrium vortices that are studied here can be much stronger or much weaker compared to the stratification of the background (i.e., far from the vortex) flow, which is also the case for many oceanic and atmospheric vortices [e.g., Aubert et al. 2012]. Considering vortices with finite Rossby numbers and with internal stratifications that significantly differ from the stratification of the background flow extends the stability analysis well beyond the QG approximation.

(ii) Geophysical and astrophysical vortices that are far from both horizontal and vertical boundaries (e.g., free surfaces or solid surfaces) and that are in quasi-equilibrium have been observed to be three-dimensional (rather than 2D Taylor columns); examples include Jupiter's Great Red Spot [Marcus 1993], Meddies [Aubert et al. 2012; Bashmachnikov et al. 2015], and zombie vortices in the protoplanetary disks [Barranco & Marcus 2005; Marcus et al. 2013; Marcus et al. 2015]. The vertical length scales of these vortices are finite and usually much smaller than their horizontal length scales, which can be understood as a direct consequence of the gradient-wind balance [see Hassanzadeh et al. 2012]. The present study extends the rigorous stability analysis of Boussinesq vortices beyond barotropic Taylor columns.

(iii) Exploiting the universal scaling law of Hassanzadeh et al. [2012] and Aubert et al. [2012], the 3D baroclinic vortices studied here are exact equilibrium solutions of the full 3D non-hydrostatic Boussinesq equations (see §2.2). The exact equilibrium is particularly important for a rigorous linear analysis, which is the subject of this study.

(iv) By using the full, 3D, non-hydrostatic Boussinesq equations, we avoid restrictions on the vertical structure of the vortex or background flow that result from the QG or multi-layer models discussed above. Although here we focus on background flows with stable stratification such that the density decreases linearly with height (i.e., constant Brunt-Väisälä frequency $\bar{N}$), background flows with more realistic $\bar{N}(z)$ profiles can be easily included in this framework.

(v) The family of Gaussian vortices that is studied here has been shown to fit many types of oceanic and laboratory vortices reasonably well [e.g., van Heijst & Clercx 2009; Chelton

et al. 2011] and has been widely-used as a model in various theoretical studies [e.g., McWilliams 1985; Morel & McWilliams 1997; Hassanzadeh et al. 2012; Negretti & Billant 2013]. Furthermore in this model, all fields (e.g., velocity, potential vorticity, and density) are continuous and smooth, which eliminate unphysical instabilities that can arise from discontinuities (which are present, for example, when vortices are modeled with piecewise-constant shells or patches of potential vorticity).

In this chapter we address the linear stability of 3D vortices in rotating stratified flows and discuss the growth rates and most unstable eigenmodes as functions of the Rossby number Ro (for $-0.5 < Ro < 0.5$), the Burger number Bu (for $0.02 < Bu < 2.3$), and $f/\bar{N} = 0.1$ and 0.01. One of the main purposes of this chapter is to extend the linear stability analysis of a specific family of 3D equilibrium vortices beyond some of the approximations or constraints imposed in previous studies and produce the parameter map of stability for 3D non-hydrostatic Boussinesq flows. We also investigate how different modes take over as the most unstable one as the Burger number changes and explore the vertical and horizontal structures of these modes and their critical layers. We discuss how the stability properties found here compare with those reported in other studies using QG or multi-layer equations or using a different vortex model. Furthermore, we show numerically that the linear stability of the family of 3D vortices that we examine is only weakly dependent on the value of $f/\bar{N}$ for $f/\bar{N} \leq 0.1$ and we discuss the reason behind this behavior.

The results of this study improve the understanding of the generic stability properties of 3D vortices in rotating stratified flows, and have implications for the dynamics of some of the geophysical and astrophysical vortices. These results are most relevant to the stability of interior (i.e., far from boundaries) oceanic vortices such as Meddies. It is acknowledged that the exclusion of horizontal and vertical background shear, free surface, lateral boundaries, bottom topography, compressible effects, and vertical variation of $\bar{N}$ limit the direct applicability of the current analysis to other oceanic eddies and planetary and astrophysical vortices. However, the numerical framework presented here can be readily adapted to account for the aforementioned boundary conditions/physical processes in future studies, and the results of this study will be needed to evaluate the influence of these boundary conditions/processes on the stability properties of these vortices.

The remainder of this chapter is structured as follows. The equations of motion, numerical method, Gaussian vortex model, and eigenmode solver are discussed in §2.2. The eigenmodes with critical layers are discussed in §2.3, and the results of the linear stability analysis and the stability map along with comparison with previous studies are presented in §2.4. Insensitivity of the most unstable modes to $f/\bar{N}$ is discussed in §2.5 and the radial and vertical structures of the most unstable modes are presented in §2.6. Discussion and summary are in §2.7.

2.2 Problem formulation

Equations of motion

The Boussinesq approximation of the equations of motion for 3D rotating, stratified, inviscid flows in the Cartesian coordinates (x, y, z), as observed in a frame rotating with angular

velocity $(f/2)\,\hat{\boldsymbol{z}}$, is [Vallis 2006]

$$\frac{\mathrm{D}\boldsymbol{v}}{\mathrm{D}t} = -\frac{\nabla p}{\rho_o} + \boldsymbol{v}\times f\hat{\boldsymbol{z}} + b\,\hat{\boldsymbol{z}}, \qquad \frac{\mathrm{D}b}{\mathrm{D}t} = -\bar{N}^2 v_z, \qquad \boldsymbol{\nabla}\cdot\boldsymbol{v} = 0, \tag{2.1}$$

where the operator $\mathrm{D}/\mathrm{D}t \equiv \partial/\partial t + \boldsymbol{v}\cdot\boldsymbol{\nabla}$ is the material derivative, t denotes time, $\boldsymbol{v} = (v_x, v_y, v_z)$ is the 3D velocity vector, f is the Coriolis frequency (constant in our study), and g is the acceleration of gravity. The total pressure and the total density of the fluid are $p_{tot} \equiv \bar{p}(z) + p(x,y,z,t)$ and $\rho_{tot} \equiv \bar{\rho}(z) + \rho(x,y,z,t)$, where $\bar{\rho}(z=0) = \rho_o$. We define the buoyancy as $b(x,y,z,t) \equiv -g\rho/\rho_o$. Quantities with a bar are properties of the equilibrium background flow (i.e., far from the vortex where $\boldsymbol{v}\to 0$, $b\to 0$, $\rho\to 0$, and $p\to 0$). The background pressure $\bar{p}$ and density $\bar{\rho}$ are in hydrostatic balance $d\bar{p}/dz = -\bar{\rho}g$. The background Brunt-Väisälä frequency $\bar{N} \equiv \sqrt{-(g/\rho_o)(d\bar{\rho}/dz)}$ is assumed to be constant, so that $\bar{\rho}(z) = \rho_o(1 - \bar{N}^2 z/g)$.

In the above equations, we have ignored viscosity in the momentum equations and diffusion in the density equation, which are reasonable approximations for atmospheric and oceanic flows. Furthermore, we have dropped the planetary centrifugal term from the momentum equations, assuming that the rotational Froude number $f^2 d/g$ is small [Barcilon & Pedlosky 1967], where d is the distance between the center of the vortex and the planetary rotation axis.

Numerical method

A pseudo-spectral initial-value solver is developed to solve (2.1) in a triply periodic domain with 256 or 512 Fourier modes in each direction. In numerical simulations of strongly rotating stratified flows, resolving the fast inertia-gravity waves can substantially limit the size of the time step Δt and thus increase the computational cost. Here we use the semi-analytic method developed by Barranco & Marcus [2006] for rotating stratified flows, which enables us to accurately and efficiently deal with large $f\Delta t$ and $\bar{N}\Delta t$.

A vortex in the middle of a periodic domain interacts with its periodic images. To minimize this interaction and its potential impact on the stability of the vortex (and to simulate having an unbounded flow) the computational domain size is chosen to be large compared to the vortex size: the domain size in the x and y directions, i.e., the values of L_x and L_y are 7.5 (or more often 15) times larger than the initial vortex diameter ($2L$), and, similarly, the domain size in the z direction L_z is 7.5 (or more often 15) times larger than the initial vortex height ($2H$). There are two reasons for sometimes making the domain size very large. First, we wanted to ensure that the periodic boundary conditions had no perceptible effects on the flow dynamics; secondly, in the follow-up chapter to this one (see our Discussion §2.7) unstable vortices often fragmented with pieces of the initial vortices becoming widely separated so that the calculations required a large domain. To help simulate an unbounded flow, we also added a cylindrical sponge layer near the boundaries of the computational domain (see Appendix B). The sponge layer, implemented as Rayleigh drag and Newtonian cooling in (2.1), damps $\boldsymbol{v}$ and ρ outside a cylindrical surface of diameter $24L$ and height $24H$

(for the large domain calculations) or $12L$ and height $12H$ (for the small domain calculations) around the center of the domain. Another advantage of adding the sponge layer is that it damps the reflection of the outgoing inertia-gravity waves, and occasional detached filaments back to the domain at the periodic boundaries. One more advantage of the axisymmetric sponge layer is that we find that it prevents the (non-axisymmetric) periodic boundary conditions in x and y from adding any significant non-axisymmetric perturbations to the initial vortices. The latter is important when computing the stability of the vortices. One way of determining if the domain size is too small is to compute the ratio of the magnitude of each component of the velocity and density of a numerically computed eigenmode at a damped location just inside the sponge layer to the maximum value of that component over the entire domain. With the domain sizes presented here, that ratio is always of order 10^{-4} (or smaller), but the ratio increases to values with orders as large as 10^{-2} when the computational domain is reduced to $(10L)\times(10L)\times(10H)$ and a sponge layer with diameter of $8L$ and height $8H$.

Hyperviscosities and hyperdiffusivities are added to our otherwise inviscid and non-diffusive calculations to stabilize the code. See Barranco & Marcus [2006] for more details.

Initial equilibria: Gaussian vortices

In this study we focus on 3D axisymmetric baroclinic vortices that are initially in horizontal cyclo-geostrophic balance and vertical hydrostatic balance, and hence they are in gradient-wind balance [Vallis 2006]. The initial vortex is centered at $r = 0$ and $z = 0$, where r denotes the radial coordinate. A widely-used model for oceanic and laboratory vortices is that of an axisymmetric vortex with a Gaussian pressure distribution [e.g., McWilliams 1985]

$$p = p_o\,\chi(r,z), \tag{2.2}$$

where $\chi(r,z) \equiv \exp\left[-(r/L)^2-(z/H)^2\right]$. Using (2.2) and the definitions presented in §2.2, an exact, steady, axisymmetric equilibrium solution to the Boussinesq equations in (2.1) is the vortex

$$v_\phi(r,z) = \frac{fr}{2}\left(-1+\sqrt{1-\left(8p_o\chi(r,z)\right)/\left(\rho_o f^2L^2\right)}\right), \qquad v_r = v_z = 0, \tag{2.3}$$

$$b(r,z) = -\frac{2p_oz}{\rho_oH^2}\,\chi(r,z), \tag{2.4}$$

where the cylindrical coordinate is used for convenience (v_ϕ is the azimuthal velocity). For any vortex, whether or not it is Gaussian, we shall define a quantity written with a subscript "c" to mean that the quantity is to be evaluated at the vortex center, so N_c is the Brunt-Väisälä frequency at the center of a vortex, or $N_c^2 \equiv \bar{N}^2 + (\partial b/\partial z)_c$. For the Gaussian vortex described by (2.3)-(2.4),

$$N_c^2 = \bar{N}^2 - 2p_o/(\rho_o\,H^2). \tag{2.5}$$

As discussed in the next section, for some values of p_o, $N_c^2 < 0$, which means that the density distribution is locally unstable at the vortex center with heavy fluid over light fluid (i.e., statically unstable). It is convenient to define the Rossby number Ro, which by definition has $Ro > 0$ for a cyclone and $Ro < 0$ for an anticyclone, in terms of the maximum (or minimum) value of a vortex's vertical vorticity ω_E, such that $Ro \equiv \omega_E/2f$. For the Gaussian vortices described above $\omega_E = \omega_c$, and

$$Ro = \omega(r = 0, z = 0)/2f = -1/2 + \sqrt{1/4 - 2p_o/(\rho_o f^2 L^2)}. \tag{2.6}$$

Note that the Gaussian vortex has an aspect ratio of

$$\left(\frac{H}{L}\right)^2 = \frac{-Ro(1+Ro)f^2}{\bar{N}^2[1-(N_c/\bar{N})^2]}, \tag{2.7}$$

in accord with the universal scaling law of Hassanzadeh et al. [2012] and Aubert et al. [2012], which is valid for all vortices that are in cyclo-geostrophic and hydrostatic balance. This can be seen by simply replacing $2p_o/\rho_o$ in (2.6) with $H^2(\bar{N}^2 - N_c^2)$ using (2.5), and then solving for H/L.

The three independent dimensional parameters in the governing equations (2.1) are f, $\bar{N}$, and ρ_o. The sizes of the computational domain $L_x \times L_y \times L_z$ have no effect (on the dimensional analysis), due to the fact that the cylindrical sponge layer is far from the vortices, and that the net circulations of the flow are zero, which makes the velocity due to the vortices fall off exponentially fast and be effectively zero at the sponge layer. (See the definition of *shielded* below and in the appendices.) The equilibrium Gaussian vortices in (2.2)-(2.4) introduce three additional dimensional parameters H, L, and p_o. Thus, there are three independent, dimensionless parameters that describe the dynamics of Gaussian vortices. The choice of these parameters is not unique, but here we choose Ro, $f/\bar{N}$, and

$$Bu \equiv \left(\frac{\bar{N}}{f}\frac{H}{L}\right)^2 = (L_r/L)^2, \tag{2.8}$$

where the latter is the Burger number, and $L_r \equiv H\bar{N}/f$ is the deformation radius. It should be noted that whether the vortices studied here are *big* or *small* depends on the inverse of their Burger number, which is the square of the vortex radius over L_r. Big vortices have small Bu, and vice versa.

The Gaussian vortices defined in the above model are *shielded*. Here we define a *shielded* flow as one in which the circulation computed with the z-component of the vorticity over the entire (x, y)-plane for any fixed value of z is zero. In addition, the circulation computed with the x-component of the vorticity over the (y, z)-plane for any fixed value of x is zero; and the circulation computed with the y-component of the vorticity over the (x, z)-plane for any fixed value of y is zero. (*n.b.* Figure 2.1(b) does not violate our definition of *shielded* because the figure shows the vertical component of the vorticity in an x-z plane, not an x-y plane.) Our governing equations and boundary conditions show that if the initial flow is

shielded, then the flow is shielded for all time. In practical terms, a shielded isolated vortex is one in which the central core of the vortex is surrounded, or partially surrounded, by a region (shield) of opposite vorticity and that the circulation quickly vanishes outside the shield. For an arbitrary (i.e., not necessarily Gaussian) cyclonic vortex, the *core* of a cyclone is a contiguous region at and near the vortex center where the vertical component of its vorticity ω is greater than or equal to zero. The *shield* is a region around the core (usually looking like a shell or annular ring) located not too far from the core, where $\omega < 0$. The precise definitions that we use for *core* and *shield* are in Appendix A. The core and shield of an example Gaussian vortex are illustrated in figures 2.1(a) and (b). The definitions of the core and shield of an anticyclone are analogous to those of the cyclone. For Gaussian vortices and many other types of shielded cyclones, outside the shield the amplitude of the vorticity decays exponentially with the radial distance r (or r^p with $p \geq 2$) from the vortex center. In our calculations, the circulation due to the vertical component of the vorticity $\int \omega(x, y, z)\, dx\, dy$ (where the integral is over the entire x-y computational domain) at each value of z must remain zero due to the periodic boundary conditions.

Commonly, in the studies of oceanic and atmospheric vortices, potential vorticity (PV) is used to describe the vortices, instead of vertical vorticity, due to its conservation property [Hoskins et al. 1985; Morel & McWilliams 1997]. Ertel's PV in figure 2.1 is defined [Ertel 1942] as

$$Q \equiv [\boldsymbol{\omega} + f\hat{\boldsymbol{z}}] \cdot \left(\frac{\nabla b + \bar{N}^2 \hat{\boldsymbol{z}}}{f\bar{N}^2} \right) - 1, \tag{2.9}$$

where $\boldsymbol{\omega} \equiv \boldsymbol{\nabla} \times \boldsymbol{v}$ is the vorticity vector as observed in the rotating frame. To provide a better sense about the PV structure of the vortices studied here, $Q(r, z)$ for a Gaussian vortex with $Ro = 0.2$ and three values of $Bu = 0.1, 1$ and 2 is depicted in figures 2.1(c)-(e), showing that the PV structure can significantly change with Bu (see Morel & McWilliams [1997] for a discussion of potential vorticity of Gaussian vortices). Our purpose for showing the PV of Gaussian vortices is to allow the reader the ability to make comparisons of the vortex model with what is used in some other stability studies such as Tsang & Dritschel [2015] who model the initial vortex with uniform patches of PV.

Finally it should be noted that there is a restriction on the equilibrium of anticyclones in the Gaussian model (2.2)-(2.4); there is no equilibrium for anticyclones for $Ro < -0.5$. This is because (2.3) and (2.6) show that v_ϕ does not have a real solution for $Ro < -0.5$, as noted, for example, by McWilliams [1985] and Olson [1991].

Eigenmodes

The symmetries of the governing equations in (2.1) linearized around the equilibrium vortex (2.2)-(2.4) are presented in dimensionless form in §2.5 in equations (2.22)-(2.26). These equations and their boundary conditions show that the eigenfunctions are either symmetric or anti-symmetric with respect to the $z = 0$ horizontal plane and have an m-fold azimuthal symmetry about the z-axis. We use the labels Sm or Am for each eigenmode, to identify

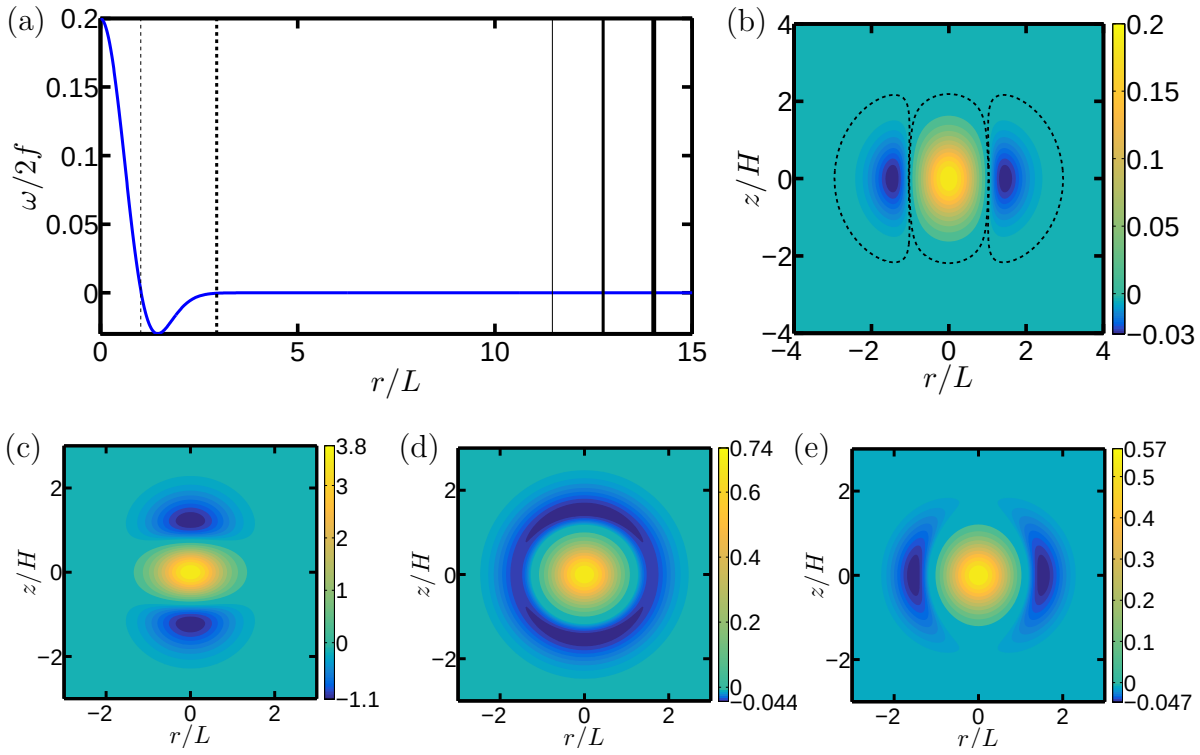

Figure 2.1: (Colour online) Vertical vorticity $\omega(r, z)$ and potential vorticity $Q(r, z)$ for Gaussian cyclones defined by (2.2)-(2.4). Panel (a) shows ω at $z = 0$ as a function of r as a solid curve (blue, in colour) for $Ro = 0.2$, $Bu = 0.1$, and $f/\bar{N} = 0.1$. The thin and thick dashed vertical lines show the boundaries of the core and the shield (see Appendix A). The solid vertical lines at large radii show, with increasing thickness from left to right, where the boundary damping function f_{bd} (see Appendix B) reaches values of 0.01, 0.5 and 0.99, respectively. Panel (b) shows $\omega(r, z)$ in units of $2f$ in the r-z plane of the vortex in panel (a). Dashed lines indicate the boundaries of the core and shield. Panels (c) to (e) show the potential vorticity $Q(r, z)$ for a Gaussian vortex with $Ro = 0.2$ and $f/\bar{N} = 0.1$, for $Bu = 0.1$, $Bu = 1.0$ and $Bu = 2.0$, respectively. For larger values of Bu, the distributions of Q and ω are similar.

it as Symmetric (or Anti-symmetric) with respect to the $z = 0$ horizontal plane and with m-fold symmetry.

The complex eigenvalues λ and eigenfunctions are of the form

$$e^{\lambda t}\, \boldsymbol{g}_{eig}(r,z)\, e^{im\phi} = e^{\sigma t}\, \boldsymbol{g}_{eig}(r,z)\, e^{im(\phi - ct)}, \tag{2.10}$$

where the eigenvector has 3 velocity components, a density component, and a pressure component:

$$\boldsymbol{g}_{eig}(r,z) \equiv [v_{r,eig}, v_{\phi,eig}, v_{z,eig}, \rho_{eig}, p_{eig}]. \tag{2.11}$$

The three velocity components are with respect to cylindrical coordinates, where m is the integer azimuthal wave number, σ is a real growth (or decay) rate, and c is a real azimuthal phase speed. By taking the complex conjugate of the linearized equation, we can show that if λ is an eigenvalue with eigenfunction given by (2.11), then $\lambda^\dagger$ is also an eigenvalue with eigenfunction $\boldsymbol{g}^\dagger_{eig}(r,z) \equiv [v^\dagger_{r,eig}, v^\dagger_{\phi,eig}, v^\dagger_{z,eig}, \rho^\dagger_{eig}, p^\dagger_{eig}]$, with m replaced by $-m$, c unchanged, and where the superscript $\dagger$ denotes complex conjugate. Or in other words, the eigenvalues λ when plotted in the complex plane are symmetric with respect to the real axis. Because the equations are non-dissipative, replacing t with $-t$ in the linearized equations shows that if $\lambda \equiv \sigma - imc$ is an eigenvalue with eigenfunction given by (2.11), then $\lambda' \equiv -\sigma - im'c'$ is an eigenvalue that corresponds to $\boldsymbol{g}'_{eig}(r,z) \equiv [v_{r,eig}, -v_{\phi,eig}, v_{z,eig}, -\rho_{eig}, -p_{eig}]$, with $m' = -m$ and $c' = c$. Or in other words, the eigenvalues λ when plotted in the complex plane are symmetric with respect to the imaginary axis, and for each eigenfunction with a positive growth rate, there is one with a negative growth rate and vice versa. The flow can never be linearly stable with all of its eigenmodes having decay rates. The flow can either be unstable or be neutrally stable with all of its eigenmodes on the imaginary axis with $\sigma = 0$. For the Gaussian vortices, the two symmetries of the linearized equations combine and therefore the eigenvalues appear as quartets of the form $\pm a \pm ib$, with all four possible combinations of the signs, and where a and b are real functions of m and of the parameters of the unperturbed vortex Ro, Bu, and $f/\bar{N}$. For Hamiltonian systems [Ozorio de Almeida 1988], it can be shown that the quartet of eigenvalues is of a more specialized form:

$$\lambda = \pm\sqrt{A} \pm iB, \tag{2.12}$$

with all four possible combinations of the signs, and where A and B are real functions of the control parameters of the system. For many non-dissipative flows, e.g. unidirectional shears flows with vortex sheets and/or vortex layers made up of piecewise-constant vorticity [Drazin & Reid 2004], it can be shown that the quartets of the eigenvalues are of the form of (2.12). Consider a system with eigenvalue quartets such as those in (2.12). When $A > 0$, the eigenvalues in the quartets are symmetric about the real and imaginary axes, and each quartet has 2 unstable and 2 stable eigenmodes. If a control parameter changes such that A decreases, then eigenvalues symmetrically approach the imaginary axis and collide when $A = 0$. For that parameter value, there are two pairs of degenerate, neutrally-stable eigenmodes with all 4 eigenvalues on the imaginary axis. If the control parameter is further changed

such that A continues to decrease and becomes negative, then the eigenvalues are no longer degenerate, but they remain on the imaginary axis and all 4 eigenmodes remain neutrally stable, regardless of how negative A becomes. (It is also possible that the eigenvalues always remain on the imaginary axis. For example, if A is equal to $-D^2$, where D is a real number, for a positive D the vortex has four imaginary eigenvalues all on the imaginary axis. If D then goes to zero, the eigenvalues approach, collide and become degenerate. If D is further decreased such that it becomes negative, the eigenvalues are no longer degenerate, but remain on the imaginary axis [Kirillov 2017]. Here however our numerical calculations show that the eigenvalues never remain on the imaginary axis; i.e., they develop a real part and move away from it. For more details, see the next two sections). Although we cannot prove that the eigenvalue quartets of the linear eigenmodes of the Gaussian vortex have the form of (2.12), all of our numerical simulations are consistent with (2.12). (See §2.3.)

Note that although we are studying the stability of axisymmetric vortices, we solve (2.1) in Cartesian coordinates rather than in cylindrical coordinates. A numerical solver in Cartesian coordinates avoids the difficulties of handling the singularity at the origin ($r = 0$), which requires using special polynomial basis functions [Matsushima & Marcus 1995]. However, our main reason for using Cartesian coordinates is that future studies can include background shear flows, so that the stability of vortices in planetary atmospheres and protoplanetary disks can be examined, as discussed in the thesis Introduction. To minimize the effect of the square computational domain, we have used a circular sponge layer as described in §2.2. In order to find the eigenmodes with various classes of azimuthal (and vertical) symmetry in the Cartesian coordinates, we use our initial-value solver as an eigenvector/eigenvalue solver and additionally use a spatial symmetrizer (see Appendix C for details). Using the spatial symmetrizer, the eigenmodes can be restricted to be symmetric or anti-symmetric in the vertical direction, while in the azimuthal direction we can enforce one of the following classes of symmetry: m odd; m even not divisible-by-4; and m even and divisible-by-4. We use these specific symmetry groups to apply the azimuthal symmetry directly in the Cartesian coordinates, which greatly speeds up the convergence of the calculations, and also avoids introducing additional errors due to transformation between Cartesian and cylindrical coordinates (see Appendix C).

2.3 Critical layers

Eigenmodes of unidirectional equilibrium flows such as the Gaussian vortices studied here can have critical layers, i.e., singularities at locations where the azimuthal phase speed c is equal to the azimuthal velocity $v_\phi(r, z)$ of the unperturbed vortex [Maslowe 1986; Benilov 2003].[1] Here we show examples of eigenmodes with critical layers and discuss, for a few cases, how different modes take over as the fastest-growing mode as Bu changes, which will be used later to interpret the results of §2.4. It should be noted that despite the

[1] In stratified unidirectional flows, critical layers can appear at other locations as well [Marcus et al. 2013; Marcus et al. 2015].

peculiar nature of critical layers, it is not difficult to accurately compute them using high-resolution numerical simulations. For example, Nguyen et al. [2012] and Yim et al. [2016] have simulated critical layers in 3D QG and Boussinesq vortices, respectively. Recently, we have numerically computed critical layers, with and without dissipation, in stratified, rotating, unidirectional flows and found that with sufficient spatial resolution the locations, widths and other analytically-known properties of the critical layers can be quantitatively reproduced [Marcus et al. 2013; Marcus et al. 2015]. In the results presented here, the location of the critical layers and the phase speed of the eigenmode containing the critical layer are insensitive to the numerical resolution and remain the same when the resolution is increased by a factor of 4 by halving the domain size in each direction to $(15L)\times(15L)\times(15H)$ and increasing the Fourier modes from 256^3 to 512^3 (the figures showing the structure of the eigenmodes in this section are from the higher resolution).

The singularity in the eigenmode occurs where the coefficient $[v_\phi(r,z)/r - c - i\sigma/m]$ in front of the highest-order derivative terms in the governing equations of the eigenmode becomes zero. Unless the growth rate σ is zero and the eigenmode is neutrally stable, the eigenmode is no longer formally singular. However, the amplitudes of the eigenmodes remain large at locations where $v_\phi(r,z)/r = c$ for parameter values where $\sigma > 0$ and the mode is *weakly* growing. For parameter values where the analytically computed eigenmode has $\sigma = 0$, but the eigenmode is computed numerically with a modified initial-value code (as done here) with weak hyperdissipation, the computed eigenmode has large amplitude at $v_\phi(r,z)/r = c$, and the magnitude of the numerically computed growth rates σ are typically less than or equal to 0.002 in inverse units of the vortex turnaround time $\tau \equiv 4\pi/\omega_c$, where ω_c is the absolute value of the vertical vorticity at the center of the vortex.

We argued in §2.2 that as a parameter value, such as the Burger number, is changed such that a growing/decaying pair of eigenmodes has its eigenvalues λ collide on the imaginary axis, the eigenmodes become neutrally stable and degenerate. As the parameter value further changes, the eigenvalues remain neutrally stable and their phase speeds become distinct from each other. Here we demonstrate in detail that this scenario of eigenvalue collision, in which the families of eigenmodes *continue* after the collision rather than ceasing to exist due to the singularity of the critical layer, is correct by illustrating the collision for three distinct families of eigenmodes with critical layers. In particular, we show that as the Bu changes and the eigenmode goes from unstable to neutrally stable, the family containing that eigenmode continues to exist and remains neutrally stable as the Bu is further changed. We need these three demonstrations to not only show that our numerical computations of eigenmodes are accurate, but also to highlight the physics of the collisions.

Figure 2.2 shows the growth rate σ and phase speed c of the fastest-growing eigenmode with S2 symmetry for $Ro = 0.05$ and $0 \le Bu \le 2.1$. As Bu increases, the growth rate in figure 2.2(a) changes from positive (unstable) to zero (neutrally stable) at $Bu \simeq 0.823$. Note that we have computed three neutrally-stable eigenmodes in this family. There can be multiple neutrally-stable S2 eigenmodes for the same Ro, $f/\bar{N}$, and Bu so it is necessary to show that the eigenvalues with $Bu \lesssim 0.823$ and $Bu \gtrsim 0.823$ belong to eigenmodes in the same family. We do this in two ways. Figure 2.2(b) shows the phase speeds c for the

eigenmodes illustrated in figure 2.2(a). According to (2.12), a necessary condition that the eigenmodes belong to the same family is that there is no discontinuity in c at the value of Bu where σ changes from positive to zero.[2] Figure 2.2(b) shows that this condition is met. Figure 2.3 shows the vertical vorticity of the eigenmodes whose eigenvalues are shown in figure 2.2 with $Bu = 0.7$ (where the eigenmode is unstable) and $Bu = 0.9$ (where the eigenmode is neutrally stable). The eigenmodes clearly have similar radial structures and are therefore part of the same family. The continuous, nearly-circular curve (dark green, in colour) is the locus in the r-z plane where $v_\phi(r, z)/r = c$ and indicates the theoretical location of the critical layer. The large vorticity that is nearly coincident with the continuous curve is the critical layer.

Figures 2.4 and 2.5 show the growth rates, phase speeds, and the vertical vorticity of another family of eigenmodes with critical layers for $Ro = 0.05$ and $0 \leq Bu \leq 2.1$. These eigenmodes have A1 symmetry and are the fastest growing eigenmodes when $Bu \lesssim 0.2$. As Bu increases, the growth rate changes from positive (unstable) to zero (neutrally stable) at $Bu \simeq 0.177$. The continuity of c and the similarity of the vorticity distributions for the unstable and neutrally-stable eigenmodes indicate that the unstable and neutrally-stable eigenmodes belong to the same family and that the family does not end abruptly at the value of Bu where the eigenmodes pass from unstable to neutrally stable.

Figures 2.6 and 2.7 also show the growth rates and phase speeds and the vertical vorticity of a different family of eigenmodes with critical layers with A1 symmetry for $Ro = 0.05$ and $0 \leq Bu \leq 2.1$. For this family as Bu decreases, the growth rate changes from positive (unstable) to zero (neutrally stable) at $Bu \simeq 1.02$. Again, the continuity of c and the similarity of the vorticity distributions for the unstable and neutrally stable eigenmodes indicate that the unstable and neutrally-stable eigenmodes belong to the same family and that the family does not end abruptly at the value of Bu where the eigenmodes pass from unstable to neutrally stable. Note that although the set of figures 2.4 and 2.5 and the set of figures 2.6 and 2.7 both illustrate A1 eigenmodes, they are different families of eigenmodes. The distinction is easily seen because the radial structures of the eigenmodes differ and because the phase speeds differ. We have illustrated these two different families of A1 eigenmodes to emphasize the fact that we can easily determine when two families of eigenmodes are distinct and when they are not. These results demonstrate that the unstable and neutrally-stable eigenmodes in figure 2.2 (or in figure 2.4 or in figure 2.6) are part of the same family and confirm that when a pair of eigenvalues of eigenmodes of the vortices studied here collide on the imaginary axis, the families of eigenmodes do not terminate. This finding will be used later to interpret the results of §2.4 (specifically, figure 2.9).

Finally, it should be mentioned that for the cases examined here ($Ro = 0.05$, $0.1 \lesssim Bu \lesssim 1.6$), the peripheral location of critical layers is found to be generic (figures 2.3, 2.5, 2.7, and 2.14(f)), which is consistent with the QG analysis of Nguyen et al. [2012].

[2]Note that the slope of c can be discontinuous at the Bu where σ changes from positive to zero.

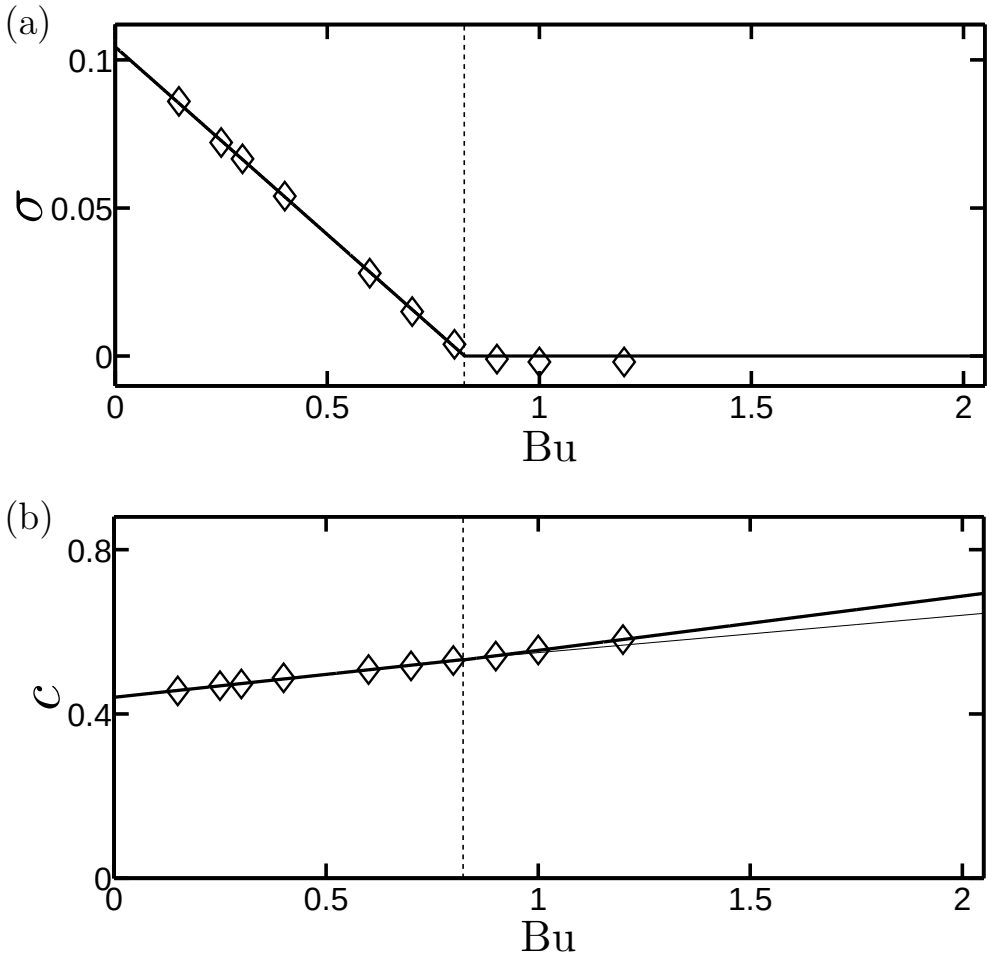

Figure 2.2: (a) Growth rates σ (in units of τ^{-1}) of eigenmodes with S2 symmetry as functions of Bu for $Ro = 0.05$ and $f/\bar{N} = 0.1$. The lines connecting the symbols are to "guide the eye". The eigenmodes with S2 symmetry are unstable in the range $Bu \lesssim 0.823$ (they are the fastest-growing for $0.2 \lesssim Bu \lesssim 0.823$). As Bu increases, the eigenmode changes from unstable to neutrally stable at $Bu \simeq 0.823$ (shown with the vertical broken line), but the family of eigenmodes does not terminate there. (b) The phase speed c (in units of τ^{-1}) corresponding to the growth rates shown in panel (a). The thick lines connecting the symbols are to "guide the eye". If (2.12) holds, the second neutrally stable eigenmode branch's eigenvalues can be calculated analytically (our calculations here show that A is quadratic in Bu and that B is linear in Bu). The thin line in the neutrally stable range shows the phase speed of this second neutrally stable eigenmode branch. Generically, we would expect A to be linear in Bu (and not quadratic). However our data indicates that A is quadratic in Bu. This suggests that due to the symmetries of the problem, there are degeneracies that cause this non-generic behavior. It may be that adding an asymmetry to the problem will unfold a degeneracy and make the problem generic. The phase speed is continuous when it passes through the vertical broken line, which is a necessary condition for the unstable and neutrally-stable eigenmodes to belong to the same family. Note that because our computation uses a small hyperdissipation, the "neutral" modes in panel (a) have a slight decay rate of $\sim 0.002\tau^{-1}$; however, as the value of the hyperdissipation decreases (with a corresponding increase in spatial resolution to prevent an accumulation of energy and enstrophy at the smallest resolvable length scales), so does the decay rate, suggesting that a dissipationless calculation would show that family of eigenmodes with $Bu > 0.823$ are truly neutral.

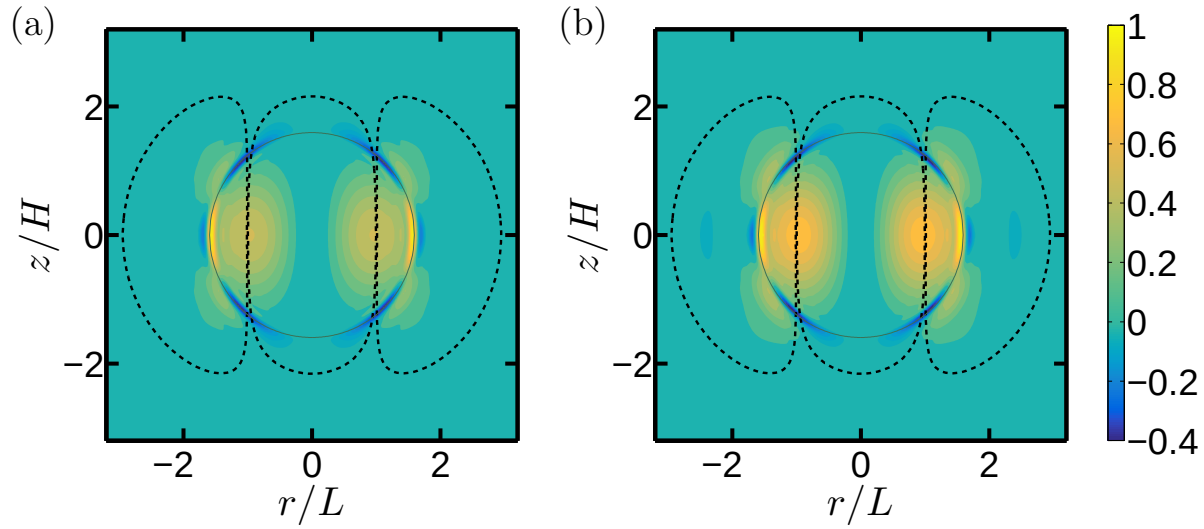

Figure 2.3: (Colour online) Vertical vorticity in the $(r-z)$ plane of two of the eigenmodes shown in figure 2.2, with medium shade being zero (cyan, in colour), light shade being the most cyclonic (yellow, in colour), and dark shade the most anticyclonic (blue, in colour). The center of each panel corresponds to the center of the unperturbed Gaussian vortex. The azimuthal angle of each panel was chosen so that the critical layer is prominent. The theoretical location of each critical layer is indicated by the continuous, nearly circular curve (dark green, in colour), which is where the phase speed c is equal to the azimuthal velocity of the unperturbed vortex. Both eigenmodes have S2 symmetry. (a) For the unstable eigenmode at $Bu = 0.7$. (b) For the neutrally-stable eigenmode at $Bu = 0.9$. The similarity of the radial structure of the unstable and neutrally-stable eigenmodes indicates that they are part of the same family and that the family does not terminate when the growth rate changes from positive to zero.

2.4 Parameter map of stability

Here, we explore the stability and linear growth rates of Gaussian vortices as functions of Ro and Bu for $f/\bar{N} = 0.1$. Like many other studies, for most cases we have used $f/\bar{N} = 0.1$, rather than $f/\bar{N} = 0.01$ (which is a better representative of the mid-latitude oceans, see Chelton et al. [1998]; Lelong & Sundermeyer [2005]), because small values of $f/\bar{N}$ are computationally expensive to tackle [see, e.g., Brunner-Suzuki et al. 2012; Tsang & Dritschel 2015]. However in this study, we use the semi-analytic method of Barranco & Marcus [2006], which allows us to compute flows efficiently for a wide range of $f/\bar{N}$, including the more physically relevant value of 0.01. Some cases are repeated with $f/\bar{N} = 0.01$ and discussed in §2.5. The results presented in this section are all obtained using the computational domain of $(30L) \times (30L) \times (30H)$ and resolution of 256^3.

For each of the vortices we examined, we computed the eigenvalues and eigenvectors (as given by (2.10)) of the fastest-growing eigenmode and also for the fastest-growing eigenmodes

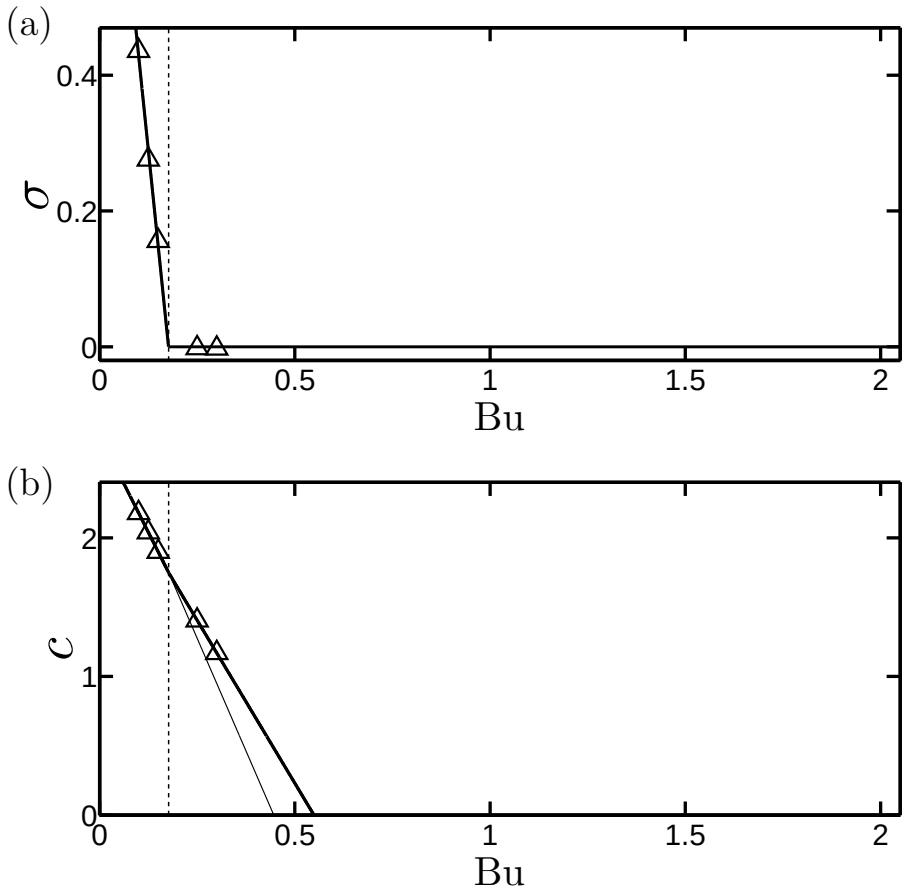

Figure 2.4: As in figure 2.2 but for the family of A1 eigenmodes that are the fastest growing for $Ro = 0.05$, $f/\bar{N} = 0.1$ and in the range $Bu \lesssim 0.2$. Triangles indicate the numerically computed values of σ and c. The eigenmode goes from unstable to neutrally stable at $Bu \simeq 0.177$, indicated by the vertical broken line. As in figure 2.2, the A has a non-generic quadratic behavior, which we use to plot the thin solid line in panel (b) to the right of the vertical dashed line.

of each of the six symmetry classes that could be computed by the simultaneous application of the spatial symmetrizer in z (which forced the eigenmode to be symmetric or anti-symmetric in z) and the azimuthal symmetrizer (which forced the eigenmode to have an odd azimuthal wave number m, or to have an even m that was not divisible by 4, or to have an even m that was divisible by 4). For some cases, the fastest-growing eigenmodes were also computed without a spatial symmetrizer, which were found to be identical (up to 3 significant digits) to the fastest-growing eigenmode of the six eigenmodes that were computed with one of the enforced symmetries.

The results are compared and contrasted with the most relevant published results obtained from analyzing the QG, shallow-water, and full Boussinesq equations in §2.4.

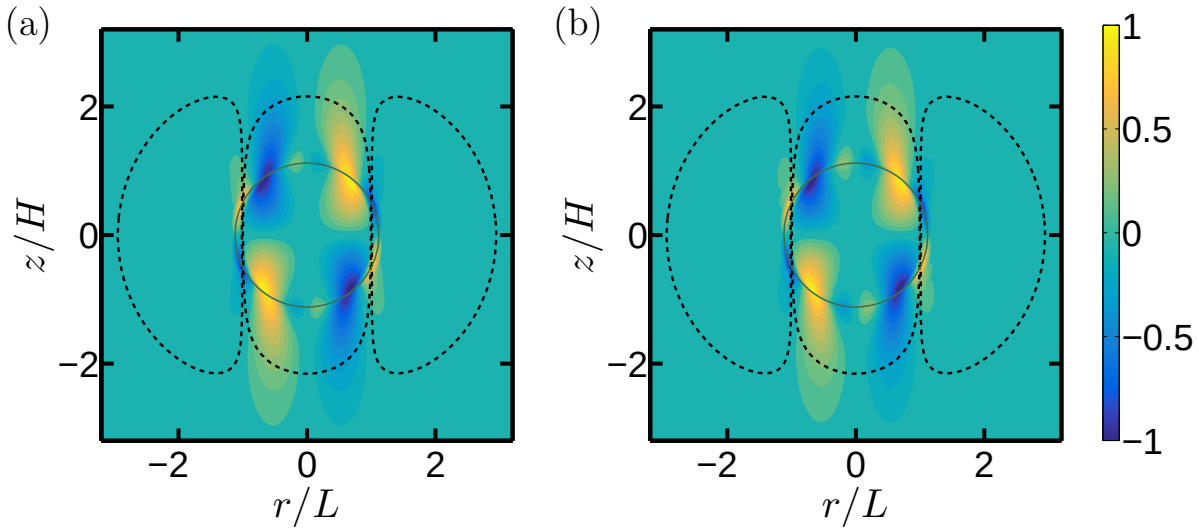

Figure 2.5: (Colour online) As in figure 2.3 but for two of the eigenmodes shown in figure 2.4 with A1 symmetry. (a) For the unstable eigenmode at $Bu = 0.15$. (b) For the neutrally-stable eigenmode at $Bu = 0.25$.

Spatial symmetries and growth rates of the eigenmodes

The parameter map of stability in the $Ro - Bu$ space is shown in figure 2.8(a). Gaussian anticyclones do not exist with $Ro < -0.5$ (see §2.2). The region to the lower left of the thick dashed black curve corresponds to equilibrium Gaussian vortices for which $N_c^2 < 0$ (or $Bu < -Ro(1 + Ro)$ according to (2.7)). These vortices are not unphysical, but near their cores they have heavy fluid above light fluid (i.e., $\partial\rho/\partial z > 0$ at the vortex center).

As shown in figure 2.8(a), the most unstable eigenmodes (i.e, those with the largest growth rates) of the vortices generally have either S2 or A1 symmetries. A few points in the figure correspond to vortices for which the fastest-growing eigenmode is A2, A3 or A4. We found that no vortex had a fastest-growing eigenmode with a symmetry different from those just listed. To our surprise, only 4 out of the 130 vortices that we examined were neutrally stable. All the neutrally-stable vortices were cyclones with $0.02 \lesssim Ro \lesssim 0.05$ and $0.8 \lesssim Bu \lesssim 1$. The neutrally-stable eigenmodes are denoted in figure 2.8(a) as solid circles in the region circumscribed by a small rectangle. The rectangle is to "guide the eye" and is used to denote the approximate boundary of the region of neutral stability. Computing the actual boundary between the regions where vortices are all neutrally stable and where they are unstable would be expensive and rather pointless given how small the neutrally-stable region is. Anticyclones have linear growth rates that are slow and would not destroy a vortex in less than 50 vortex turnaround times if $0.5 \lesssim Bu \lesssim 1.3$. For nearly geostrophic cyclones with $|Ro| < 0.05$, linear growth rates are slow and would not destroy a vortex in less than 50 vortex turnaround times if $0.7 \lesssim Bu \lesssim 1.2$. As Ro increases, the growth rates of large-diameter cyclones (i.e., with $Bu \lesssim 1.05$ or $L \gtrsim 0.98L_r$) becomes faster.

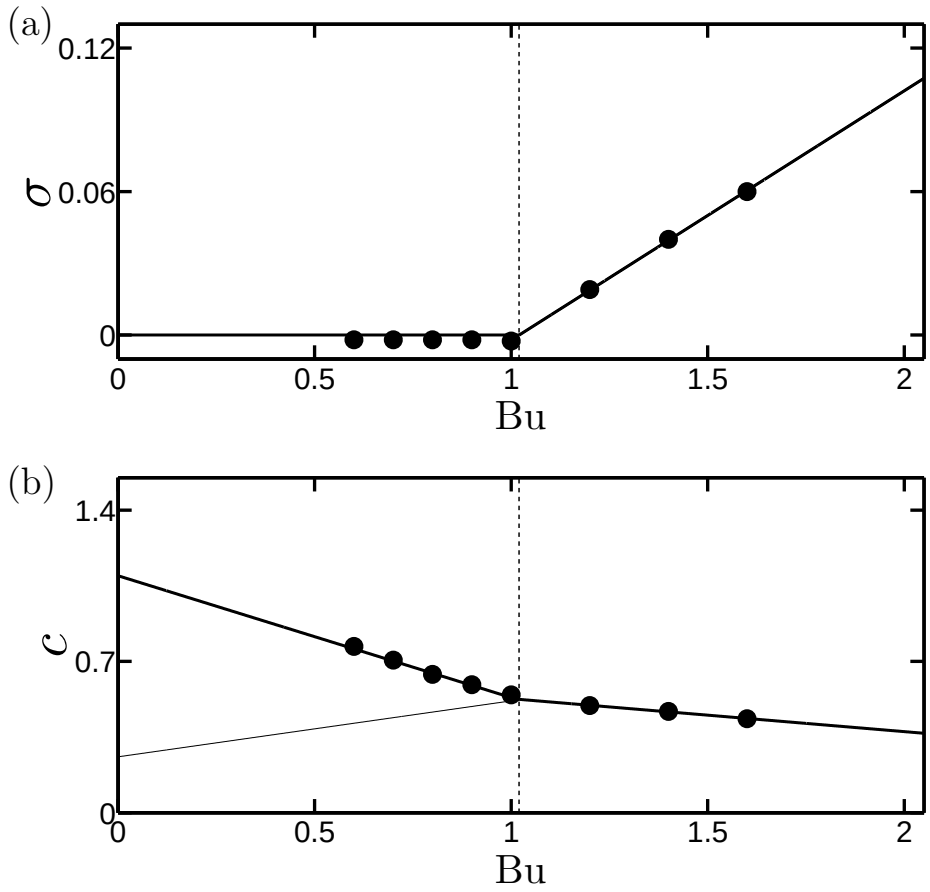

Figure 2.6: As in figure 2.2 but for the family of A1 eigenmodes that are the fastest growing for $Ro = 0.05$, $f/\bar{N} = 0.1$, and $Bu \gtrsim 1$. Solid circles indicate the numerically computed values of σ and c. The eigenmode goes from neutrally stable to unstable at $Bu \simeq 1.02$ indicated by the vertical broken line (for a description about the panel(b)'s thin solid line, see figure 2.2 and 2.4's captions). Also note that the families illustrated here and in figure 2.4 both have A1 symmetry, but they are different families.

Considering the smallness of the region of neutral stability, clearly, linear stability cannot be used to explain the differences between the numbers of observed cyclones and anticyclones in the oceans or in planetary atmospheres. On the other hand, ocean vortices can survive for more than 50 of their own turn-around times, τ. So, one plausible explanation of the cyclonic/anticyclonic asymmetry in the frequency of observation of mesoscale oceanic eddies and of planetary vortices might depend on the differences of the *growth rates* of the linear instabilities, rather than just the fact that some vortices are not linearly unstable and others are. For example, if there are physical processes (such as turbulence, interactions with other vortices or currents or boundaries) that are likely to destroy a vortex after 50 τ, which is more than $\sim 1/2$ year for ocean Meddies [McWilliams 1985; Armi et al. 1989; Hebert et al. 1990; Pingree & Le Cann 1993; D'Asaro et al. 1994; Prater & Sanford 1994; Paillet et al.

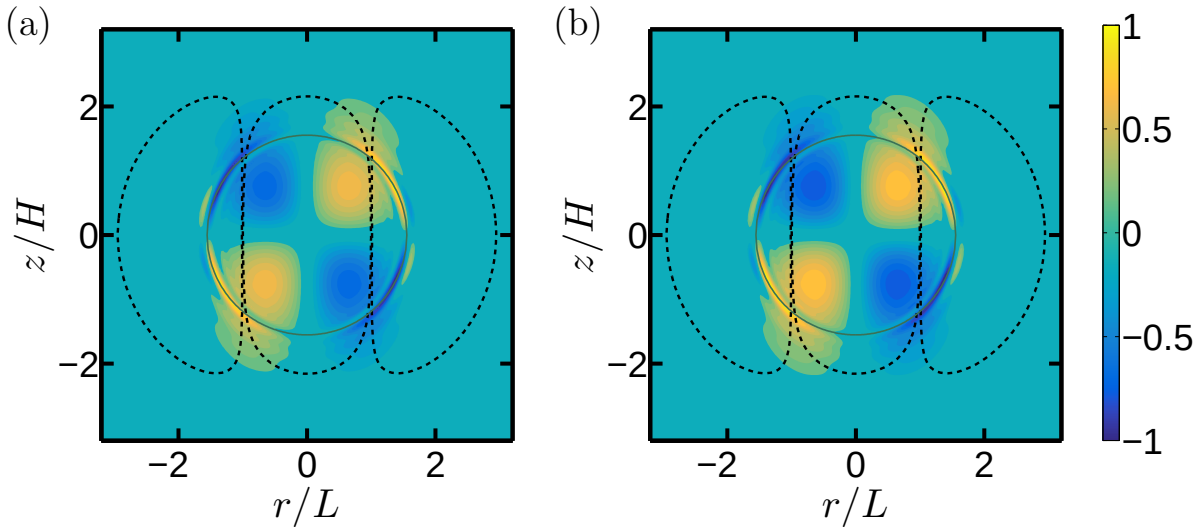

Figure 2.7: (Colour online) As in figure 2.3 but for two of the eigenmodes shown in figure 2.6 with A1 symmetry. (a) For the unstable eigenmode at $Bu = 1.2$. (b) For the neutrally-stable eigenmode at $Bu = 0.9$. Note that the eigenmodes illustrated here and in figure 2.5 both have A1 symmetry, but they are different eigenmodes.

2002], then a vortex need not be neutrally stable to be observed, it needs only have growth rates less than $\sim 1/50\,\tau^{-1}$. So, it is plausible that the asymmetry between the numbers of observed cyclones and anticyclones depends upon the relative amount of area in $Ro - Bu$ parameter space for which the fastest-growing eigenmodes grow slower than $\sim 1/50\,\tau^{-1}$, or some other critical growth rate. For Gaussian vortices, the region in $Ro - Bu$ parameter space where the growth rate of the fastest-growing eigenmode is less than $1/50\,\tau^{-1}$ (i.e., the "slow growth region" for linear instability) is the region bounded above by the solid (blue, in colour) and dotted (red, in colour) curves in figure 2.8(a) and to the lower left by the thick dashed curve. Along the solid curve (blue, in colour), the fastest-growing eigenmode has S2 symmetry, whereas along the dotted curve (red, in colour) it is A1. The solid and dotted curves are drawn to "guide the eye", and the vortices corresponding to the black solid circles have $\sigma < 1/50\,\tau^{-1}$. In general, for large Bu, the fastest-growing eigenmodes have A1 symmetry, while for smaller Bu, they have S2 symmetry. However, for cyclones with $Bu \lesssim 0.4$, some of the fastest-growing eigenmodes also have A1 symmetry, or even A2, A3 or A4 symmetry, and the growth rates are often faster than $1\,\tau^{-1}$. There are two regions in the $Ro - Bu$ parameter space where the fastest-growing eigenmodes of the cyclones have A1 symmetry. In the region with higher Bu, the growth rate of the fastest-growing modes is smaller than that in the lower Bu region, and, as discussed previously and elaborated on in §2.6, the radial structures of the fastest-growing A1 eigenmodes in the large and small Bu regions differ as well.

Of course, our choice of $50\,\tau$ to define the "slow growth region" for linear instability is

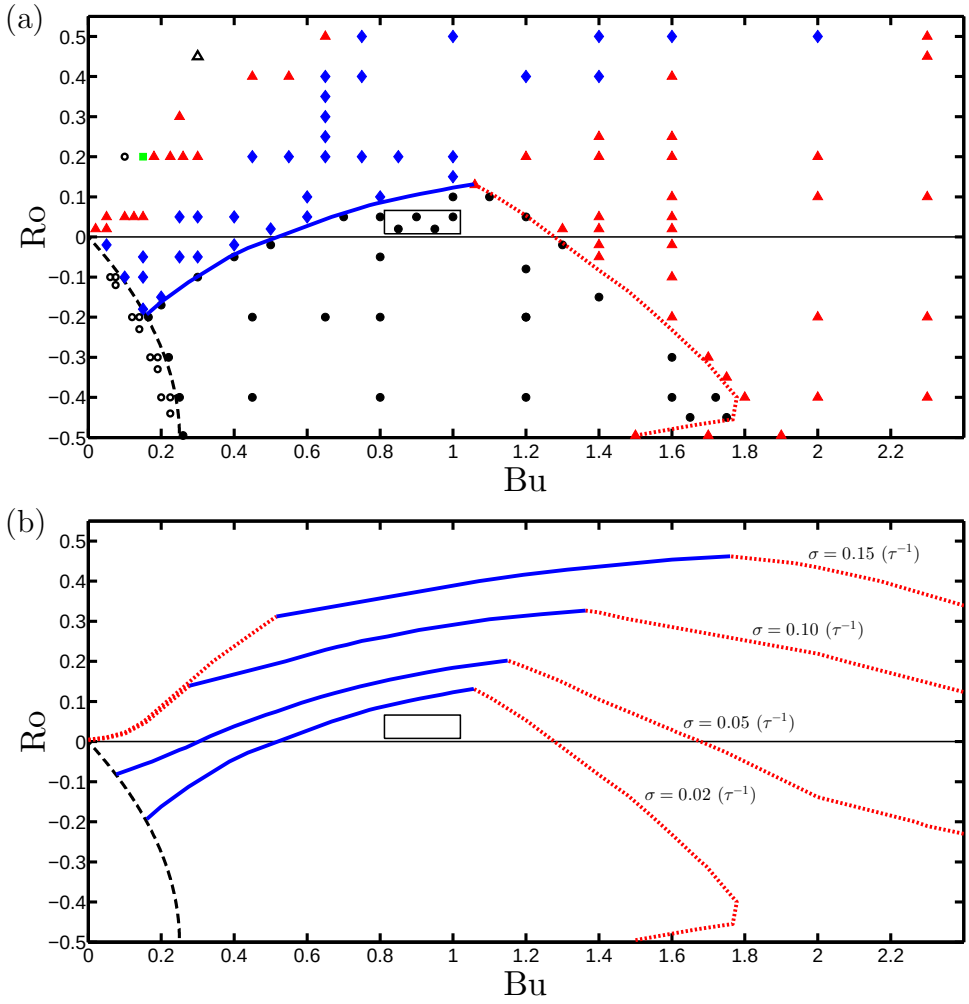

Figure 2.8: (Colour online) Parameter map of the stability of Gaussian vortices in the $Ro - Bu$ space. No equilibrium Gaussian vortices exist with $Ro < -0.5$. The thick black dashed line in the lower left corner indicates the locus over which $N_c^2 = 0$, i.e., $Bu = -Ro(1 + Ro)$, with $N_c^2 < 0$ for vortices with smaller Ro or Bu. Panel (a): The thick solid (blue, in colour) and thick dotted (red, in colour) lines indicate the iso-surface where σ of the fastest-growing eigenmode is $0.02\,\tau^{-1}$. The region bounded by this iso-surface, the thick black dashed curve (but see the caveat in the text describing figure 2.10), and the bottom of the figure has $\sigma < 0.02\,\tau^{-1}$ (the iso-contour is to "guide the eye" and is approximated by interpolating among the growth rates calculated at the locations of the discrete symbols). The symbols denote the spatial symmetry of the fastest-growing eigenmode, with diamonds (blue, in colour) as S2, solid triangles (red, in colour) as A1, squares (green, in colour) as A2, hollow triangles as A3, and hollow circles as A4. Black solid circles correspond to vortices for which the most unstable eigenmodes have growth rates slower than $0.02\,\tau^{-1}$. Panel (b): Four iso-contours (approximated as in (a)) of growth rate σ of the fastest-growing eigenmode. Each contour consists of one solid curve (blue, in colour) and one or two dotted curves (red, in colour). The fastest-growing eigenmodes along the dotted curves (red, in colour) have A1 symmetry and along the solid curves (blue, in colour) have S2 symmetry. The small rectangular box near $Bu = 1$ is to guide the eye and shows the approximate, very small, region where all of the eigenmodes of the cyclones are neutrally stable. The σ and the symmetries of the most unstable eigenmodes with $\sigma > 0.02\,\tau^{-1}$ for vortices with $N_c^2 > 0$ in panel (a) are given in Appendix E.

arbitrary, so figure 2.8(b) shows how the "slow growth" region changes when we change our choice from $50\,\tau$ to $20\,\tau$, $10\,\tau$, or $6.67\,\tau$. That is, the two sets of (solid/broken) curves are iso-surfaces in $Ro - Bu$ parameter space where σ is 0.02, 0.05, 0.1, and 0.15 in units of τ^{-1}. For the iso-surface for the growth rate of $0.15\,\tau^{-1}$ in figure 2.8(b), the fastest-growing eigenmode has S2 symmetry for $0.5 \lesssim Bu \lesssim 1.8$, otherwise the fastest-growing eigenmode has A1 symmetry. Note that the iso-surfaces for the growth rates of $0.10\,\tau^{-1}$ and $0.15\,\tau^{-1}$ are very close to each other for $Bu \lesssim 0.3$. Most of the fastest-growing eigenmodes in the $Ro - Bu$ parameter space shown in figure 2.8 have $\sigma < 0.2\,\tau^{-1}$. However, cyclones in the upper left corner of figure 2.8 can have σ of order one τ^{-1}. As shown below, anticyclones to the lower left of the thick dashed curve in the lower left side of figure 2.8 (with $N_c^2 < 0$) can have much larger σ.

The growth rates of the three fastest-growing eigenmodes for $Ro = 0.05$ as functions of Bu are plotted in figure 2.9(a) (combining figures 2.2, 2.4, and 2.6) showing that the fastest growing eigenmode is A1 for $Bu \lesssim 0.2$; is S2 for $0.2 \lesssim Bu \lesssim 0.8$; and is A1 for $1 \lesssim Bu \lesssim 2.1$. However, for $0.8 \lesssim Bu \lesssim 1$, the eigenmodes are all neutrally stable. This region of neutral stability is consistent with the neutrally stable region shown in figure 2.8. The change in the spatial symmetry from A1 to S2 back to A1 of the fastest growing eigenmode as Bu increases was discussed in §2.3 and it was shown that i) the family of eigenmodes continues to exist even after the eigenmodes become neutrally stable, and ii) the A1 modes at small and large Bu belong to two different families of eigenmodes. Similar changes in the symmetries of the most unstable mode are observed at $Ro = 0.2$ (figure 2.9(b)); however, at $Ro = 0.2$ there is not a region where the vortex is neutrally stable to all eigenmodes. Similar to $Ro = 0.05$, the two families of A1 eigenmodes shown in figure 2.9(b) with triangles and with filled circles are distinct families with different radial structures. How these results, particularly at the small Ro of 0.05, compare with those obtained, analyzing QG equations is discussed in the next subsection.

The growth rates for region with statically unstable vortex cores, i.e., with $N_c^2 < 0$, are shown in figure 2.10. Eigenmodes for this region have A4 symmetry and the growth rates can be as large as $\sim 100\,\tau^{-1}$. The σ as a function of Bu (for fixed Ro), and as a function of Ro (for fixed Bu) for vortices with $N_c^2 < 0$ are shown in figures 2.11(a) and (b), respectively. In each of the eight panels, the value of the horizontal coordinate axis on the right side of the panel corresponds to a vortex with $N_c^2 = 0$ (i.e., a point on the thick dashed curve in figure 2.8 or in the broken curve in figure 2.10). The figure shows that σ increases rapidly as a function of distance from the $N_c^2 = 0$ boundary. Due to this rapid growth in σ, for all practical purposes we can consider the thick dashed line at $N_c^2 = 0$ to be the left boundary of the region in figure 2.8(b) in $Ro - Bu$ for which $\sigma < 0.02\,\tau^{-1}$, and also the boundary for the region $0.02\,\tau^{-1} \le \sigma < 0.05\,\tau^{-1}$, and for the region $0.05\,\tau^{-1} \le \sigma < 0.10\,\tau^{-1}$.

Comparison with previous studies

As discussed in §2.1, this study extends the analyses of previous studies by using the full 3D non-hydrostatic Boussinesq equations and by employing the 3D Gaussian vortex model,

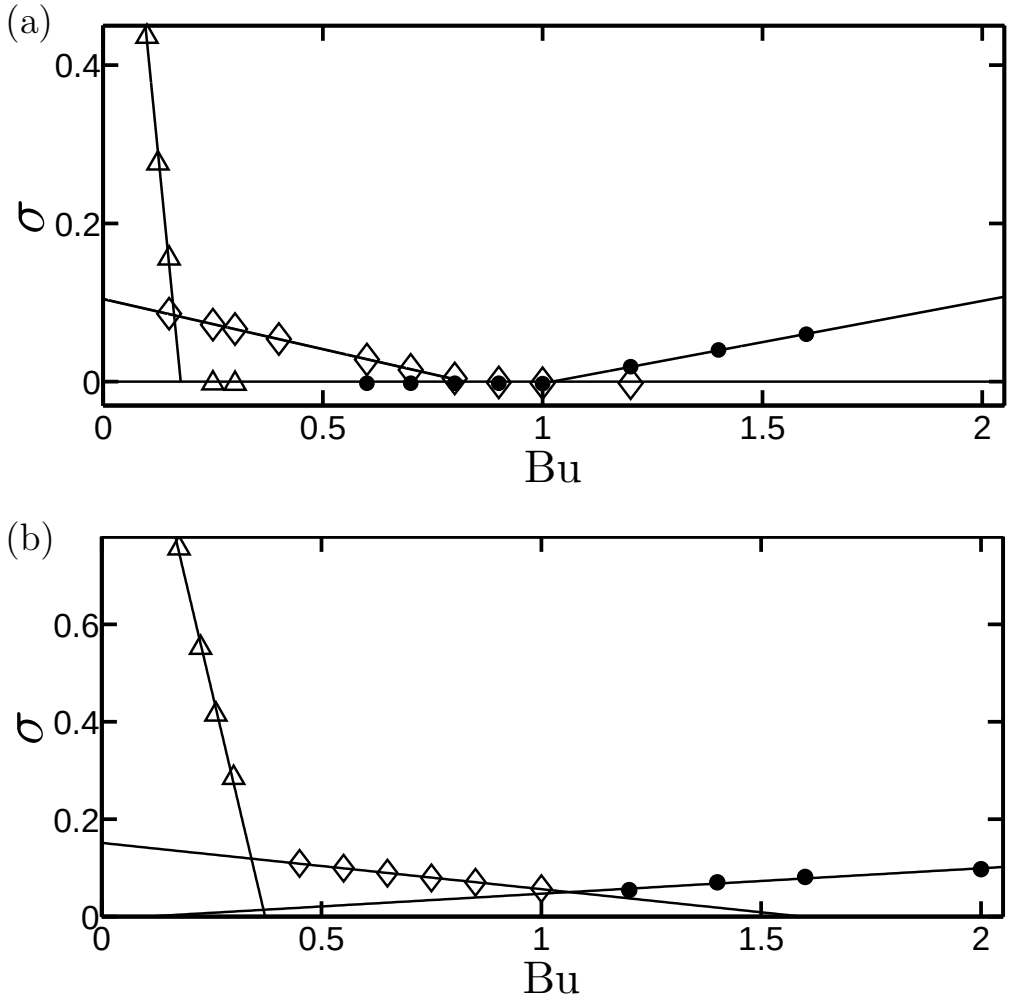

Figure 2.9: Growth rates σ (in units of τ^{-1}) of the three fastest-growing modes as functions of Bu for fixed Ro. $f/\bar{N} = 0.1$. Triangles, filled circles, and diamonds, respectively indicate the fastest growing eigenmodes at low Bu (which have A1 symmetry), the fastest growing eigenmodes at high Bu (which also have A1 symmetry), and the fastest growing eigenmodes for intermediate Bu (which have S2 symmetry). The three lines connecting the three sets of symbols are to "guide the eye" to show the three families of eigenmodes. (a) $Ro = 0.05$; In this case as Bu increases, the fastest-growing mode changes from A1 to S2; then all modes are linearly neutrally stable; then the fastest-growing mode is A1. (b) $Ro = 0.2$; the fastest-growing mode changes from A1 to S2 and again to A1 as Bu increases.

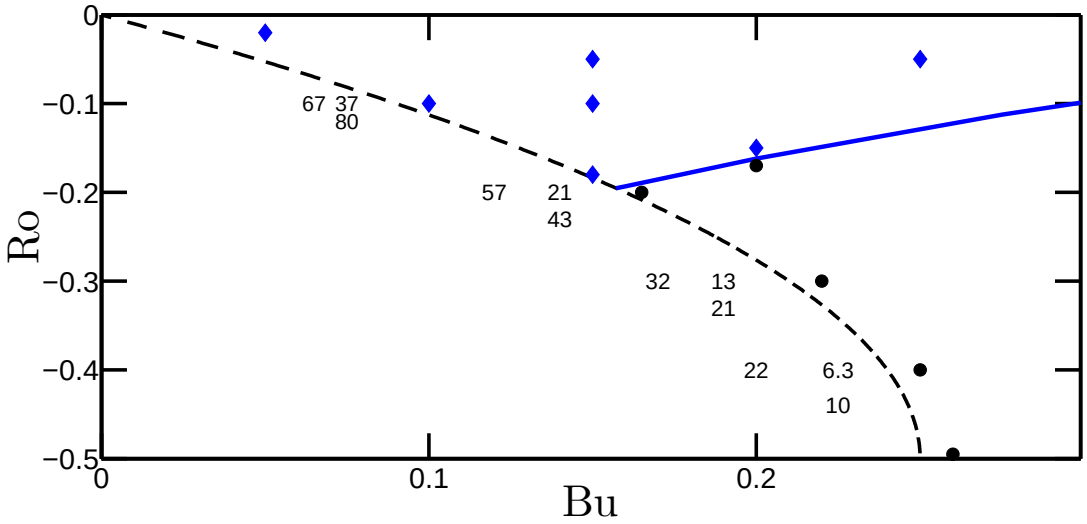

Figure 2.10: (Colour online) Blow up of the lower left corner of figure 2.8(a), showing details of the eigenvalues in the region where the Gaussian vortices have $N_c^2 < 0$. The axes of the figure, line styles, and symbols have the same meaning as they do in figure 2.8(a). In the lower left region, below the broken line, numbers rather than symbols are used to indicate where in parameter space we have carried out linear stability calculations. The numbers are the values σ (in units of τ^{-1}) of the fastest-growing eigenmode (which in all cases has an A4 symmetry).

which has continuous velocity and density (and PV) fields and is initially in exact equilibrium. The latter is necessary for a rigorous linear stability analysis. A comparison of our results with those of many previous studies is not straightforward because various different vortex models and flow models have been used. Below we compare our parameter map of stability with the results of the most relevant study in the QG limit [Nguyen et al. 2012] and with the results of several relevant studies using multi-layer models. We also discuss the results of Yim et al. [2016], who used the full Boussinesq equations but studied a different family of vortices.

In the limit of vanishing Ro, the most relevant study to ours is that of Nguyen et al. [2012], who numerically calculated the unstable modes of a Gaussian vortex using the QG equations. They found that the fastest-growing mode changes from S2 to A1 around $Bu = 1$, which along with the general dependence of the growth rate of the fastest-growing mode on Bu in their figure 1(a) agrees overall with the results of current study (see figure 2.9(a) which is for $Ro = 0.05$). However, they also found that for Bu as small as 0.05, modes with higher m dominate. In our results, for anticyclones, as Bu decreases, the most unstable mode changes from S2 to A4 once the vortex becomes statically unstable (this instability is not considered in the QG framework used by Nguyen et al. [2012]). For cyclones, as Bu decreases, the most unstable mode changes from S2 to A1 for small Ro and to A2 or A3 for moderate Ro (see figure 2.8).

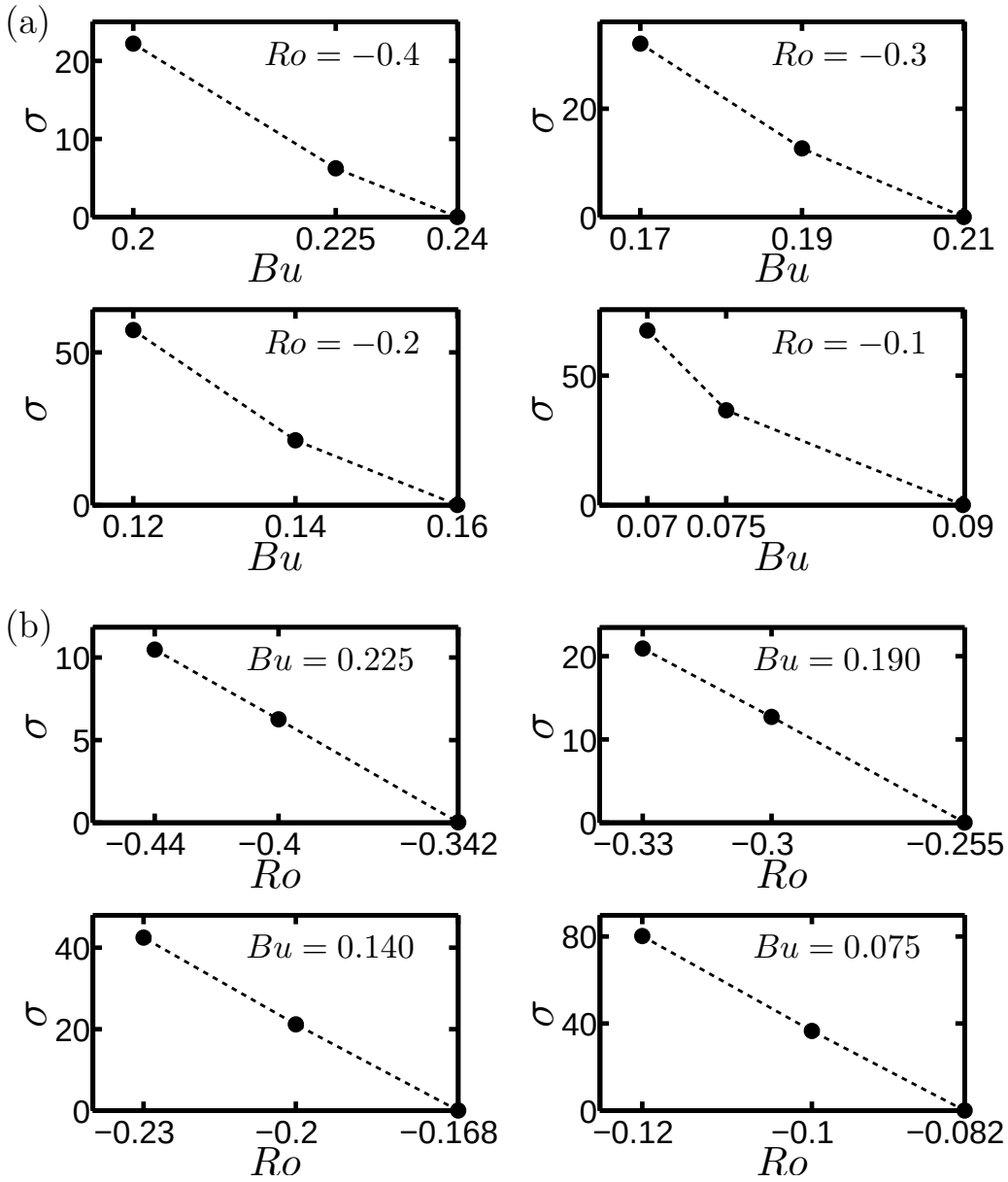

Figure 2.11: Growth rates (in units of τ^{-1}) for the most unstable eigenmode of vortices with $N_c^2 < 0$ for fixed Ro and Bu. $f/\bar{N} = 0.1$. For all vortices examined in this region, the fastest-growing eigenmode has A4 symmetry; Panel (a): σ as a function of Bu for $Ro = -0.4$, -0.3, -0.2 and -0.1; Panel (b): σ as a function of Ro for $Bu = 0.225$, 0.19, 0.14 and 0.075. In each panel, the value of the horizontal coordinate axis on the right side of the panel corresponds to a vortex with $N_c^2 = 0$. The dotted lines are to "guide the eye".

There are a number of studies which have used the shallow-water equations with the Gaussian vortex model and are relevant to current work. Consistent with the results of our analysis, these studies find that anticyclones become more stable as the absolute value of the Rossby number increases, whereas for cyclones the growth rates decrease with decreasing the Rossby number [Stegner & Dritschel 2000; Baey & Carton 2002; Benilov & Flanagan 2008]. (In this section note that our results are only for vortices with stably-stratified interiors.)

How the growth rates in these studies vary with the Burger number, however, shows a strong dependence on the vertical structure of the vortex and the background flow. Stegner & Dritschel [2000] studied the stability of isolated Gaussian vortices using a $1 - 1/2$ layer model and found that for vortices with small Rossby numbers, the growth rate decreases with decreasing the Burger number. This is consistent with our results only for $Bu \gtrsim 1$. Benilov & Flanagan [2008] used a two-layer model to examine the stability of the "compensated" (i.e., $\boldsymbol{v} = \boldsymbol{0}$ in the bottom layer) Gaussian vortices, and also Gaussian vortices with uniform PV in the lower layer. They found that compensated vortices are neutrally stable for intermediate Burger numbers, while vortices with uniform PV in the lower layer are neutrally stable for Burger numbers smaller than a critical value of order 1. Baey & Carton [2002] studied two-layer Gaussian vortices and found, in contrast to the previous results and those of ours, that the growth rate decreases with Burger number for both cyclones and anticyclones and the eigenmodes are stable for Burger numbers larger than a critical value. It is apparent that identifying a unique stability behavior with Burger number in these studies is difficult and the behavior is highly dependent on the vertical structure of the flow/vortex. An example of such dependence is given by Sutyrin [2015], who examined two and three layer compensated shallow water vortices and showed that the addition of a third middle layer with uniform PV weakens the coupling between the upper and lower layers and enhances the stability of vortices. Considering these results, comparing the Burger number dependence of the stability behavior of 3D vortices in continuously-stratified Boussinesq flows and vortices in shallow water and layer models is not particularly useful.

Only few studies have used the full Boussinesq equations, and even those have focused on very different vortex models such as barotropic Taylor columns [Smyth & McWilliams 1998], evolving (out-of-equilibrium) 3D vortices interacting with large-scale internal waves [Brunner-Suzuki et al. 2012], out-of-equilibrium, ellipsoidal 3D vortices with discontinuous PV profiles [Tsang & Dritschel 2015], and 3D equilibrium vortices with Gaussian angular velocity [Yim et al. 2016]. Here we focus on the latter, because the main difference between our analysis and that of Yim et al. [2016] is in the vortex model: Gaussian pressure anomaly in the current study versus their Gaussian angular velocity (also note that the flow in their study is not inviscid). Such comparison provides some understanding of how the stability properties depend on the vortex profile.

Yim et al. [2016] conducted a linear stability analysis of 3D equilibrium vortices with Gaussian angular velocity in unbounded, rotating, stratified flows for a wide range of Rossby number, $|Ro| \leq 20$. Here we only focus on their results for $|Ro| \leq 0.5$ and inviscid and non-diffusive flows, which are relevant to the present study. Consistent with our results, for $Bu \gtrsim 1$, they found A1 as the most unstable mode for both cyclones and anticyclones

(their figures 39(d) and (f)), which they attributed to the instability mechanism of Gent & McWilliams [1986] (this is also consistent with the results of Smyth & McWilliams [1998] for Taylor columns). For $Bu \lesssim 1$, Yim et al. [2016] found anticyclones neutrally stable for $0.5 \lesssim Bu \lesssim 1$ (while we found them weakly unstable), and they found S2 as the most unstable mode for anticyclones between the statically-unstable region and $Bu \sim 0.4 - 0.5$ (depending on Ro), which is consistent with our results. For cyclones with $Bu \lesssim 1$, Yim et al. [2016] found a neutrally-stable region between $0.5 \lesssim Bu \lesssim 1$ (variable with Ro), which is much larger than (and encompasses) the neutrally-stable region we found; they also found that as Bu decreases from one, modes with $m = 2$ become the most unstable ones before modes with $m = 1$ also becoming unstable at lower Bu, which is overall consistent with our results. At Bu as low as 0.3, the family of vortices studied by Yim et al. [2016] can have statically-unstable cyclones, while cyclones in the family of vortices we studied are always statically stable. The comparison of the results of the current study and those of Yim et al. [2016], as summarized above, suggests that for these two vortex families, while the linear stability properties are not sensitive to the vortex profile for $Bu \gtrsim 1$, the stability properties strongly depend on the vortex profile for $Bu \lesssim 1$. Whether this behavior is generic or not requires further studies with other vortex families.

2.5 Effect of $f/\bar{N}$ on linear stability

Despite the fact that $f/\bar{N}$ is of order 0.01 in the mid-latitude oceans [Chelton et al. 1998; Sundermeyer & Lelong 2005], $f/\bar{N} \sim 0.1$ is commonly used in studies of the oceanic vortices to reduce the computational cost; small values of $f/\bar{N}$ in explicit codes makes the equations of motion numerically "stiff", which means they must be computed with small time steps. In this study calculations are done with $f/\bar{N} = 0.1$ for the purpose of sweeping a large region of the $Ro - Bu$ parameter space and comparing our results with those of others who have used this value.

Several other studies [Smyth & McWilliams 1998; Sundermeyer & Lelong 2005; Brunner-Suzuki et al. 2012; Dritschel & Mckiver 2015; Tsang & Dritschel 2015] have shown numerically that the stability properties and some aspects of the dynamics of vortices in rotating, stratified flows are not very sensitive to the specific value of $f/\bar{N}$ as long as this value is small. Here, we show numerically that the eigenvectors and eigenvalues of Gaussian vortices (with $N_c^2 > 0$), when properly scaled, are nearly independent of $f/\bar{N}$ for small $f/\bar{N}$. Furthermore, by properly non-dimensionalizing the linearized equations of motion, we explain the insensitivity of the eigenvalues and eigenvector structures of the fastest-growing modes to the value of $f/\bar{N}$.

Exploiting our semi-analytic method that enables us to accurately and efficiently deal with large $f\Delta t$ and $\bar{N}\Delta t$, we have repeated over 40 of the simulations with $f/\bar{N} = 0.01$. Table 2.1 shows the linear growth rate and the spatial symmetry of the fastest-growing eigenmode of several Gaussian vortices for $f/\bar{N} = 0.1$ and $f/\bar{N} = 0.01$. The symmetries are the same in all cases, as are the growth rates (in units of τ^{-1}) within 4%. Figure 2.12 shows examples of the most unstable eigenvectors (with dimension in z scaled by H, and

		$f/\bar{N}=0.1$		$f/\bar{N}=0.01$	
Ro	Bu	Symmetry	σ	Symmetry	σ
$+0.45$	0.3	A3	1.5	A3	1.5
$+0.4$	1.2	S2	0.14	S2	0.14
$+0.4$	1.6	A1	0.13	A1	0.13
$+0.2$	0.15	A2	1.1	A2	1.1
$+0.2$	1.0	S2	0.058	S2	0.058
$+0.2$	2.0	A1	0.097	A1	0.098
$+0.05$	1.4	A1	0.040	A1	0.039
$+0.02$	0.5	S2	0.029	S2	0.029
-0.02	1.4	A1	0.028	A1	0.028
-0.18	0.15	S2	0.024	S2	0.023
-0.2	0.45	-	< 0.02	-	< 0.02
-0.2	2.0	A1	0.042	A1	0.043
-0.3	1.6	-	< 0.02	-	< 0.02
-0.4	1.72	-	< 0.02	-	< 0.02
-0.4	1.8	A1	0.021	A1	0.021

Table 2.1: Comparison of the linear growth rates (in units of τ^{-1}) and symmetries of the most unstable eigenmode of selected Gaussian vortices in the $Ro - Bu$ space for $f/\bar{N} = 0.1$ and $f/\bar{N} = 0.01$.

dimensions of r, x, and y scaled by L). The eigenmodes are nearly indistinguishable for $f/\bar{N} = 0.1$ and $f/\bar{N} = 0.01$.

The insensitivity to $f/\bar{N}$ is easily explained by non-dimensionalizing the equations of motion (2.1) with $4\pi/\omega_c \equiv \tau$ as the unit of time, L as the unit of horizontal length, H as the unit of vertical length, L/τ as the unit of horizontal velocity, H/τ as the unit of vertical velocity, $\rho_o f L^2/\tau$ as the unit of pressure, ρ_o as the unit of density, and $fL^2/(H\tau)$ as the unit of buoyancy. In the following equations, asterisk superscripts indicate the non-dimensionalized quantity or operator

$$\left(\frac{Ro}{2\pi}\right)\left[\frac{\partial v_r^*}{\partial t^*} + v_r^*\frac{\partial v_r^*}{\partial r^*} + \frac{v_\phi^*}{r^*}\frac{\partial v_r^*}{\partial \phi} + v_z^*\frac{\partial v_r^*}{\partial z^*} - \frac{v^{*2}_\phi}{r^*}\right] = -\frac{\partial p^*}{\partial r^*} + v_\phi^*, \tag{2.13}$$

$$\left(\frac{Ro}{2\pi}\right)\left[\frac{\partial v_\phi^*}{\partial t^*} + v_r^*\frac{\partial v_\phi^*}{\partial r^*} + \frac{v_\phi^*}{r^*}\frac{\partial v_\phi^*}{\partial \phi} + v_z^*\frac{\partial v_\phi^*}{\partial z^*} + \frac{v_r^* v_\phi^*}{r^*}\right] = -\frac{1}{r^*}\frac{\partial p^*}{\partial \phi} - v_r^*, \tag{2.14}$$

$$\left(\frac{Ro}{2\pi}\right)(Bu)\left(\frac{f}{\bar{N}}\right)^2\left[\frac{\partial v_z^*}{\partial t^*} + v_r^*\frac{\partial v_z^*}{\partial r^*} + \frac{v_\phi^*}{r^*}\frac{\partial v_z^*}{\partial \phi} + v_z^*\frac{\partial v_z^*}{\partial z^*}\right] = -\frac{\partial p^*}{\partial z^*} + b^*, \tag{2.15}$$

$$\left(\frac{Ro}{2\pi Bu}\right)\left[\frac{\partial b^*}{\partial t^*} + v_r^*\frac{\partial b^*}{\partial r^*} + \frac{v_\phi^*}{r^*}\frac{\partial b^*}{\partial \phi} + v_z^*\frac{\partial b^*}{\partial z^*}\right] = -v_z^*, \tag{2.16}$$

$$\frac{v_r^*}{r^*} + \frac{\partial v_r^*}{\partial r^*} + \frac{1}{r^*}\frac{\partial v_\phi^*}{\partial \phi} + \frac{\partial v_z^*}{\partial z^*} = 0. \tag{2.17}$$

Only (2.15) depends on $f/\bar{N}$. For $f/\bar{N} \leq 0.1$ and for Burger numbers of order unity or less, the left side of (2.15) is of order 10^{-3}, whereas the two terms on the right side are both of order unity *if* we have chosen "proper" units of length, time, and mass in our non-dimensionalization such that the dimensionless quantities denoted with asterisk superscripts and their derivatives with respect to the dimensionless length and time inside the square brackets are of order unity or less. Thus those two terms nearly cancel each other, or

$$\frac{\partial p^*}{\partial z^*} = b^* + O(10^{-3}). \tag{2.18}$$

So, hydrostatic equilibrium is enforced to one part in a thousand. Thus, replacing the dynamic equation (2.15) with the kinematic equation (2.18) is a very good approximation, and with the replacement, the equations of motion are formally independent of $f/\bar{N}$. However, the argument above is not particularly useful because there is no *a priori* way of knowing that we chose "proper" units, and, in fact, for many types of waves, with this choice of units, the dimensionless expressions inside the square brackets are much greater than unity, and the waves are not in hydrostatic balance and the value of $f/\bar{N}$ is important.

However, with the choice of units above, the dimensionless form of our initial Gaussian equilibrium vortices is

$$\hat{p}^* = (-\pi)(1+Ro)\chi^*(r^*,z^*), \tag{2.19}$$

$$\hat{v}^*_\phi = \left(\frac{\pi}{Ro}\right)(r^*)\left(-1+\sqrt{1+4Ro(1+Ro)\chi^*(r^*,z^*)}\right), \qquad \hat{v}^*_r = \hat{v}^*_z = 0, \tag{2.20}$$

$$\hat{b}^* = (2\pi)(1+Ro)z^*\chi^*(r^*,z^*), \tag{2.21}$$

where $\chi^* \equiv \exp\left[-(r^*)^2-(z^*)^2\right]$. Note that the vortices depend on Ro, but not on $f/\bar{N}$ or Bu. Also note that as $Ro \to 0$, the equilibrium velocity $\hat{v}^*_\phi \to 2\pi r^*\chi^*(r^*,z^*)$ and remains of order unity or less. The equilibrium p^* and b^* are also of order unity or less for $|Ro|$ of order unity or less.

The non-dimensional equations linearized around the non-dimensional Gaussian vortex are (after dropping the asterisk superscripts and writing $\boldsymbol{v} = \hat{\boldsymbol{v}} + \tilde{\boldsymbol{v}}$, $p = \hat{p} + \tilde{p}$, and $b = \hat{b} + \tilde{b}$, where tilde denotes the linear eigenmode)

$$\left(\frac{Ro}{2\pi}\right)\left[\frac{\partial \tilde{v}_r}{\partial t} + \left(\frac{\hat{v}_\phi}{r}\right)\frac{\partial \tilde{v}_r}{\partial \phi} - \left(\frac{2\hat{v}_\phi \tilde{v}_\phi}{r}\right)\right] = -\frac{\partial \tilde{p}}{\partial r} + \tilde{v}_\phi, \tag{2.22}$$

$$\left(\frac{Ro}{2\pi}\right)\left[\frac{\partial \tilde{v}_\phi}{\partial t} + \left(\frac{\hat{v}_\phi}{r}\right)\frac{\partial \tilde{v}_\phi}{\partial \phi} + \left(\frac{\partial \hat{v}_\phi}{\partial r}\right)\tilde{v}_r + \left(\frac{\partial \hat{v}_\phi}{\partial z}\right)\tilde{v}_z + \left(\frac{\hat{v}_\phi}{r}\right)\tilde{v}_r\right] = -\frac{1}{r}\frac{\partial \tilde{p}}{\partial \phi} - \tilde{v}_r, \tag{2.23}$$

$$(Ro)\,(Bu)\left(\frac{f}{\bar{N}}\right)^2\left(\frac{1}{2\pi}\right)\left[\frac{\partial \tilde{v}_z}{\partial t} + \left(\frac{\hat{v}_\phi}{r}\right)\frac{\partial \tilde{v}_z}{\partial \phi}\right] = -\frac{\partial \tilde{p}}{\partial z} + \tilde{b}, \tag{2.24}$$

$$\left(\frac{Ro}{2\pi Bu}\right)\left[\frac{\partial \tilde{b}}{\partial t} + \left(\frac{\hat{v}_\phi}{r}\right)\frac{\partial \tilde{b}}{\partial \phi} + \left(\frac{\partial \hat{b}}{\partial r}\right)\tilde{v}_r + \left(\frac{\partial \hat{b}}{\partial z}\right)\tilde{v}_z\right] = -\tilde{v}_z, \tag{2.25}$$

$$\frac{\tilde{v}_r}{r} + \frac{\partial \tilde{v}_r}{\partial r} + \frac{1}{r}\frac{\partial \tilde{v}_\phi}{\partial \phi} + \frac{\partial \tilde{v}_z}{\partial z} = 0. \tag{2.26}$$

For the fastest-growing eigenmodes of vortices with $N_c^2 > 0$, we have numerically computed the dimensionless values of the quantities inside the square brackets and found them to be of order unity or less for all of the eigenmodes represented in figure 2.8. This calculation shows that for vortices whose interior is statically stable, the fastest-growing eigenmodes are in vertical hydrostatic balance and therefore explains why the non-dimensionalized eigenvalues and eigenmodes are insensitive to the value of $f/\bar{N}$ for $f/\bar{N} \lesssim 0.1$. It should be emphasized that we could not assume *a priori* that the fastest-growing eigenmodes of our vortices are in hydrostatic balance. Here we have numerically tested and verified the validity of this assumption. It is worth mentioning that non-hydrostatic effects can be important in the dynamics and evolutions of some geophysical and astrophysical vortices; for example, our previous calculations of vortices [Marcus & Hassanzadeh 2014], especially the longevity of the Great Red Spot (GRS) of Jupiter (and we remind the reader that longevity of vortices was the motivation of the study), showed that small departures from vertical hydrostatic equilibrium caused large changes to the lifetime of the GRS (albeit, due to nonlinear effects).

Finally, it is not surprising that for vortices with statically-unstable interiors ($N_c^2 < 0$), the terms in the square brackets are large and therefore the most unstable eigenmodes are *not* in hydrostatic balance. We have not carried out further eigenmode calculations with $f/\bar{N} = 0.01$ in this region because they are computationally very expensive.

2.6 Radial and vertical structure of the unstable eigenmodes

In this section we investigate the radial distribution of vorticity in the fastest-growing eigenmodes. The spatial distribution of these eigenmodes can be characterized quantitatively by determining the fractional amounts of its vertical enstrophy that are within the Gaussian vortex's core S_{core} and within its shield S_{shield}, where we use the definitions of *core* and *shield* given in Appendix A:

$$S_{core} \equiv \frac{\int_{core} |\omega_{eig}|^2 \, d^3x}{\int |\omega_{eig}|^2 \, d^3x}, \tag{2.27}$$

$$S_{shield} \equiv \frac{\int_{shield} |\omega_{eig}|^2 \, d^3x}{\int |\omega_{eig}|^2 \, d^3x}, \tag{2.28}$$

where ω_{eig} is the vertical vorticity of the eigenmode, the integrals in the numerators of (2.27) and (2.28) are over the core and shield respectively of the unperturbed vortex, and where the integrals in the denominators are taken over the entire computational domain. Not surprisingly, $S_{core} + S_{shield} > 0.95$, meaning that eigenmodes do not effectively extend radially beyond the shield of the unperturbed vortex. Figures 2.13 and 2.14 show that the radial structure of the fastest-growing mode depends in a simple way on its vertical and azimuthal symmetry. Figure 2.13(a) is a simplified version of figure 2.8(a) and divides the

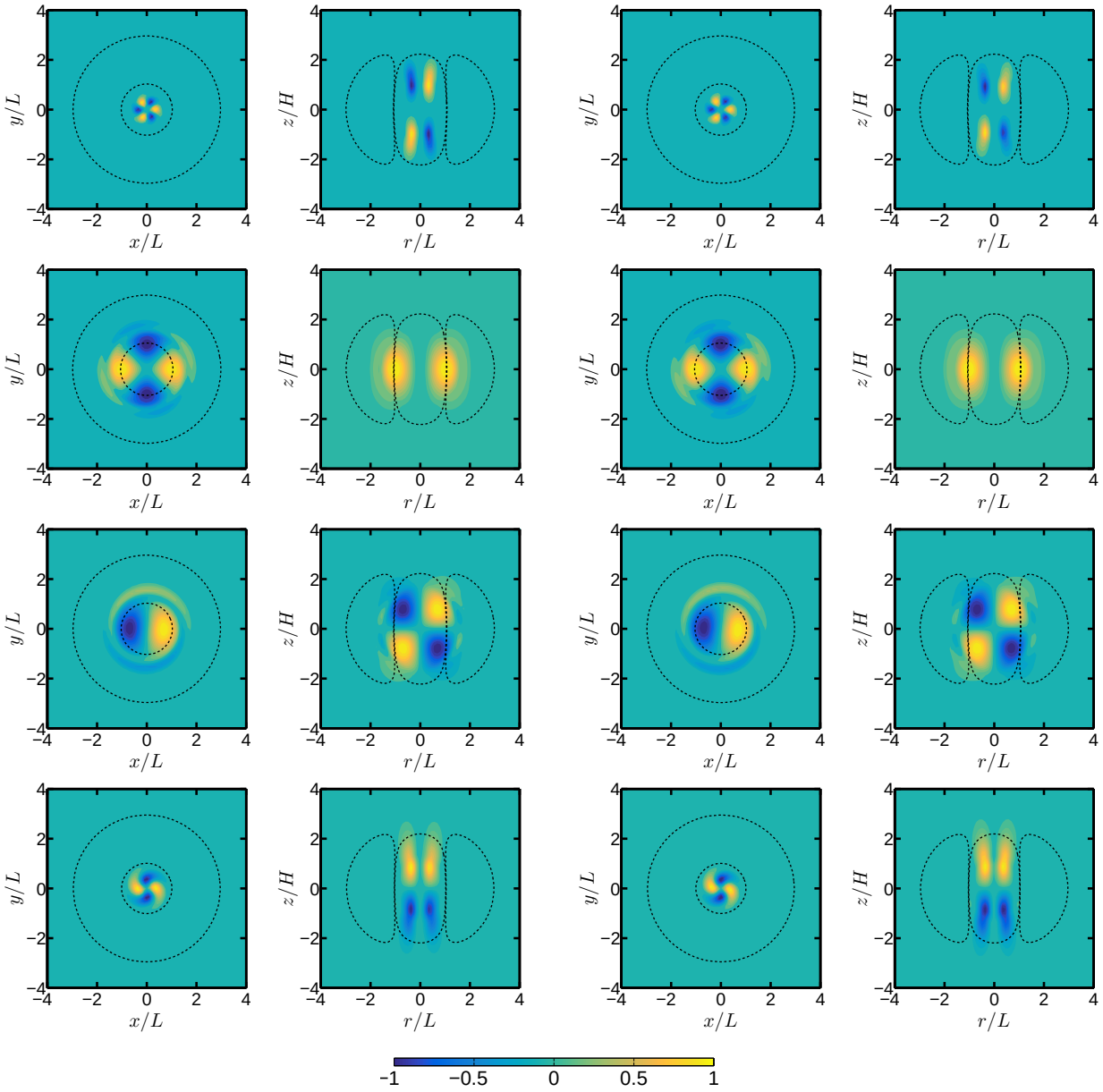

Figure 2.12: (Colour online) Vertical vorticity of eigenmodes normalized such that the maximum value of $|\omega|$ is 1. The eigenmodes are virtually indistinguishable for $f/\bar{N} = 0.1$ and $f/\bar{N} = 0.01$. The four rows from top to bottom correspond to the first four rows in table 2.1. The broken lines denote the boundaries of the core and shield of the unperturbed Gaussian vortex. In each row, the left two panels are for $f/\bar{N} = 0.1$ and the right two are for $f/\bar{N} = 0.01$. The first and third panels in each row show the eigenmodes in the x-y plane for a fixed z. For the z-symmetric eigenmode in the second row, this fixed value is $z = 0$. For the anti-symmetric eigenmodes in rows 1, 3, and 4, the fixed value of z is the positive value of z at which $|\omega|$ of the eigenmode obtains its maximum value. The second and fourth panels in each row show the eigenmodes in the r-z plane for fixed azimuthal angle ϕ. In all cases, ϕ is chosen so that it is the angle at which ω of the eigenmode obtains its maximum value.

$Ro - Bu$ space into 5 regions. The two unlabeled regions correspond to the region with $N_c^2 < 0$, and to the region of slow growth with $\sigma \leq 0.02\,\tau^{-1}$.

The three regions labeled $A1$, $S2$, and A, correspond accordingly to the vertical-azimuthal symmetry of the fastest-growing eigenmodes with the region labeled A having fastest-growing eigenmodes that are anti-symmetric in z with an azimuthal wave number m of 1, 2, 3 or 4. The fastest-growing eigenmodes in the $A1$ region are always (that is, for the vortices illustrated in figure 2.8(a)) concentrated radially in the core with $0.71 \leq S_{core} \leq 0.75$. The A1 eigenmode indicated by the label (f) in figure 2.13 is shown in the two panels labeled (f) in figure 2.14, which clearly show the radial concentration of the eigenmode in the core. The fastest-growing eigenmodes in the A region of figure 2.13(a) are even more strongly concentrated in the core and have $S_{core} > 0.87$. The A1 eigenmode of the cyclone indicated by the label (e) in figure 2.13 is shown in the two panels labeled (e) in figure 2.14, which show the concentration in the core. In contrast, the fastest-growing eigenmodes in the S2 region are either radially concentrated in the shield or are spread throughout the core and shield. Figure 2.13(b) is a blow-up of figure 2.13(a) and shows iso-contours of S_{shield}, which varies in the region of $Ro - Bu$ space that we examined from 0.95 at low Bu to 0.55 at high Bu. Thus, for low values of Bu, the fastest-growing S2 eigenmodes are very concentrated in the shields, and as Bu increases, the radial structure spreads into the core such that for the largest values of Bu that we examined, the eigenmode is approximately equally spread between the shield and core. The radial dependence on Bu of the S2 eigenmodes is illustrated in panels (a)-(d) in figure 2.14. The implications of the spatial structure of the most unstable eigenmodes will be discussed in the subsequent chapter that is focused on the nonlinear evolution of these vortices and is outlined in the Discussion.

2.7 Discussion and summary

We have studied the linear stability of 3D axisymmetric Gaussian vortices as a function of their Rossby number, Ro, and Burger number, Bu, over the wide range of values where long-lived geophysical and astrophysical vortices are often observed ($-0.5 < Ro < 0.5$ and $0.02 < Bu < 2.3$). For each (Ro, Bu), the growth rate, σ, and the eigenvector of the most unstable eigenmode have been calculated by numerically solving the 3D non-hydrostatic Boussinesq equations.

The results of the stability analysis are summarized in the $Ro - Bu$ parameter map (figure 2.8). These results show that neutrally-stable (i.e., $\sigma = 0$) cyclones only exist over a small region of the parameter space where $Ro \sim 0.02 - 0.05$ and $Bu \sim 0.85 - 0.95$; we do not find any neutrally-stable anticyclone. On the other hand, the most unstable eigenmodes of anticyclones generally have slower growth rates compared to those of the cyclones. Over a large region of the $Ro - Bu$ parameter space (mainly $Ro < 0$ and $0.5 \lesssim Bu \lesssim 1.3$), the maximum growth rates of the anticyclones are smaller than 50 turn-around time (τ) of the vortex. For $Bu \gtrsim 1.3$, the maximum growth rate of anticyclones increases (decreases) with increasing Bu ($|Ro|$). In this region, the eigenvector of the most unstable modes is

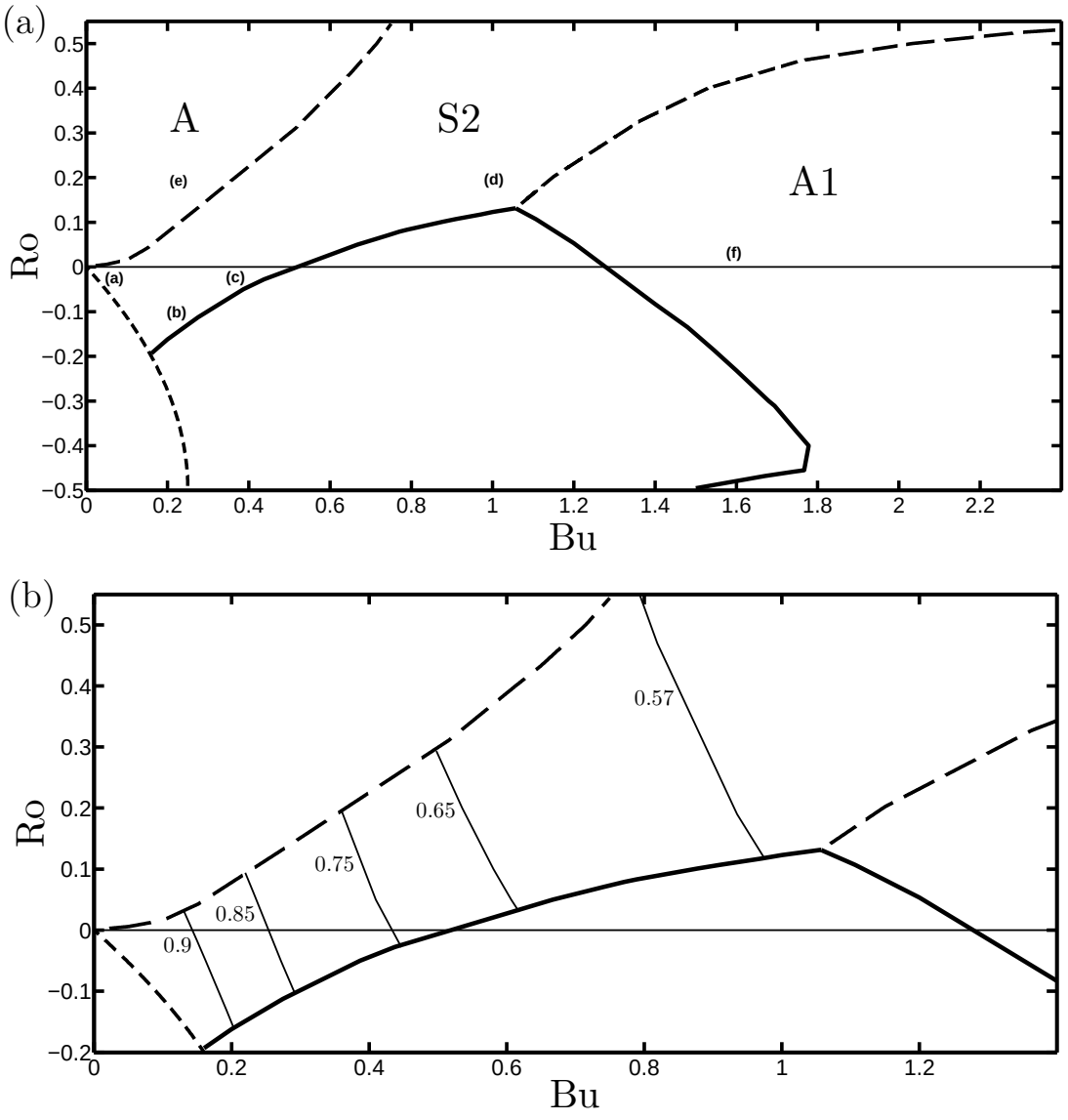

Figure 2.13: Panel (a): Simplification of the parameter map in figure 2.8(a). The fastest-growing eigenmodes in the region labeled A are anti-symmetric in z and have azimuthal wave numbers of 1, 2, 3, or 4; otherwise, the fastest-growing eigenmodes have the symmetry of the large labels. The small labels (a)-(f) indicate the locations in parameter space of the vortices whose fastest-growing eigenmodes are plotted in figure 2.14. Panel (b): Blow up of the S2 region in panel (a). The thin solid curves are the iso-contours of the enstrophy S_{shield} of the vertical vorticity of the eigenmode in the vortex shield. The value of S_{shield} in the S2 region decreases from 0.95 to 0.55 with increasing Bu. The approximate average value of S_{core} in the A and A1 regions are 0.95 and 0.73, respectively. In the lower left corner of panel (a) where $N_c^2 < 0$, $S_{core} \simeq 0.99$.

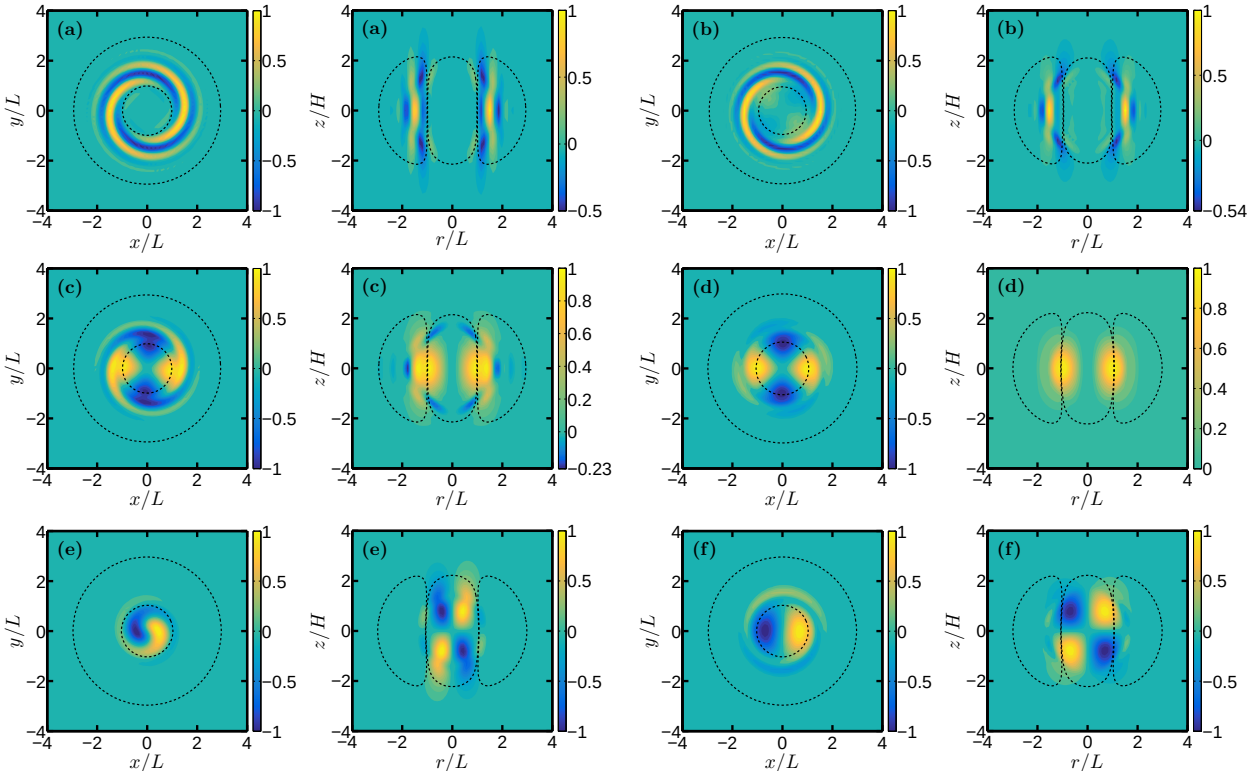

Figure 2.14: (Colour online) Vertical vorticity ω of the eigenmodes of the Gaussian vortices for which the locations in $Ro - Bu$ space are indicated with letters in figure 2.13(a). The vorticity (normalized as in figure 2.12) and boundaries of the shields and cores are plotted as in figure 2.12. The first and third columns of panels show eigenmodes in the x-y plane, and the second and fourth columns show them in the r-z plane. Consistent with figure 2.13, the A and A1 eigenmodes [i.e., (e) and (f)] are mainly confined to the cores of the unperturbed vortices. The S2 eigenmodes with low Bu [i.e., (a) and (b)] are mainly confined to the shield. The S2 eigenmodes with higher Bu [i.e., (c) and (d)] are spread over the core and the shield.

anti-symmetric with respect to the $z = 0$ plane and has $m = 1$ azimuthal wave number (denoted as A1 mode), and the vertical vorticity (ω) of the most unstable modes is mainly confined to the core of the initial (i.e., unperturbed) anticyclone (similar to figure 2.14(f), but for an anticyclone). Preliminarily investigation of the nonlinear evolution of these vortices shows that, in addition to the growth rate, the structure of the most unstable mode is also important in determining how the nonlinearly-equilibrated vortex compares with the initial vortex (nonlinear evolution will be addressed in the second chapter). For $Bu \lesssim 0.5$, the maximum growth rate of anticyclones increases with decreasing Bu or $|Ro|$. In this region, the eigenvector of the most unstable modes is symmetric with respect to the $z = 0$ plane and has $m = 2$ azimuthal wave number (S2 mode). The vertical vorticity of these modes is mainly confined to the shield or spread over the core and the shield of the initial

anticyclone depending on the Burger number (see figures 2.14(a)-(c)). For anticyclones if $Bu < -Ro(1+Ro)$, the interior of the vortex is statically unstable. The growth rates of the most unstable mode for these anticyclones are much larger (by factors up to several thousand or more) compared to those of the anticyclones outside this region (see figures 2.10 and 2.11).

For cyclones, the region of small growth rate ($\sigma < 0.02\,\tau^{-1}$) is much smaller and confined to $Ro < 0.1$ and $0.5 \lesssim Bu \lesssim 1.3$. For $Bu \gtrsim 1$, the maximum growth rate of cyclones increases with increasing Bu or Ro. As was the case for anticyclones with large Bu, in this region the eigenvector of the most unstable modes is (generally) an A1 mode, and the vertical vorticity of these modes is mainly confined to the core of the initial cyclone (see figure 2.14(f)). For $Bu \lesssim 1$, the maximum growth rate of cyclones increases with decreasing Bu or increasing Ro. In this region, for moderate values of Bu, the eigenvector of the most unstable modes is a S2 mode, and its vertical vorticity is spread over the core and the shield of the initial cyclone (see figure 2.14(d)). For smaller values of Bu, the eigenvector is anti-symmetric with respect to the $z = 0$ plane and has $m = 1, 2, 3$ or 4, and its ω is confined to the core of the initial cyclone. Further analysis shows that although the fastest-growing eigenmodes of cyclones are A1 for both small and large values of Bu, the families of these eigenmodes are in fact distinct and have different spatial structures (see figures 2.4–2.7 and 2.14).

The findings described above are compared and contrasted with the relevant published work in §2.4. In particular, in the QG limit, Nguyen et al. [2012] found that the fastest-growing mode changes from S2 to A1 around $Bu = 1$, which along with the general dependence of the growth rate of the most unstable mode on Bu agrees with our results for small Ro. However, there are differences at the limit of small Bu ($\lesssim 0.05$): the QG analysis showed the dominance of modes with higher m, while our analysis using the non-hydrostatic Boussinesq equations shows anticyclones to be statically-unstable with A4 modes dominating, and cyclones to be unstable with A1 modes dominating at low Ro and A2 or A3 modes dominating at moderate Ro. We have also investigated critical layers in the eigenmodes of unstable and neutrally-stable vortices (see §2.3), and have found them at the periphery of the vortex core for a wide range of Bu, in agreement with the QG analysis of Nguyen et al. [2012].

We have also examined how the vortex profile affects the stability properties by comparing our results for the family of vortices with Gaussian pressure anomaly with those of Yim et al. [2016] who studied the linear stability of a family of vortices with Gaussian angular velocity using non-hydrostatic Boussinesq equations. While for $Bu \gtrsim 1$ both families of vortices have most unstable modes with A1 symmetries, for $Bu \lesssim 1$, there are notable similarities and differences: Yim et al. [2016] found that both cyclones and anticyclones can become statically-unstable at low Bu (while we found that only for anticyclones); they found that anticyclones are neutrally stable for moderate Burger numbers $0.5 \lesssim Bu \lesssim 1$ (while we found them weakly unstable) and are unstable with S2 modes dominating for smaller Bu (which is consistent with our results); Yim et al. [2016] found similar stability properties for cyclones as reported here although they found a much larger neutrally-stable region compared to what we found.

Most of the calculations reported in this study have been done for $f/\bar{N} = 0.1$. This

value, which is approximately 10 times larger than the value in ocean at mid-latitudes, was commonly used in studies of vortices in rotating stratified flows because at smaller values the equations of motion are computationally stiff and therefore computationally expensive to compute because small time steps are necessary. Focusing on vortices whose interiors are statically stable (i.e., $N_c^2 \geq 0$), we have repeated some of the calculations with $f/\bar{N} = 0.01$ and found the results to remain quantitatively the same (see Table 2.1 and figure 2.12). We have further shown that the insensitivity of the growth rate and eigenvector of the most unstable modes to $f/\bar{N}$ can be explained from the non-dimensionalized equations of motion. This is because the most unstable eigenmodes are found to be approximately in the hydrostatic balance, which could not be assumed *a priori*. As a result, the dynamics of these modes are nearly independent of $f/\bar{N}$ (as long as this ratio is small, e.g., $\lesssim 0.1$) given that this ratio only appears on the left-hand side of the vertical momentum equation (see §2.5 for details). Note that such insensitivity to $f/\bar{N}$ is not expected in the region where the vortex interior is statically unstable (i.e., $N_c^2 < 0$).

The results of this study improve the understanding of the generic stability properties of 3D vortices in rotating stratified flows, and as discussed in §2.1, extend the analyses of the previous studies in several ways, including: using the full 3D non-hydrostatic Boussinesq equations, which extends the stability analysis well beyond the usually-used QG and shallow-water approximations; focusing on a widely-used model of geophysical and astrophysical vortices, i.e., 3D Gaussian vortices with continuous vorticity and density profiles, which, for many applications, is more appropriate than 2D models, Taylor columns, and/or PV patches that are often used to simplify the numerical or analytical stability analysis; and performing the linear stability analysis on vortices that are exact equilibrium solutions of the full 3D non-hydrostatic Boussinesq equations.

The results also have implications for the two problems that have motivated many studies of vortex stability in the past: the observed stability of long-lived, axisymmetric vortices in the oceans and the observed predominance of anticyclones over cyclones in the oceans (at the mesoscales) and planetary atmospheres (see §2.1 for more details). As described above, while neutrally-stable vortices are found only in a very small region of the $Ro-Bu$ parameter space, the maximum (linear) growth rates in a large region of the parameter space, particularly for anticyclones, are small compared to the vortex turn-around time, which means that these vortices can remain nearly axisymmetric for months and even years despite being linearly unstable. This might explain the observations of long-lived axisymmetric vortices in the oceans, given that the slowly-growing non-axisymmetric flow can be difficult to detect in the satellite or ship-based observations and in time-averaged measurements (but also see the next two paragraphs for several caveats). Furthermore, we found the region of slow growth rates for anticyclones to be much larger than that of the cyclones; whether this offers an explanation for the observed cyclone-anticyclone asymmetry in the oceans (at the mesoscales) and atmospheres requires further studies (see below).

Of course for both problems, the nonlinear stability and nonlinear evolution of these vortices are very important as well, and will be the subject of the next chapter. In particular, we will discuss that small linear growth rate is neither a necessary nor a sufficient condition

for a vortex to survive long to be observed. It is not necessary because our nonlinear simulations show that vortices with eigenmodes with very fast growth rates can have very large Landau coefficients [Drazin & Reid 2004]. Thus, even though the original Gaussian vortex becomes quickly unstable, the instability quickly saturates, and a new equilibrium that looks very similar to the initial unstable Gaussian vortex is established. A slow growth rate of the fastest-growing eigenmode is not sufficient because the equilibrium vortex may be hard to create from realistic initial conditions, or nonlinear instabilities may destroy it.

The limitations and several important caveats of our analysis, discussed in §2.1, should be again emphasized. The exclusion of background shear, compressible effects, and vertical variation of $\bar{N}$ limit the direct application of the results to vortices in the atmospheres and protoplanetary disk, while using an unbounded domain (hence the absence of free surface, bottom topography, lateral boundaries) and vertical variation of $\bar{N}$ limit the direct applicability of the current analysis to most oceanic eddies. The results are most relevant to the stability of interior oceanic vortices such as Meddies. Still, while our results for stability properties and slow growth rates might explain the observations of long-lived nearly axisymmetric Meddies, our results for cyclone-anticyclone asymmetry are not relevant to the dominance of anticyclones among Meddies, which has been suggested to be a result of how Meddies form [McWilliams 1985].

Nonetheless, the results of this study provide a steppingstone to study the more complicated problems of the stability of geophysical and astrophysical vortices, and the framework developed here can be readily extended to include further complexities such as the meridional dependence of f (i.e., the β-effect), compressible effects (e.g., by using the anelastic approximation), and the z-dependence of $\bar{N}$, for example, to account for the thermocline. The framework can be also extended to study the linear and nonlinear stability of vortices in rotating stratified shearing flows such as Jovian vortices, vortices in protoplanetary disks, and oceanic eddies in the Gulf Stream and Antarctic Circumpolar Current. For example, planetary anticyclones on Jupiter appear to have $|Ro| < 0.3$ and $Bu \sim 1$, which gives them a very slow linear growth rate of instability (according to figure 2.8). Understanding how the Jupiter's strong shear influences the growth rate and the most unstable eigenmode is of great interest and can be studied in the modified framework.

Chapter 3

Nonlinear analysis

3.1 Introduction

An inspiring aspect of some of the vortices is their unexplained robustness over time, for conditions that suggest that they should be quickly destroyed. Finite-amplitude perturbations, e.g., interaction with high-amplitude waves, with other vortices, with jets and currents, and topography, or sea surface, or turbulence, are some of the phenomena, that can cause evolution to new equilibria, or even disintegration in time for these vortices [Armi et al. 1989; Olson 1991; Koszalka et al. 2009; Brunner-Suzuki et al. 2012]. Nonetheless, it has been found, via direct observations, that some vortices remain robust for years in the ocean [Lai & Richardson 1977; Armi et al. 1989; Budéus et al. 2004; Chelton et al. 2011]. Different mechanisms (e.g., seasonal recharging by surface forcing, or addition of a supporting circulation with uniform potential vorticity) have been proposed, for the long term sustenance of these vortices [Budéus et al. 2004; Benilov 2005a]. However, our goal here, is to explain the vortex robustness, by not using an external forcing mechanism, but rather one that does so without it, or at least with minimum forcing (i.e., vortices' dynamics, are due to adjustment to the rotation and stratification of the flow they are in). Such an assumption is safely applicable for the vortices that evolve naturally in time.

In the first part of this work, linear stability for 3D axisymmetric vortices in rotating vertically-stratified Boussinesq flows was examined in chapter 2 (for same vortices studied here). The focus of the study was on a widely-used model of geophysical and astrophysical vortices, assuming an axisymmetric Gaussian structure for pressure anomalies in the horizontal and vertical directions. For a range of Rossby number, Ro, and Burger number, Bu (same as in this study), the eigenvalue and the spatial structure of the most unstable eigenmodes (i.e., the fastest-growing ones) were calculated numerically, as a function of $Ro - Bu$. It was shown that, only a small region of the parameter space was neutrally stable, with the growth rate of all of the eigenmodes equal to zero. However, it was also found that anticyclones generally have a smaller growth rate σ, compared to the cyclones. Specifically, the most unstable eigenmode of the anticyclones has, over a significant portion of the parameter

map (e.g., $Ro < 0$ and $Bu \lesssim 0.5$), growth rates slower than 50 turnaround times of the vortex (which can for example correspond to 2 to 3 years for oceanic eddies). For cyclones, a region of slow growth rate was found as well, but for a small region $0 < Ro < 0.1$ and $0.5 \lesssim Bu \lesssim 1.3$. Also note that, while most of the calculations in this study where done for $f/\bar{N} = 0.1$ (where f and $\bar{N}$ are the Coriolis and background Brunt-Väisälä frequencies), we have verified and explained, the insensitivity of the stability results in chapter 2 to reducing $f/\bar{N}$ to the more ocean-relevant value of 0.01.

In this study we examine the finite-amplitude stability of 3D vortices in rotating stratified flows and discuss the evolution of the unstable vortices for various perturbations, as functions of Rossby number Ro (for $-0.5 < Ro < 0.5$) and Burger number Bu (for $0.07 < Bu < 2$). We study the finite-amplitude stability by examining points in the region of $Ro - Bu$ parameter space in which the vortices have at least one unstable eigenmode with a growth rate that is faster than 50 turnaround times (see chapter 2, §2.4). Although the Boussinesq equations that are solved here are undamped, we use sponge layers as the boundary conditions for the domain of the solution. The sponge layer which is modeled as Rayleigh drag, and Newton cooling, acts on the weak filaments shed from the vortices and inertia-gravity waves (boundary damping only damps kinetic energy, but it can damp or increase potential energy) that are radiated to the periphery of the domain. This allows the vortices to evolve towards the final equilibria gradually. Shedding of filaments during vortex evolution has been observed extensively before [Dritschel & De La Torre JuáRez 1996; Humphreys & Marcus 2007], and radiation of inertia-gravity waves has been observed before in the laboratory [Aubert et al. 2012] and numerical calculations [Hassanzadeh et al. 2012]. Our calculations show that most of the vortices do *not* deviate much, from their initial unperturbed equilibria, and regardless of the perturbations, vortices always evolve to well-defined basins of attraction. The unexpected robustness of the equilibria and the small sizes of the attracting basins are explained using the numerical results, as well as a simplified representation of the flow and an analytical solution for the evolution (i.e., the Landau equation). Note that, our explanation of the robustness of baroclinic vortices does not require a direct forcing mechanism (e.g., vortex merger, or interaction with shear flow). The dynamics of the vortices is expected to dependent only weakly on $f/\bar{N}$, for $f/\bar{N} \leq 0.1$, which is the range relevant to oceanic flows. Therefore, we leave the study on the effects of $f/\bar{N}$ on the long-term stability of the vortices to a future work.

The remainder of the chapter is structured as follows. The equations of motion, numerical method, Gaussian vortex model, finite-amplitude perturbations, vortex evolution enstrophy measures, and the method to identify dominant symmetries are discussed in §3.2. The results of the finite-amplitude stability analysis, along with the attracting basins, different vortex groups, and parameter map of stability are presented in §3.3. The simplified flow representation for the vortex groups, and also the Landau equation are discussed in §3.4. Discussion and summary for this work are in §3.5.

3.2 Problem formulation

Equations of motion

We solve the non-hydrostatic Boussinesq equations, in a constant angular velocity rotating frame, on the f-plane, with a background density stratification $\bar{\rho}(z)$ varying linearly in z (here an overbar is used for the background flow, which lets us denote the imposed flow far from the vortex). To simplify the equations, we define the buoyancy as $b \equiv (-g)(\rho/\rho_o)$, which when used in the equations, it simply removes acceleration of the gravity $-g$ (here the density ρ_o is $\rho(z=0)$). Our idealized simulations, thus exclude some of oceanic and atmospheric phenomena, e.g. Rossby waves, β-effects, external shear, topographic elements, and free-surface effects, which lets us exclusively study the evolution in each simulation.

The governing equations of motion (with negligible viscosity and diffusion), in Cartesian coordinates, with x and y horizontal directions, and z denoting the vertical direction, and as observed in a frame rotating with an angular frequency $f/2$, are

$$\begin{aligned} \boldsymbol{\nabla \cdot v} &= 0, \\ \mathrm{D}\boldsymbol{v}/\mathrm{D}t &= -\nabla p/\rho_o + \boldsymbol{v} \times f\hat{\boldsymbol{z}} + b\,\hat{\boldsymbol{z}}, \\ \mathrm{D}b/\mathrm{D}t &= -\bar{N}^2 v_z, \end{aligned} \tag{3.1}$$

where $\boldsymbol{v} = (v_x, v_y, v_z)$ is the 3D velocity vector, $\mathrm{D}/\mathrm{D}t \equiv \partial/\partial t + \boldsymbol{v}\cdot\boldsymbol{\nabla}$ is the material derivative, and $\hat{\boldsymbol{z}}$ is the unit vector in the vertical direction. The Coriolis frequency is f (constant in this study). Here the pressure anomaly and the density anomaly are $p(\boldsymbol{x},t) = p_{tot}(\boldsymbol{x},t) - \bar{p}(z)$ and $\rho(\boldsymbol{x},t) = \rho_{tot}(\boldsymbol{x},t) - \bar{\rho}(z)$, where p_{tot} and ρ_{tot} are the values of the total pressure and total density, respectively. $\bar{N} \equiv \sqrt{-(g/\rho_o)(d\bar{\rho}/dz)}$ is the Brunt-Väisälä frequency of the background flow (constant here). The background pressure $\bar{p}$ and density $\bar{\rho}$ are in hydrostatic balance $d\bar{p}/dz = -\bar{\rho}g$. The Rayleigh drag, and Newtonian cooling (at large radial and vertical distances) act on the momentum and density, respectively. The details about these terms are given in the next section.

Numerical method

A pseudo-spectral initial-value code is used to solve (3.1), on a triply-periodic domain with 256 Fourier modes in each direction. The rotating stratified flows in (3.1) allow propagation of the inertia-gravity waves. Here we use a semi-analytic method, which lets us track, and resolve these waves, accurately and efficiently. Details of the numerical method here and of Barranco & Marcus [2006] are the same.

The vortices in this study gradually evolve towards their attraction basins. To ensure that the domain boundaries do not alter the evolution significantly, the computational domain size is chosen to be large compared to the vortex size, before, during, and after the evolution of the vortex (for the cases with splitting, the simulations are carried out to the time resulting tripoles move well within the boundary damping region). The domain size in the x and y

directions, i.e., the values of L_x and L_y are 15 times larger than the initial vortex diameter ($2L$), and, similarly, the domain size in the z direction L_z is 15 times larger than the initial vortex height ($2H$). Our investigation of the vortex evolution, and about the late-time fate of the vortices, assumes that there is a basin of attraction to which unstable vortices evolve. Generally, non-dissipative equations, such as the inviscid Boussinesq equations[1] that we solve here with an initial value code do not allow attractors. However note that our calculations have sponge layers as the boundary conditions that may absorb kinetic or potential energy. They are located far from the location of the initial vortex and far from most of the vortices spawned from the initial vortex. The direct effects of the boundary-vortex interactions are initially small. In fact, due to the initial vortices being "shielded" (that is, the circulation in the total flow at each height is equal to zero. See §2.2 of chapter 2), the long-range velocity of an initially-compact vortex falls off as $1/r^2$, where r is the radial distance (i.e., $r = (x^2+y^2)^{1/2}$). The sponge layer, implemented as Rayleigh drag and Newtonian cooling in (3.1), damps $\boldsymbol{v}$ and ρ outside a cylindrical surface of diameter $24L$ and height $24H$ around the center of the domain. The vortices shed filaments of vorticity and/or density, when they are not steady. These filaments carry significant energy and momentum to distances far from the vortex and are absorbed by the sponge layer. Similarly, the vortices in an ambient-stratified fluid radiate inertia-gravity waves in their evolutions, which can also carry momentum and energy to the domain boundaries, and are damped by the boundary damping. Thus, although the Boussinesq equations that we solve here are undamped, filament shedding, and/or wave emission, along with the energy absorption at the sponge layer allow the vortices to evolve into their final equilibria (see Appendix B). By following the evolution of the vortices with an initial-value code for several hundred turnaround times, we find that vortices remain unchanged, after reaching their basins of attraction, also for hundreds of turnaround times (see below for the vortex turnaround time definition).

Hyperviscosities and hyperdiffusivities, that are added to our calculations here, are used to stabilize the code. See Barranco & Marcus [2006] for more details.

Gaussian vortices, finite-amplitude perturbations, and evolution enstrophy measures

Here, the equilibria are 3D axisymmetric baroclinic vortices that are initially in horizontal cyclo-geostrophic balance and vertical hydrostatic balance, and hence they are in gradient-wind balance. The initial vortex is centered, and is shown to remain centered, at $r = 0$, and $z = 0$, for all cases studied here (except when vortices split). In the first part of this work, we explored the linear stability and linear growth rates of Gaussian vortices as functions of Ro

[1] We have dissipation in our system, in hyperviscosity and hyperdiffusivity form, to stabilize our code. Hyperdiffusivity can both add and remove potential energy from the flow, while hyperviscosity only removes kinetic energy from the high wave numbers of the velocity field. However, we argued previously in chapter 2 and will also show here the fact that our results are not largely affected by the hyperdissipation. The real use of the hyperviscosity here is that it allows vortex lines to connect and reconnect, which is not possible in a viscous-free calculation.

and Bu, the results of which, will be useful for this study. Here, we will again examine the stability of Gaussian vortices (a representation of which is shown by the equations (2.2)-(2.4) in chapter 2, §2.2), but our investigation will be confined to finite-amplitude perturbation and evolution of the vortices that have σ (i.e., where σ is the linear growth rate of the vortex's fastest growing eigenmode) larger than 0.02 inverse vortex turnaround times (the vortex turnaround time is defined below). To simulate the evolution of these vortices, the flow is initialized by adding perturbations that can differ from each other, not only by the type, but by the perturbation amplitude as well. This allows us to replicate different perturbations efficiently. Additionally, to make sure that perturbation type or amplitude do not have a significant effect on our calculations, two or more different simulations are carried out for each vortex whose evolution is studied. However, it should also be noted that, as shown in the next section, for the vortices with locally unstable density gradient at the vortex center, denoted as statically unstable, the most-unstable eigenmode always has the same spatial symmetry, and σ that is significantly larger than the σ of the other eigenmode symmetry classes, and is therefore the only eigenmode class used as the perturbation for these vortices. Also, our study's perturbations are implemented from the following specific groups: (a) One (or more) of the fastest growing eigenmodes in the six previously-identified symmetry classes (in accord with the constraints presented in chapter 2, §2.2), (b) white noise, implemented as divergence-free noise in the flow velocity, or (c) a combination of an eigenmode and white noise. For these perturbations, we define the initial perturbation amplitude, as $A_{IC,i} \equiv \int |\boldsymbol{v}_i'|^2 d^3x \,/\, \int |\tilde{\boldsymbol{v}}|^2 d^3x$, where $\boldsymbol{v}_i'$ demonstrates the velocity of the i^{th} perturbation, and $\tilde{\boldsymbol{v}}$ denotes the velocity of the unperturbed equilibrium (from here onwards, a tilde is used to represent the initial unperturbed equilibrium). The integrals in the equation are calculated over the entire computational domain. Note that because relevant observations of the ocean and atmosphere vortices are nearly axisymmetric, values of the initial amplitudes in our simulations are chosen small (such that $A_{IC,i} \lesssim 10^{-2}$). In what follows, any quantity denoted with a subscript E is calculated at the point of maximum absolute vertical vorticity value. To track the vortex quantitatively, we define for its horizontal extent and angular velocity, the horizontal length scale $L \equiv \sqrt{|4p_E/(\nabla_h^2 p)_E|}$ (i.e., L is the vortex radius), and the Rossby number $Ro \equiv \omega_E/2f$ (i.e., ω is the vertical vorticity), respectively. Also, the subscript h means horizontal component. For Gaussian vortices here $\tilde{\omega}_E = \tilde{\omega}_c$ (where c denotes the vortex center). If $\sigma = 0$, a simulation initialized with an axisymmetric 3D vortex in dissipationless equilibrium and a Gaussian p (as described above) remains similar to the initial equilibrium, e.g., its $N_c \neq \bar{N}$ remains the same ($N \equiv \sqrt{-(g/\rho_o)(d\rho/dz)}$ is the Brunt-Väisälä frequency). Furthermore, it was shown before that the σ of the vortex in a region of the parameter space was $\lesssim 50$ inverse turnaround times (i.e. often corresponding to several years for ocean eddies). For more details about that study see chapter 2. Here, we examine the evolution of the vortices with σ larger than 50 turnaround times, towards their attracting basins (the vortex turnaround time is defined as $\tau \equiv 4\pi/\tilde{\omega}_c$). Note that the

initial Gaussian vortex has an aspect ratio of

$$\left(\frac{H}{L}\right)^2 = \frac{-Ro(1+Ro)}{\bar{N}^2[1-(N_c/\bar{N})^2]}, \tag{3.2}$$

(we have not used tildes in (3.2) for simplicity) in accord with the universal scaling law of Hassanzadeh et al. [2012] and Aubert et al. [2012]. Also, our definition of $H \equiv \sqrt{|2p_E/(\partial^2 p/\partial z^2)_E|}$, is the same as in Hassanzadeh et al. [2012] and Marcus & Hassanzadeh [2014], where the vortex's mid-plane is the horizontal plane $z = 0$, and H is its pressure anomaly's vertical length scale (i.e., its half-hight from the $z = 0$) calculated using the second order z derivative. The Burger number is defined as

$$Bu \equiv \left(\frac{\bar{N}}{f}\frac{H}{L}\right)^2. \tag{3.3}$$

We have a non-standard way of measuring the volume of the basin of attraction of our perturbed equilibrium Gaussian vortices. Our initial-value experiments begin with an exact equilibrium Gaussian vortex, that is perturbed with several kinds of initial perturbations that give the initial conditions different initial energies and momenta. The flow then evolves, shedding internal gravity waves to our dissipative boundary conditions. Therefore, we would not expect all of the initial conditions to relax to the same final state. Rather our cloud of initial conditions relax to a cloud of final states. This cloud of final states represents a basin of attraction. For N sets of perturbations, the vortices evolve to the equilibria ω_1, ω_2, ..., and ω_N, where the equilibrium is represented for each case j by using its vertical vorticity ω_j. The individual final equilibria are each located and oriented differently. To compare final equilibria to each other and their average, we account for each case's translations and rotations, using a coordinate system, with an origin E, and an x axis pointing in the direction of minimum vertical vorticity (i.e., for the cyclones). Also, the z axis is always oriented in the vertical direction. Below we will often use the vertical vorticity ω to refer to the equilibria in this study. We define the average final equilibrium

$$\hat{\omega}(x,y,z) \equiv \left(\frac{1}{N}\right)\sum_{j=1}^{N}\langle\omega_j(x,y,z,t)\rangle, \tag{3.4}$$

where the angle brackets $\langle\ \rangle$ show the time average after reaching quasi-steady state, i.e., time during which fractional changes – fluctuation amplitude over mean, of the kinetic energy $KE/\widetilde{KE}$, the enstrophy $EN/\widetilde{EN}$, the horizontal length scale $L/\widetilde{L}$, the vertical length scale $H/\widetilde{H}$, Rossby number Ro, and Burger number Bu values become $\lesssim 0.1$. Enstrophy is defined as $EN \equiv \int \omega^2 d^3x$, where the integral is over the entire computational domain. In the following, we use a hat to show the average final equilibrium's properties. The size of the attracting basin depends on the difference between individual final equilibria, and the average final equilibrium $\hat{\omega}$, and is calculated numerically for each simulation, by defining

the quantity

$$d_j \equiv \frac{\int (\langle \omega_j \rangle - \hat{\omega})^2 d^3x}{\int \hat{\omega}^2 d^3x}, \tag{3.5}$$

where the numerator and denominator integrals are calculated over the computational domain. Also, the changes in Ro,

$$\delta Ro_j \equiv |Ro_j - \widehat{Ro}|, \tag{3.6}$$

indicate the magnitude difference between Ro_j for the time-averaged final equilibrium $\langle \omega_j \rangle$ and $\widehat{Ro}$ for the average equilibrium $\hat{\omega}$. The δBu_j definition,

$$\delta Bu_j \equiv |Bu_j - \widehat{Bu}|, \tag{3.7}$$

for the Burger number is analogous. We note that, generally, for vortices with basins of attraction, the final equilibrium can be similar to the initial vortex (that has large growth rates), or different from it. More accurately, we calculate the differences inside the initial vortex's shield D_s, as well as inside its core D_c, by defining the quantities

$$D_s \equiv \frac{\int_{shield} (\hat{\omega} - \tilde{\omega})^2 d^3x}{\int_{shield} \tilde{\omega}^2 d^3x}, \tag{3.8}$$

$$D_c \equiv \frac{\int_{core} (\hat{\omega} - \tilde{\omega})^2 d^3x}{\int_{core} \tilde{\omega}^2 d^3x}, \tag{3.9}$$

where the integrals in equations (3.8) and (3.9) are calculated inside the shield and core, respectively, of the initial equilibrium vortex. Also, the changes in Ro,

$$\Delta Ro \equiv |\widehat{Ro} - \widetilde{Ro}|, \tag{3.10}$$

indicate the magnitude difference between $\widehat{Ro}$ for the average final equilibrium $\hat{\omega}$ and $\widetilde{Ro}$ for the initial unperturbed equilibrium $\tilde{\omega}$. Furthermore, the ΔBu definition

$$\Delta Bu \equiv |\widehat{Bu} - \widetilde{Bu}|, \tag{3.11}$$

for the Burger number is analogously implemented. The equilibria in this study are generally, Gaussian, Gaussian-like, or non-Gaussian-like. A Gaussian equilibrium is one, with a prefect Gaussian pressure distribution, in horizontal cyclo-geostrophic balance and vertical hydrostatic balance. The unperturbed initial equilibria here all are Gaussian. In the following, for a cyclonic equilibrium vortex the core of the cyclone is a contiguous region at and near the vortex center where the ω is greater than zero or zero. The shield is a contiguous region $\omega < 0$, surrounding the core (usually looking like a shell or annular ring) located not too far from the core. We will show quantitatively in §3.3 and below that the core of all vortices in this study remain close to a Gaussian state (except for a case for which the vortex

splits). For Gaussian-like final equilibria the core and shield remain close to Gaussian, but they are not perfectly Gaussian. Therefore, the cases with $D_c \lesssim 0.1$ and $D_s \lesssim 0.4$, i.e., with the final equilibrium's core and shield near initial Gaussian vortex's core and shield, have a Gaussian-like final equilibrium. Our choice of 0.4 for D_s's upper limit is large, because we find that there are some cases for which part of the shield deforms or breaks, while a large part of it remains close to the Gaussian vortex's shield. We describe this family of final equilibria as Gaussian-like as well. For the cases with $D_c \gtrsim 0.1$, i.e., for the vortices with the final equilibrium's core far from the initial Gaussian vortex's core, we define the quantities

$$F_s \equiv \frac{\int_{shield}(\hat{\omega} - \tilde{\omega}^{NEW})^2 d^3x}{\int_{shield}(\tilde{\omega}^{NEW})^2 d^3x}, \tag{3.12}$$

$$F_c \equiv \frac{\int_{core}(\hat{\omega} - \tilde{\omega}^{NEW})^2 d^3x}{\int_{core}(\tilde{\omega}^{NEW})^2 d^3x}, \tag{3.13}$$

where $\tilde{\omega}^{NEW}(x, y, z)$ is the value of the Gaussian vortex's vertical vorticity, demonstrated for $Ro = \widehat{Ro}$ and $Bu = \widehat{Bu}$, and the integrals in equations (3.12) and (3.13) are calculated inside the shield and core, respectively, of $\tilde{\omega}^{NEW}(x, y, z)$. The cases with $F_c \lesssim 0.1$ and $F_s \lesssim 0.4$, i.e., with the final equilibrium's core and shield near $\tilde{\omega}^{NEW}(x, y, z)$'s core and shield, have a Gaussian-like final equilibrium. For the cases, other than the ones listed above for Gaussian and Gaussian-like final equilibria, the final equilibrium is non-Gaussian-like. Furthermore, for the vortices with Gaussian-like and non-Gaussian-like final equilibria the "shield" in some cases breaks into two (or more) satellite vortices that look different from the initial shield. For such cases, the satellite vortices are the two, or four (or even six) regions rotating around the core of the vortex, where the satellites' vorticity is the opposite of that of the vortex's core. The precise definitions that we use for *core*, *shield*, and *satellites* are in Appendix A. During the shield breaking, filaments are shed, which then carry energy and momentum, far from the vortex, where their effects are exhausted by the sponge layer. The boundary damping mechanism is particularly through the potential energy damping (as shown in Appendix B), i.e, it removes the density anomalies by damping their potential energy magnitude. Surprisingly, in this study all but one of the vortices have basins of attraction (see §3.3), for which the sizes of the basins are shown to be small. For the final equilibria in such cases we find that the amplitude of the vorticity decays exponentially outside the shield (or away from the satellites) of the vortices with the radial distance r. This is because the vortices are confined to the region near their cores and due to the boundary damping acting at large radii. For the cases with splitting, the resulting tripoles quickly move to large radii, near the boundary damping region. As such, the simulations for these cases are comparatively short. In fact, the simulations are only carried out until the direct interaction of the vortices and the boundary damping becomes significant. There is one case with splitting in this study, i.e., last eight rows of table 3.4 (that is for a vortex which can split).

There are three dimensionless parameters that describe the Gaussian vortices' dynamics (e.g., see §2.2 of chapter 2). For vortices that remain Gaussian-like, again we use three parameters for tracking vortices during evolution. To adequately and consistently describe

the vortex dynamics, in this study we use, as tracking parameters, Ro, $f/\bar{N}$ and Bu. The differences between the unperturbed vortex's shield and the final equilibrium's broken shield and/or satellite vortices are calculated numerically, as described above (D_s and F_s). Also, note that for the vortices with a non-Gaussian-like final equilibrium, where the vortex breaks into multiple smaller vortices, or splits into two separate parts, additional parameters are required to describe the vortex characteristics (e.g., the distance between smaller vortices, or the radial velocity of a tripole). Here we again use the same parameters and measures as described above for vortices with a non-Gaussian-like final equilibrium. An analysis, carried out for these cases with the additional parameters is forwarded to a future study.

To find out the possible form of time dependence (or independence) of the perturbations throughout the vortex quasi-steady state (the quasi-steady state for vortices was defined above), we define the quantity

$$EN'_{\infty,j}(t > t_\infty) \equiv \frac{\int (\omega_j - \langle \omega_j \rangle)^2 d^3x}{\int \langle \omega_j \rangle^2 d^3x}, \tag{3.14}$$

where t_∞ denotes the time at which ω_j reaches quasi-steady, and the integral is calculated over the entire computational domain. The perturbations are approximately-steady, if $EN'_{\infty,j}(t)$'s temporal changes are less than 0.1, and are unsteady (and therefore can be periodic, or aperiodic), if $EN'_{\infty,j}(t)$'s temporal changes are $\gtrsim 0.1$. In this study we find, by examining the late-time perturbations, that for the cases with an attracting basin, $EN'_{\infty,j}$ has approximately-steady values.

Dominant Symmetries

The differences between the initial and final equilibria for the vortices evolving towards an attracting basin can be dominated by a symmetry. The difference flows that belong to a dominant symmetry class, are either largely symmetric or anti-symmetric with respect to the horizontal plane $z = 0$ and have a dominant m-fold azimuthal symmetry about the z-axis (and therefore, for such flows, the other components of the difference flow, i.e., with symmetries other than the dominant difference flow symmetry are much smaller). Here, we use the labels Sm (or Am) for each flow component, to identify it as Symmetric (or Anti-symmetric) with respect to the $z = 0$ horizontal plane and with m-fold symmetry.

The flow evolution from its axisymmetric Gaussian equilibrium can be described as

$$\boldsymbol{g}(\boldsymbol{x}, t) = \tilde{\boldsymbol{g}}(r, z) + \boldsymbol{R}(\boldsymbol{x}, t), \tag{3.15}$$

where the flow has 3 velocity components, a density component, and a pressure component $\boldsymbol{g} \equiv [v_r, v_\phi, v_z, \rho, p]$, and we use $\boldsymbol{R}(\boldsymbol{x}, t)$ to denote the remainder. The remainder can be exactly decomposed into a symmetric part $\boldsymbol{R}_{\rm S}$, and an anti-symmetric part $\boldsymbol{R}_{\rm A}$, about the horizontal plane $z = 0$. For the symmetric or anti-symmetric remainders, the (dimensionless)

enstrophies are then defined as

$$\gamma_{\mathrm{S}} \equiv \frac{\int |\omega_{R,\mathrm{S}}|^2 dx^3}{\int |\omega_R|^2 dx^3}, \tag{3.16}$$

$$\gamma_{\mathrm{A}} \equiv \frac{\int |\omega_{R,\mathrm{A}}|^2 dx^3}{\int |\omega_R|^2 dx^3}, \tag{3.17}$$

where ω_R shows the remainder vertical vorticity of the j^{th} time-averaged final equilibrium, or the average final equilibrium, the additional subscripts S and A are used to represent symmetric and anti-symmetric parts, the numerator and denominator integrals are calculated over the entire computational domain, and it can be shown that $\gamma_{\mathrm{S}} + \gamma_{\mathrm{A}} = 1$. If $1 - \gamma_{\mathrm{S}} \ll 1$, or $1 - \gamma_{\mathrm{A}} \ll 1$, then the difference flow possibly has a dominant symmetry. Otherwise, the analysis here demonstrates that the remainder simply has no dominant symmetries (γ_{S}, γ_{A} $\sim O(0.1)$). However, if the difference flow is found S or A dominant about $z = 0$ then, the dominant symmetry remainder shown by a subscript $\perp$ (i.e., $\boldsymbol{R}_\perp = \boldsymbol{R}_{\mathrm{S}}$ for a largely symmetric $\boldsymbol{R}$, or $\boldsymbol{R}_\perp = \boldsymbol{R}_{\mathrm{A}}$ for a largely anti-symmetric $\boldsymbol{R}$) is again exactly decomposable into (see Appendix D) a $\boldsymbol{R}_{\perp even}$ part with the azimuthal wave numbers that are even, and a $\boldsymbol{R}_{\perp odd}$ part with the azimuthal wave numbers that are odd. For these remainders, the (dimensionless) enstrophies are defined as

$$\gamma_{\perp even} \equiv \frac{\int |\omega_{\perp even}|^2 dx^3}{\int |\omega_\perp|^2 dx^3}, \tag{3.18}$$

$$\gamma_{\perp odd} \equiv \frac{\int |\omega_{\perp odd}|^2 dx^3}{\int |\omega_\perp|^2 dx^3}, \tag{3.19}$$

similar to the ratios given by (3.16) and (3.17), but where $\omega_\perp$ shows the $\boldsymbol{R}_\perp$ vertical vorticity of the j^{th} time-averaged final equilibrium, or the average final equilibrium, the additional subscripts 'even' and 'odd' are used to represent even and odd parts, and it can be shown that $\gamma_{\perp even} + \gamma_{\perp odd} = 1$. If $1 - \gamma_{\perp even} \ll 1$, or $1 - \gamma_{\perp odd} \ll 1$, then the difference flow is shown to have $\perp$ dominant symmetry about $z = 0$, and even or odd dominant symmetry azimuthally. Otherwise, the analysis here demonstrates that the remainder simply has no dominant symmetries ($\gamma_{\perp even}$, $\gamma_{\perp odd} \sim O(0.1)$) (note as well that for a remainder part that is not dominant, the even and odd enstrophies can be calculated to determine more exactly how these enstrophies are allocated). For a difference flow dominated by $\perp$ symmetry about $z = 0$, and by an even symmetry azimuthally, the $\boldsymbol{R}_{\perp even}$ is further decomposable into (again see Appendix D) a $\boldsymbol{R}_{\perp even,d4}$ part with the azimuthal wave numbers that are even and divisible-by-4, and a $\boldsymbol{R}_{\perp even,nd4}$ part with the azimuthal wave numbers that are even not divisible-by-4. For these remainders, the (dimensionless) enstrophies $\gamma_{\perp even,d4}$ and $\gamma_{\perp even,nd4}$ are defined in a way, similar to (3.16) and (3.17), but with $|\omega_{\perp even,d4}|^2$ and $|\omega_{\perp even,nd4}|^2$ as the numerator integrands, $|\omega_{\perp even}|^2$ as the denominator integrand, and where $\gamma_{\perp even,d4} + \gamma_{\perp even,nd4} = 1$. If $1 - \gamma_{\perp even,d4} \ll 1$, or $1 - \gamma_{\perp even,nd4} \ll 1$, then the difference flow is shown to have $\perp$ dominant symmetry about $z = 0$, and even and divisible-by-4; or even not divisible-by-4 dominant

symmetry azimuthally. Otherwise, the analysis here demonstrates that the remainder simply has no dominant symmetries ($\gamma_{\perp even,d4}$, $\gamma_{\perp even,nd4} \sim O(0.1)$) (note as well that for an even remainder part that is not dominant, the even and divisible-by-4; and even not divisible-by-4 enstrophies can be calculated to determine more exactly how these enstrophies are allocated). Performing the stepped analysis above for any symmetry class *symm* specifically, the fraction of the total remainder enstrophy pertaining to that symmetry class Γ_{symm} can be accurately found. The Γ_{symm} is defined as

$$\Gamma_{symm} \equiv \frac{\int |\omega_{symm}|^2 dx^3}{\int |\omega_R|^2 dx^3}, \tag{3.20}$$

where ω_{symm} is the vertical vorticity of the symmetry class *symm*. No dominant symmetries exist for the cases that have $\Gamma_{symm} \sim O(0.1)$ (for any *symm*).

Note that although the study here is on the finite-amplitude stability of axisymmetric (or usually almost axisymmetric) vortices, in fact we use (3.1) in the Cartesian coordinates, rather than in the cylindrical coordinates. A solution carried out in the Cartesian coordinates avoids the difficulties of e.g., division by declining r at the origin ($r = 0$). In the analysis above, the enstrophies calculations are done for the remainder parts that are symmetric or anti-symmetric in the vertical direction, while in the azimuthal direction there is one of the following classes of symmetry: m odd; m even not divisible-by-4; and m even and divisible-by-4. As used here, these specific symmetry groups can be directly sought for in Cartesian coordinates and in fact also avoid introducing additional errors due to transformation between Cartesian and cylindrical coordinates (see Appendix D).

3.3 Evolution of the vortices and finite-amplitude stability

Here, we examine the evolution for selected vortices with very fast growth rates (i.e., with growth rates $\sigma > 0.02\,\tau^{-1}$) towards each case's final equilibrium. Also, we demonstrate how the cloud of initial states for the cases examined, evolves to the cloud of final states in the $Ro-Bu$ parameter space. For all cases here we use fixed $f/\bar{N} = 0.1$, and effects of changing $f/\bar{N}$ on the dynamics of the vortices is therefore forwarded to a future study. Also, it is noted that a vortex perturbed using different perturbations can evolve to different final equilibria. Our initial-value calculations however show that there are basins of attraction with small sizes (as demonstrated quantitatively below) to which the vortex cloud can be attracted, such that in these cases, the final equilibria are independent of the initial perturbations that are implemented in our code. Furthermore, we show that the flow is represented throughout its complete evolution using a simple equation including the unperturbed equilibrium, its dominant symmetry eigenmode, and a complex valued coefficient, where the latter can be calculated analytically using the Landau equation.

We also calculate the difference between the final and the initial states of the vortices in their cores and shields, as well as the values of the dimensionless enstrophies of the difference

flow for the class of symmetry that is dominant, and also for those that are not dominant (see §3.2). Then we show that there are six different groups of final equilibria, each of which has different properties for their final equilibria, and a different class of dominant symmetry (there also are groups of vortices with no dominant symmetries). It also is shown that there are a few cases with the vortex splitting into two tripoles moving radially away, which clearly have no attracting basins and no dominant symmetries.

Attracting basins, dominant symmetries and the vortex groups

Our initial-value calculations show that vortices generally evolve towards one of the attracting basins within six different groups, where the difference between final and initial states of the vortices have different core and shield (or satellite) configurations, and/or dominant symmetries of the difference flow. The six vortex groups and their characteristics are described as follows:

Group 1

The qualitative distinction of these vortices is that they have quasi-steady final equilibria, that are visually indistinguishable from the corresponding initial equilibria to which we add the finite-amplitude perturbations. This observation can be made quantitative, by our initial-value calculations for group 1 cases listed in table 3.1. The numerical values of d_j are $O(10^{-4})$ or smaller, indicating that, there is a well-defined basin of attraction that these vortices evolve to. Furthermore we show that D_c and D_s values are $O(10^{-2})$ or smaller in all the cases, so group 1's final equilibria remain similar to their initial equilibria (i.e., in the L2 norm terms). Also, under table 3.1's 'Differences (Ro and Bu)', group 1's Rossby number changes δRo_j (that are $O(10^{-3})$ or smaller) and Burger number changes δBu_j (that are $O(10^{-2})$ or smaller), more clearly show the small basin sizes for the final equilibria of group 1; and the Rossby number changes ΔRo (that are $O(10^{-2})$ or smaller) and Burger number changes ΔBu (that are $O(10^{-2})$ or smaller), more clearly show the resemblance between group 1's final and initial equilibria. Furthermore, the remainder flow has an A1 dominant symmetry for group 1's final equilibria, as indicated by the values of $\Gamma_{A1} \gtrsim 0.9$ shown in table 3.6 (and with the contributions of $\Gamma_{S2} \simeq 0.03$ and $\Gamma_{S4} \simeq 0.03$ shown to be much smaller). The kinetic energy $KE/\widetilde{KE}$, enstrophy $EN/\widetilde{EN}$, horizontal length scale $L/\widetilde{L}$, vertical length scale $H/\widetilde{H}$, Rossby number Ro, and Burger number Bu for different perturbations of a group 1 vortex are demonstrated in figure 3.1, showing how the vortex reaches quasi-steady state. Example group 1 vortices are illustrated in figures 3.2 and 3.3. The former shows the Gaussian and average final equilibria as well as the details of the vortex evolution, whereas the latter only shows the Gaussian and average final equilibria.

Group 2

Qualitatively, all group 2 vortices evolve towards quasi-steady final states, with their core in the initial vortex state looking very similar to their final slightly-deformed cores, and with

Init. Eq.		**Perturbations**				$\boldsymbol{\sigma(\tau^{-1})}$	**Differences (L2 norms)**			**Differences (*Ro* and *Bu*)**			
$\widetilde{Ro}$	$\widetilde{Bu}$	P1	$\log_{10}[A_{IC,P1}]$	P2	$\log_{10}[A_{IC,P2}]$		$d_j(10^{-5})$	$D_c(10^{-3})$	$D_s(10^{-3})$	$\delta Ro_j(10^{-5})$	$\delta Bu_j(10^{-4})$	$\Delta Ro(10^{-4})$	$\Delta Bu(10^{-3})$
+0.5	1.6	A1	−2	N	−2.5		53	13	16	440	96	170	78
		S2	−2	N	−2.5	0.17							
+0.5	2.0	A1	−2	N	−2.5		73	18	18	950	210	320	99
		S2	−2	N	−2.5	0.16							
+0.4	1.4	A1	−4	-	-		16			150	37		
		A1	−4	N	−4.5		18			120	52		
		A1	−2	N	−2.5		24	8.9	13	200	56	60	51
		S2	−4	N	−4.5	0.13	21			140	46		
		S2	−2	N	−2.5		26			210	79		
+0.2	1.0	A1	−2	N	−2.5		15	3.1	9.6	19	7.7	7.1	5.2
		S2	−2	N	−2.5	0.058							
+0.2	1.3	**A1**	−2	-	-	0.062	20			31	16		
		A1	−2	N	−2.5		12	5.5	11	5.6	7.1	13	11
		S2	−2	N	−2.5		17			25	23		
+0.2	2.0	N	−3	-	-		47	10	15	290	96	120	92
		A1	−3	N	−3.5	0.097							
+0.1	1.6	N	−2.5	-	-		1.9	4.4	9.8	62	58	16	35
		A1	−2	N	−2.5	0.062							
-0.1	1.6	N	−2.5	-	-		1.1	1.2	6.2	49	29	11	28
		A1	−2	N	−2.5	0.032							
-0.2	2.0	N	−3	-	-		3.3	1.9	14	98	34	96	78
		A1	−3	N	−3.5	0.042							
-0.495	1.9	N	−2.5	-	-		2.2	1.1	11	89	29	89	71
		A1	−2	N	−2.5	0.036							

Table 3.1: Initial-value calculations for the vortices in group 1 with an attracting basin where the difference between the initial and final states of the vortex is dominated by A1 symmetry. For a single vortex, each row represents a simulation with different perturbations of the vortex in the initial conditions' cloud (i.e., for $j = 1$, $j = 2$, etc). The perturbations for each case are indicated by P1 and P2, with the initial amplitudes respectively denoted by $A_{IC,P1}$ and $A_{IC,P2}$. Here the perturbations are the linearly unstable eigenmode(s) of the vortex examined, or white noise which is denoted by using the letter N. The most unstable eigenmodes (i.e. those with the fastest growth rates in terms of vortex turnaround times) are designated with the bold font, with their growth rate's numerical values shown under the column '$\sigma\,(\tau^{-1})$' in the table. The number of total simulation turnaround times t_f for these cases is between 150 and 660. The numerically computed values of d_j are $O(10^{-4})$ indicating that, there is a basin of attraction that the vortices evolve to. Furthermore, D_c and D_s values are $O(10^{-2})$ in all the cases, so the final equilibria remain similar to the initial equilibria (i.e., in the L2 norm terms). The indicated changes of the Rossby number δRo_j (i.e., $O(10^{-3})$) and the Burger number δBu_j (i.e., $O(10^{-2})$) also show the small sizes of the attracting basins here, and the indicated changes in the Rossby number ΔRo (i.e., $O(10^{-2})$) and the Burger number ΔBu (i.e., $O(10^{-2})$) further show the similarity between the final and initial equilibria. For cases with two sets of different initial conditions, the values of d_j are equal to each other. The same is true for the magnitudes of δRo_j and δBu_j. However note that, $\delta Ro_j < 0$ for one simulation, and $\delta Ro_j > 0$ for the other. The same holds for the Burger number. $EN'_{\infty,j}$ is approximately-steady for the cases in the table.

Init. Eq.		**Perturbations**				$\boldsymbol{\sigma(\tau^{-1})}$	**Differences (L2 norms)**			**Differences (*Ro* and *Bu*)**			
$\widetilde{Ro}$	$\widetilde{Bu}$	P1	$\log_{10}[A_{IC,P1}]$	P2	$\log_{10}[A_{IC,P2}]$		$d_j(10^{-5})$	$D_c(10^{-3})$	$D_s(10^{-2})$	$\delta Ro_j(10^{-4})$	$\delta Bu_j(10^{-4})$	$\Delta Ro(10^{-4})$	$\Delta Bu(10^{-3})$
+0.5	0.65	**A1**	−2	N	−2.5	0.26	700	16	5.1	64	100	270	57
		S2	−2	N	−2.5								
+0.5	1.0	A1	−2	N	−2.5	0.20	33	11	3.6	24	42	100	28
		S2	−2	N	−2.5								
+0.4	0.65	A1	−3	N	−3.5	0.18	570	13	5.7	50	88	210	55
		S2	−2	N	−2.5								
+0.2	0.45	A1	−3	N	−3.5	0.11	570	11	16	44	110	96	34
		S2	−3	N	−3.5								
+0.2	0.75	N	−2.5	-	-	0.079	20	5.4	8.2	9.8	24	24	13
		S2	−2	N	−2.5								
+0.1	0.6	N	−2.5	-	-	0.049	12	6.7	15	6.7	18	11	10
		S2	−2	N	−2.5								
+0.05	0.45	N	−2.5	-	-	0.048	3.3	8.7	21	2.3	5.8	6.0	8.9
		S2	−2	N	−2.5								
-0.18	0.17	N	−2.5	-	-	0.021	420	14	32	11	18	48	8.3
		S2	−2	N	−2.5								

Table 3.2: As in table 3.1, but for the evolution of the vortices in group 2 with an attracting basin where the difference between the initial and final states of the vortex is dominated by S2 symmetry. The number of total simulation turnaround times t_f for these cases is between 140 and 520. The d_j and D_c here (and δRo_j, δBu_j, ΔRo and ΔBu) are $O(10^{-3})$ and $O(10^{-2})$ (and $O(10^{-3})$, $O(10^{-2})$, $O(10^{-2})$ and $O(10^{-2})$), respectively; hence showing the small sizes of the attracting basins of the vortices, and closeness of the cores in the final and initial equilibria. However, for these cases, the vortex's shield breaks into two satellite vortices. Despite such changes, for this family of final equilibria we find that the D_s has intermediate values $\lesssim 0.4$, and its final equilibria therefore are Gaussian-like. $EN'_{\infty,j}$ is approximately-steady for the cases in the table.

Init. Eq.		Perturbations				$\sigma(\tau^{-1})$	Differences (L2 norms)					Differences (Ro and Bu)			
$\widetilde{Ro}$	$\widetilde{Bu}$	P1	$\log_{10}[A_{IC,P1}]$	P2	$\log_{10}[A_{IC,P2}]$		$d_j(10^{-3})$	$D_c(10^{-1})$	$D_s(10^{-1})$	$F_c(10^{-3})$	$F_s(10^{-1})$	$\delta Ro_j(10^{-3})$	$\delta Bu_j(10^{-3})$	$\Delta Ro(10^{-3})$	$\Delta Bu(10^{-2})$
-0.05	0.15	N	−2.5	-	-										
		S2	−3	N	−3.5	0.053	4.8	3.5	4.3	17	6.0	1.2	3.8	5.3	1.1
+0.45	0.3	A2	−3.5	-	-		4.2					29	32		
		A3	−3.5	-	-	1.5	2.9					12	21		
		A4	−3.5	-	-		5.4					23	20		
		S2	−3.5	-	-		7.1	8.0	8.3	17	5.6	34	25	250	30
		S3	−3.5	-	-		8.0					25	40		
		S4	−3.5	-	-		6.5					19	9.0		
		N	−3.5	-	-		7.5					34	33		
+0.4	0.45	**A1**	−2	N	−2.5	0.40	4.9					23	11		
		S1	−2	N	−2.5		2.9	3.5	3.8	9.4	4.4	8.0	12	75	15
		S2	−2	N	−2.5		6.7					15	23		
+0.05	0.15	**A1**	−3	N	−3.5	0.16									
		S2	−3	N	−3.5		5.8	5.2	6.7	19	6.4	8.7	9.9	22	12

Table 3.3: As in table 3.1 again, but for the vortices in groups 3a and 3b with an attracting basin where the difference between the initial and final states of the vortices is not dominated by a single symmetry. The case above the bold line is for an anticyclone in group 3a, which has two satellite vortices, both residing on the mid-plane ($z = 0$) of vortex (as indicated the fastest growing eigenmode of this case has S2 symmetry). Below the bold line three cases are demonstrated for three group 3b cyclones, which have satellite vortices again, however here there is one or two satellite vortices above vortex's mid-plane and one or two below it (as indicated the fastest growing eigenmode of these cases have A1 symmetry). The number of total simulation turnaround times t_f for the group 3a (and group 3b) cases is between 180 and 220 (and between 140 and 390). The δRo_j, δBu_j and d_j here are again small, i.e., $O(10^{-2})$, $O(10^{-2})$ and $O(10^{-3})$, respectively, which is because of the small sizes of the attracting basins of groups 3a and 3b's final equilibria. However, noting that the ΔRo, ΔBu, D_c and D_s all are $O(0.1)$, neither the core nor the shield remain similar between the final and initial equilibria. Also here, F_c, and F_s (i.e., previously defined in the text) have values of $O(10^{-2})$, and $O(10^{-1})$, showing that the vortex's core is near a Gaussian vortex's core, but nevertheless, its shield is not (i.e., it breaks into smaller vortices). $EN'_{\infty,j}$ is approximately-steady for the cases in the table.

Init. Eq.		**Perturbations**				$\boldsymbol{\sigma(\tau^{-1})}$
$\widetilde{Ro}$	$\widetilde{Bu}$	P1	$\log_{10}[A_{IC,P1}]$	P2	$\log_{10}[A_{IC,P2}]$	
+0.2	0.1	A2	−4	-	-	
		A3	−4	-	-	
		S4	−4	-	-	
		A2	−4	A3	−4	
		A2	−4	N	−4.5	
		A3	−4	**A4**	−4	2.9
		A3	−4	N	−4.5	
		A4	−4	-	-	
		S2	−4	-	-	
		S3	−4	-	-	
		A2	−4	A4	−4	
		A4	−4	N	−4.5	
		S2	−4	N	−4.5	
		S3	−4	N	−4.5	
		S4	−4	N	−4.5	

Table 3.4: As in table 3.1 again, but for a group 4 vortex, which can split. Rows one to seven show the cases, where the vortex remains whole. For the rest of the cases (i.e., below the partial line) the vortex splits into two separate parts moving away radially. The number of total simulation turnaround times t_f for the non-splitting cases and the splitting cases is between 120 and 380, and between 24 and 57.

Init. Eq.		**Perturbations**				$\boldsymbol{\sigma(\tau^{-1})}$	**Differences (L2 norms)**		
$\widetilde{Ro}$	$\widetilde{Bu}$	P1	$\log_{10}[A_{IC,P1}]$	P2	$\log_{10}[A_{IC,P2}]$		$d_j(10^{-5})$	$D_c(10^{-3})$	$D_s(10^{-5})$
-0.1	0.07	**A4**	−4	-	-	67	6.2		
		N	−4.5	-	-		12	1.9	16
		A4	−4	N	−4.5		6.4		
-0.2	0.12	**A4**	−4	-	-	57	9.0		
		N	−4.5	-	-		39	4.4	18
		A4	−4	N	−4.5		11		
-0.3	0.17	**A4**	−4	-	-	32	2.5		
		N	−4.5	-	-		10	3.0	8.9
		A4	−4	N	−4.5		2.7		
-0.4	0.2	**A4**	−4	-	-	22	3.6		
		N	−4.5	-	-		11	2.3	8.2
		A4	−4	N	−4.5		5.9		

Table 3.5: Initial-value simulations for Gaussian vortices that have $N_c^2 < 0$ (group 5) and an attracting basin. Note also that, there is a clear S4 symmetry (see the part describing group 5's dominant symmetries in table 3.6's caption) corresponding to the difference between the initial and final equilibria of these cases, and their core always splits vertically into two radially-aligned cores (i.e., see figures 3.15 and 3.16). The table symbols here have the same interpretation, as the ones in tables 3.1 to 3.4. For the cases in this table, however, δRo_j, δBu_j, ΔRo, and ΔBu are not shown, because their previous definitions do not lend themselves, as they did before, to the final equilibria of these vortices (i.e., these final equilibria have two cores). The number of total simulation turnaround times t_f for these cases is between 80 and 120. The d_j values for group 5 are also very small (i.e., $O(10^{-4})$, or even smaller), which is because of the small size of the attraction basins of group 5's final equilibria. The D_c and D_s values are of orders, 10^{-3} and 10^{-4}, or smaller, here, showing that for group 5 the initial and final equilibria remain close. $EN'_{\infty,j}$ is approximately-steady for the cases in the table.

their shields breaking into two satellite vortices (on the vortex midplane). Again, a more quantitative description of the above statements is presented via our initial-value calculations for group 2 cases in table 3.2. The quantities d_j and D_c for these vortices (and the δRo_j, δBu_j, ΔRo and ΔBu also) have values of $O(10^{-3})$ and $O(10^{-2})$, or smaller (and have values of $O(10^{-3})$, $O(10^{-2})$, $O(10^{-2})$ and $O(10^{-2})$, or smaller), for the cases we examined in this group, therefore indicating the small size of the attraction basins for group 2 vortices, and also closeness of the vortex cores in their final and initial equilibria. However as was explained above, for group 2 vortices the shield sometimes breaks into two satellite vortices on the midplane of the vortex. Even with these changes, for the family of group 2 final equilibria we show that the D_s (see table 3.2) has intermediate values of $\lesssim 0.4$, and group 2 therefore has Gaussian-like final equilibria. Also, for the vortices of group 2 the remainder flow shows an S2 dominant symmetry, which is presented by the $\Gamma_{S2} \gtrsim 0.9$ for table 3.6's group 2 cases (and with the contributions of $\Gamma_{A1} \simeq 0.04$ and $\Gamma_{S4} \simeq 0.02$ shown to be much smaller). Furthermore it can be shown that for the group 2 vortices, for which all A1 eigenmodes are neutrally stable (table 3.6's last four group 2 cases), the difference flow only has S symmetry (i.e., meaning that for such cases $\Gamma_{\mathrm{A1}} < 0.01$). The time variation of different properties of a group 2 vortex are in figure 3.4, demonstrating how the vortex reaches quasi-steady state, and example group 2 vortices are illustrated in figures 3.5 and 3.6.

For the family of group 2 final equilibria we have shown 4 example cases in figure 3.7, where the Gaussian-like final equilibria have broken shields around their cores. As shown in figure 3.7, as the Bu increases, from panel (a) to panel (d), we find smaller parts of the shield broken/deformed. This can be seen, by the fact that the dominant symmetry of these group 2 vortices is S2 and by noting that for low values of Bu, the fastest growing S2 eigenmodes (i.e., of the Gaussian equilibria of group 2) are very concentrated in the shields, and as Bu increases, the radial structure spreads into their core, e.g., as demonstrated by equation (2.28) and figure 2.13(b) of chapter 2 using the fraction of the eigenmode enstrophy in the vortex shield given by S_{shield}, which for the vortices with S2 fastest growing eigenmodes has values that decrease from 0.94 at low Bu to 0.55 at high Bu. Also consistent with this is that group 2's D_s values decrease (see table 3.2) as Bu increases from 0.32 at low Bu to 0.036 at high Bu.

Groups 3a and 3b

These vortices have very fast growth rates ($\sigma \sim 0.1\tau^{-1}$, or lager) and thus quickly evolve from their initial equilibrium state towards a quasi-steady final equilibrium, where we find that neither their core nor their shield look similar to the Gaussian equilibrium's core and shield. Here we use group 3a for anticyclones, with two cyclonic satellite vortices that reside on the vortex's midplane i.e., $z = 0$ (for the vortices of group 3a the fastest growing eigenmode has S2 symmetry). Also, group 3b is to demonstrate initial cyclones which have one or two satellite vortices that are above vortex's midplane, and one or two that are below it (for the vortices of group 3b the fastest growing eigenmode has A1 symmetry). Our initial-value calculations for groups 3a and 3b are in table 3.3. The quantities δRo_j, δBu_j and d_j for groups 3a and 3b are shown to be small, with values $O(10^{-2})$, $O(10^{-2})$ and $O(10^{-3})$, or

Group	Init. Eq.		Symmetry	Enstrophy Values					
	$\widetilde{Ro}$	$\widetilde{Bu}$		Γ_{A1}	Γ_{A2}	Γ_{A4}	Γ_{S1}	Γ_{S2}	Γ_{S4}
1	+0.5	1.6	A1	0.93	–	–	–	0.044	0.035
	+0.5	2.0	A1	0.93	–	–	–	0.040	0.034
	+0.4	1.4	A1	0.93	–	–	–	0.039	0.033
	+0.2	1.0	A1	0.92	–	–	–	0.042	0.035
	+0.2	1.3	A1	0.94	–	–	–	0.033	0.031
	+0.2	2.0	A1	0.94	–	–	–	0.032	0.030
	+0.1	1.6	A1	0.95	–	–	–	0.032	0.024
	−0.1	1.6	A1	0.95	–	–	–	0.028	0.022
	−0.2	2.0	A1	0.95	–	–	–	0.028	0.024
	−0.495	1.9	A1	0.96	–	–	–	0.022	0.020
2	+0.5	0.65	S2	0.064	–	–	–	0.92	0.011
	+0.5	1.0	S2	0.043	–	–	–	0.93	0.036
	+0.4	0.65	S2	0.062	–	–	–	0.93	0.012
	+0.2	0.45	S2	0.057	–	–	–	0.93	0.012
	+0.2	0.75	S2	–	–	–	–	0.95	0.048
	+0.1	0.6	S2	–	–	–	–	0.95	0.048
	+0.05	0.45	S2	–	–	–	–	0.96	0.037
	−0.18	0.17	S2	–	–	–	–	0.96	0.044
3a	−0.05	0.15	–	–	–	–	0.062	0.45	0.49
3b	+0.45	0.3	–	0.27	–	–	–	0.084	0.65
	+0.4	0.45	–	0.26	–	–	–	0.088	0.65
	+0.05	0.15	–	–	–	–	0.10	0.16	0.74
5	−0.1	0.07	S4	–	–	0.033	–	0.017	0.95
	−0.2	0.12	S4	–	–	0.032	–	0.016	0.95
	−0.3	0.17	S4	–	–	0.027	–	0.017	0.96
	−0.4	0.2	S4	–	–	0.028	–	0.020	0.95

Table 3.6: The dimensionless enstrophies, Γ_{A1}, Γ_{A2} Γ_{A4}, Γ_{S1}, Γ_{S2}, and Γ_{S4}, for different vortex groups, and their average final equilibria $\hat{\omega}$. $\Gamma_{A1} + \Gamma_{A2} + \Gamma_{A4} + \Gamma_{S1} + \Gamma_{S2} + \Gamma_{S4} \simeq 1$. The vortex dominant symmetries are indicated under 'Symmetry'. The values of the enstrophies for each of the final cloud's time-averaged equilibria $\langle \omega_j \rangle$ are within 0.02 of the enstrophy of the corresponding $\hat{\omega}$ that is demonstrated in the table. The dashes show symmetries for which the fractional enstrophy < 0.01. For group 1, and group 2 cases examined, $\Gamma_{A1} \gtrsim 0.9$, and $\Gamma_{S2} \gtrsim 0.9$, respectively. Furthermore, for the last four vortices of group 2, where all A1 eigenmodes are neutrally stable, the final equilibria clearly have S symmetries only (i.e., meaning that for such cases $\Gamma_{A1} < 0.01$). Also note that for the group 3a, and group 3b cases shown, even though Γ_{S4} has the largest value, we find that they have in fact no dominant symmetries. For the group 3a case shown, the largest value is for S enstrophies, whereas, for the group 3b cases with one satellite (or two satellites) above vortex midplane and one (or two) below it, the enstrophy values are represented by $\Gamma_{A1} \simeq 0.3$ (or $\Gamma_{S2} \simeq 0.2$) and $\Gamma_{S4} \simeq 0.7$ (or $\Gamma_{S4} \simeq 0.8$). For group 5 cases, it is shown that, as in groups 3a and 3b, the largest enstrophy values are for Γ_{S4}, but greater than those of groups 3a and 3b. The vortices of group 5 have an A4 fastest growing eigenmode, and an S4 dominant symmetry. There also is $\Gamma_{A4} \simeq 0.03$ in group 5's final equilibria, with much smaller values than the indicated values of $\Gamma_{S4} \simeq 0.95$ (with their $\Gamma_{S2} \simeq 0.02$ being small as well).

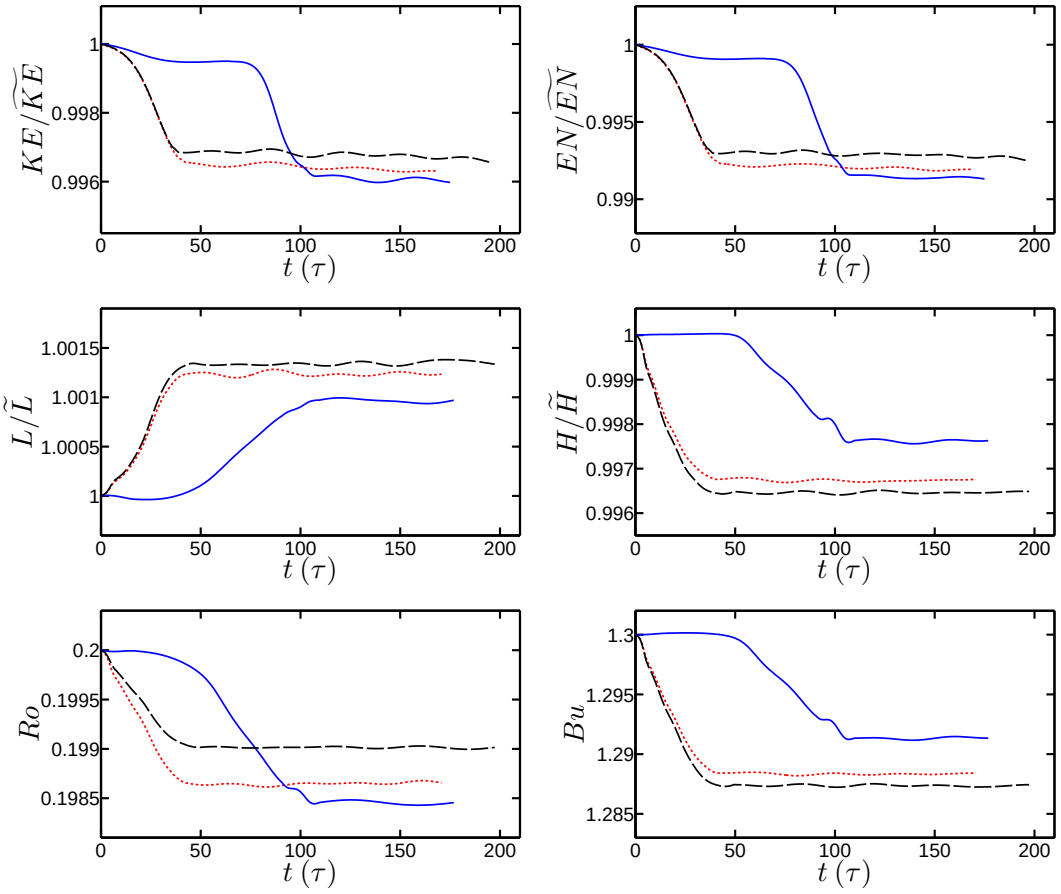

Figure 3.1: (Colour online) Kinetic energy $KE/\widetilde{KE}$, enstrophy $EN/\widetilde{EN}$, horizontal length scale $L/\widetilde{L}$, vertical length scale $H/\widetilde{H}$, Rossby number Ro, and Burger number Bu, for different perturbations of a group 1 vortex, showing how for these cases the vortex reaches quasi-steady state. Here $\widetilde{Ro} = 0.2$, and $\widetilde{Bu} = 1.3$. Different line styles (and colours, in colour version) are for different perturbations; the black long-dashed lines have perturbation amplitude (for definition of $A_{IC,i}$ see the text) $A_{IC,A1} = 10^{-2}$; the short-dashed lines (red, in colour) have $A_{IC,A1} = 10^{-2}$, and $A_{IC,N} = 10^{-2.5}$; and the solid lines (blue, in colour) have $A_{IC,S2} = 10^{-2}$, and $A_{IC,N} = 10^{-2.5}$. At quasi-steady state the fractional changes (fluctuation amplitude divided by mean) of all the quantities are smaller than $\sim 5 \times 10^{-4}$.

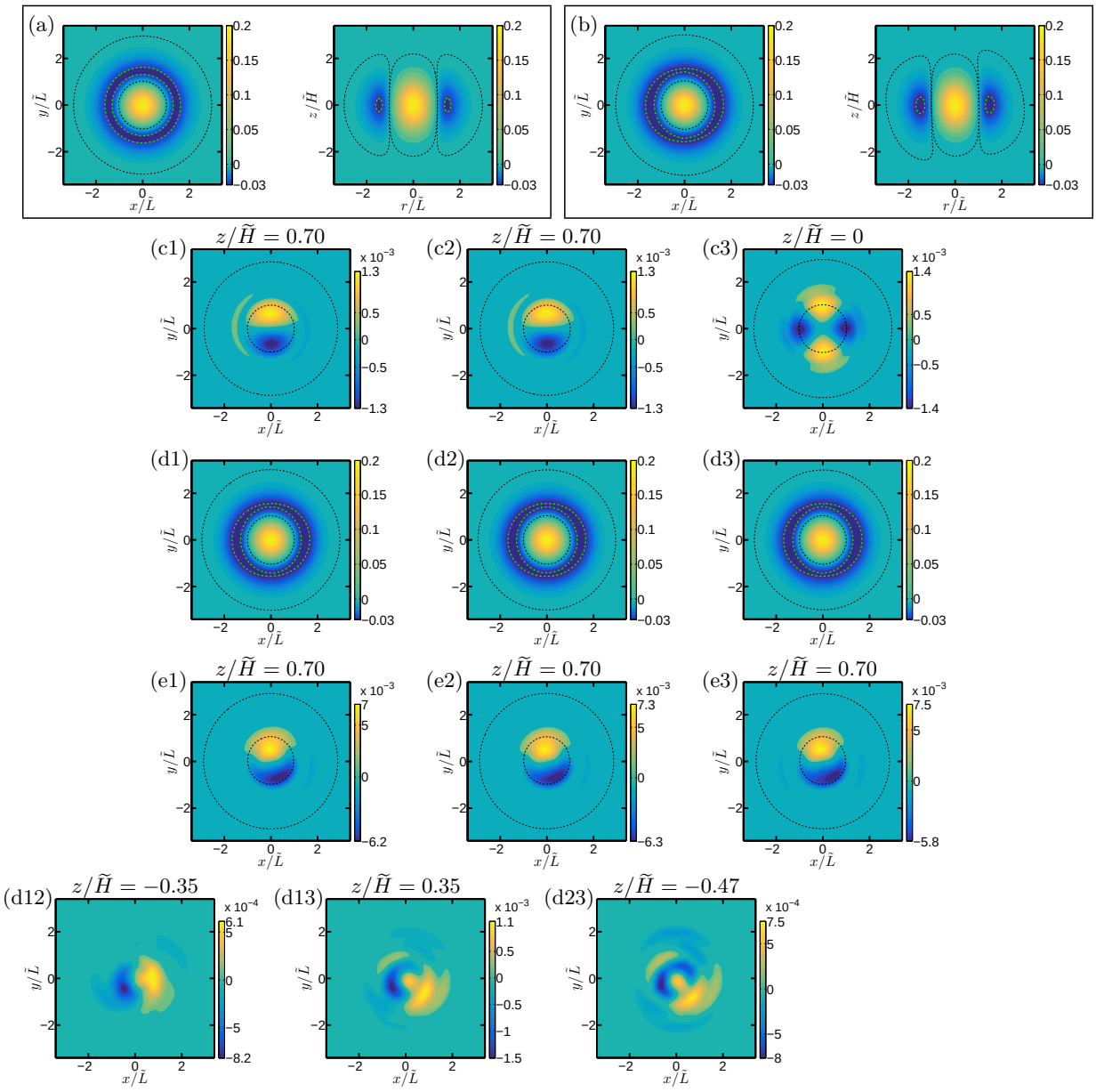

Figure 3.2: (Colour online) Vertical vorticity ω of a group 1 vortex for the Gaussian equilibrium $\tilde{\omega}$ and the average final equilibrium $\hat{\omega}$, as well as for the numerical quantities that describe the vortex evolution. Here $\widetilde{Ro} = 0.2$, $\widetilde{Bu} = 1.3$, and $f/\bar{N} = 0.1$. (a) and (b) show the $\tilde{\omega}$ and $\hat{\omega}$, respectively, where for each panel, the first figure is on the midplane of the vortex (i.e., $z = 0$), whereas the second figure outlines the vortex on the $(r - z)$ plane. For the average final equilibrium shown in (b), the $(r - z)$ plane has an azimuthal angle, chosen where the shield has its minimum vorticity value. The dashed-dotted lines (green, in colour) are for $0.1 \min[\omega]$, indicating that the vortex's shield remains almost axisymmetric here. The black dashed lines indicate the boundaries of the core and shield. Panels (c1) to (c3) demonstrate for the initial cloud, three different perturbation sets, each shown on the horizontal plane with the maximum magnitude of the ω. The perturbation amplitude(s) for panel (c1) is $A_{IC,A1} = 10^{-2}$; for panel (c2) are $A_{IC,A1} = 10^{-2}$, and $A_{IC,N} = 10^{-2.5}$; and for panel (c3) are $A_{IC,S2} = 10^{-2}$, and $A_{IC,N} = 10^{-2.5}$. For these three cases, panels (d1) to (d3) (given on the midplane of the vortex) show that the final cloud's time-averaged equilibria $\langle\omega_j\rangle$ resemble each other closely and panel (b)'s average final equilibrium $\hat{\omega}$. The differences between the time-averaged final equilibria and Gaussian equilibrium $\langle\omega_j\rangle - \tilde{\omega}$ in (e1) to (e3) (presented on the plane with maximum $|\omega|$) are small (fractional magnitudes $\simeq 7.5 \times 10^{-3}/0.1$), which is consistent with the initial-value calculations in table 3.1. (d12), (d13), and (d23) (presented on the plane with maximum $|\omega|$) show that the differences between each two time-averaged final equilibria $\langle\omega_{j_1}\rangle - \langle\omega_{j_2}\rangle$, $j_1 \neq j_2$ are small (smaller than the values of $\langle\omega_j\rangle - \tilde{w}$, given in (e1)-(e3)), with fractional magnitudes that have values $\simeq 1.5 \times 10^{-3}/0.1$.

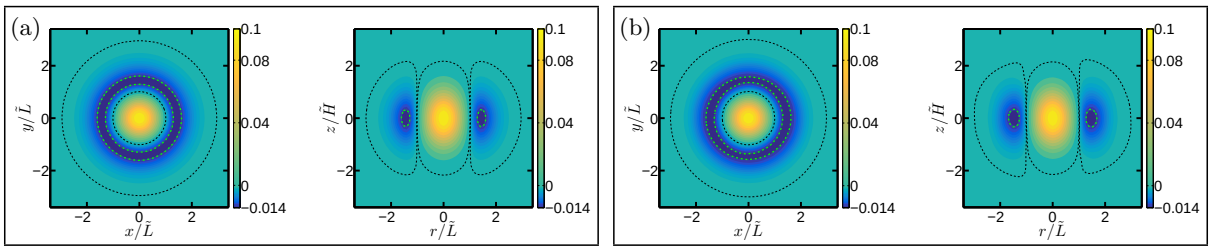

Figure 3.3: (Colour online) Similar to figure 3.2's panels (a) and (b), but for a group 1 vortex, with $\widetilde{Ro} = 0.1$, $\widetilde{Bu} = 1.6$, and $f/\tilde{N} = 0.1$. Figure 3.2's panel (b) and the average final equilibrium that is shown here, resemble each other closely, with the iso-contours of $0.1\,\min[\omega]$ and the boundaries for the cores and shields being similar for the two cases (the initial-value calculations for this group 1 case are in table 3.1).

smaller, respectively, which is due to the small size of the attraction basins for groups 3a and 3b vortices. However note that the quantities ΔRo, ΔBu, D_c and D_s are all $O(0.1)$, and neither the core nor the shield stay similar between their final equilibrium and the initial equilibrium (i.e., that is the axisymmetric Gaussian equilibrium for $Ro = \widetilde{Ro}$, and $Bu = \widetilde{Bu}$).

On the other hand, we find that the final equilibria's core for such cases can as well be shown to be near the core of a Gaussian equilibrium, that has $Ro = \widehat{Ro}$ and $Bu = \widehat{Bu}$. Nevertheless, the shield for group 3a and group 3b's final equilibria, does not remain similar to the initial shield – it breaks into smaller satellite vortices, on, or above/below vortex midplane, showing that the final equilibria are in fact non-Gaussian-like. The above statements are also consistent with the F_c, and F_s values in table 3.3, that are $O(10^{-2})$, or smaller, and $O(10^{-1})$.

We find here that groups 3a and 3b vortices clearly have no dominant symmetries. Furthermore, for group 3a vortices the "remainder" flow is largely symmetric, as shown by $\Gamma_{S1} \simeq 0.06$, $\Gamma_{S2} \simeq 0.45$, and $\Gamma_{S4} \simeq 0.49$ values for group 3a in table 3.6 below. Correspondingly, for the group 3b cases with one satellite above vortex's mid-plane and one below it, the remainder flow is shown to have partly A1 symmetry, and partly S4 symmetry (with the enstrophy values represented by $\Gamma_{\mathrm{A1}} \simeq 0.3$, $\Gamma_{\mathrm{S2}} \simeq 0.1$ and $\Gamma_{\mathrm{S4}} \simeq 0.6$ as demonstrated by table 3.6's first two group 3b cases). Also, for the group 3b cases with two satellites above vortex's mid-plane and two below it, the remainder flow shows partly S2 symmetry, and again partly S4 symmetry (with the enstrophy values here represented by $\Gamma_{\mathrm{S1}} \simeq 0.1$, $\Gamma_{\mathrm{S2}} \simeq 0.2$ and $\Gamma_{\mathrm{S4}} \simeq 0.7$ as shown by table 3.6's last group 3b case). Different vortex properties for cases in groups 3a and 3b, and how they reach quasi-steady state are shown in figures 3.8 and 3.10; the initial equilibrium, vortex evolution, and final equilibrium for a group 3a vortex are illustrated in figure 3.9, and two examples for group 3b vortices are demonstrated in figures 3.11 and 3.12.

Group 4

The vortices of this group can split, i.e., that is, the vortex remains whole for a set of initial conditions, whereas it can split for a different set of initial conditions (see table 3.4). Note

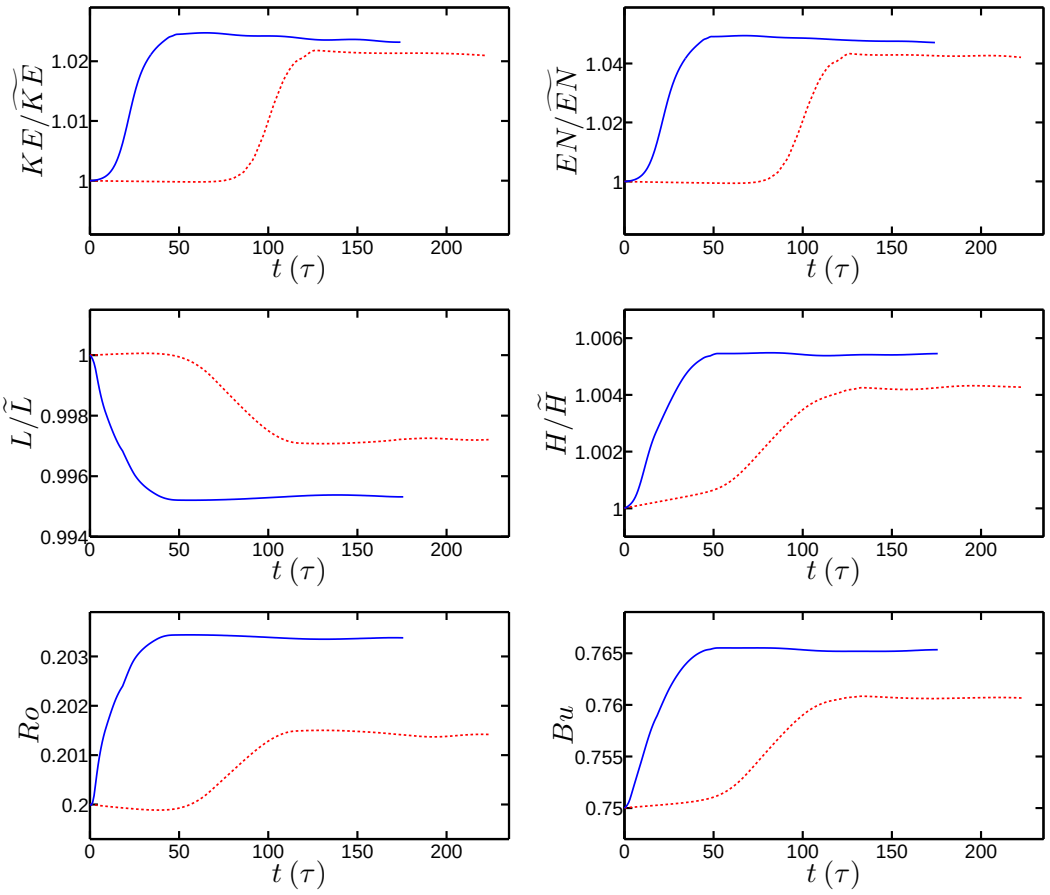

Figure 3.4: (Colour online) As in figure 3.1, but for the evolution of a vortex in group 2. Here $\widetilde{Ro} = 0.2$, and $\widetilde{Bu} = 0.75$. In this case, the dashed lines (red, in colour) have a perturbation amplitude of $A_{IC,N} = 10^{-2.5}$; and the solid lines (blue, in colour) have perturbation amplitudes of $A_{IC,S2} = 10^{-2}$, and $A_{IC,N} = 10^{-2.5}$. At quasi-steady state the fractional changes of all the quantities are smaller than ~ 0.004.

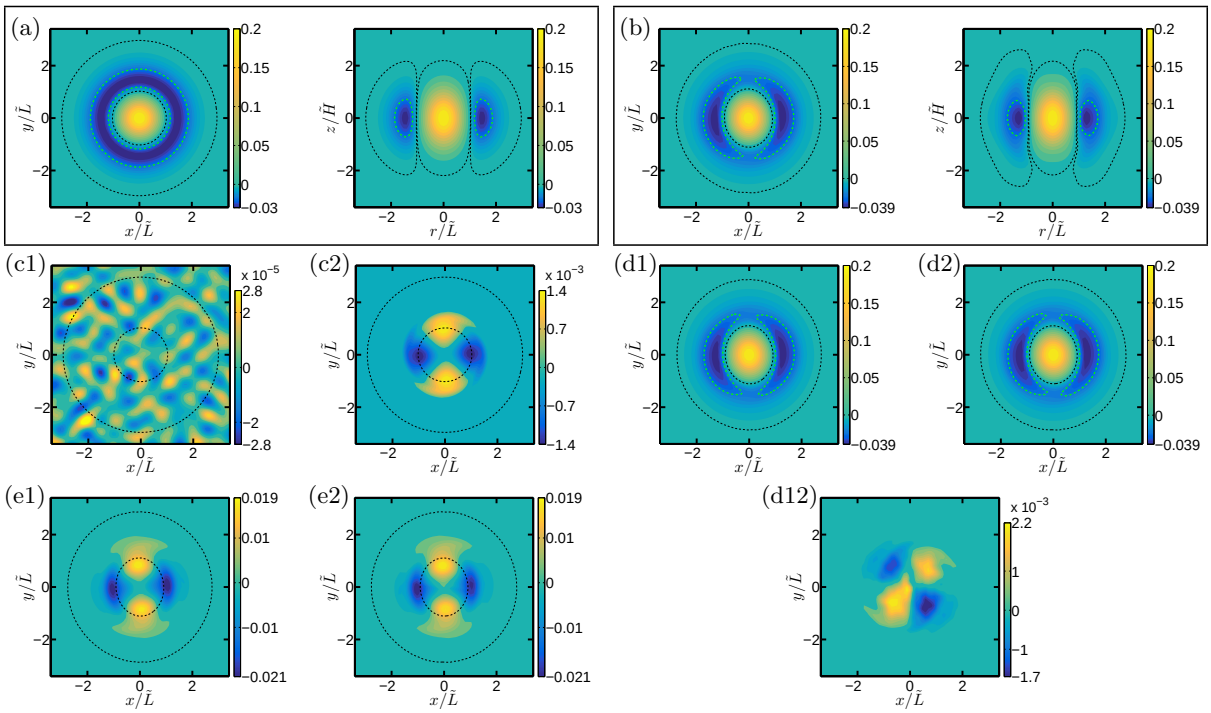

Figure 3.5: (Colour online) As in figure 3.2, but for a group 2 vortex with $\widetilde{Ro} = 0.2$, $\widetilde{Bu} = 0.75$, and $f/\bar{N} = 0.1$. For the equilibria shown here, the dashed-dotted lines (green, in colour) are for $0.6\,\mathrm{min}\,[\omega]$ showing that a region of the initial shield breaks into satellite vortices, with the other part of it remaining almost axisymmetric, as indicated by the shield's dashed line. In panel (b), therefore, the $(r-z)$ plane's azimuthal angle, is chosen where the satellite vortices shown by the dashed-dotted curves (green, in colour) have the largest magnitude. For this case, the perturbation amplitude(s) for panel (c1) is $A_{IC,N} = 10^{-2.5}$; and for panel (c2) are $A_{IC,S2} = 10^{-2}$, and $A_{IC,N} = 10^{-2.5}$. Panels (c1), (c2), (d1), (d2), (e1), (e2), and (d12) are all on the midplane of the vortex (which is where the satellite vortices are most prominent for this case). (d1) and (d2) show that the final cloud's time-averaged equilibria $\langle\omega_j\rangle$ resemble each other closely and panel (b)'s average final equilibrium $\hat{\omega}$. The differences $\langle\omega_j\rangle - \tilde{\omega}$ in (e1) and (e2) for the core are small (fractional magnitudes $\simeq 0.02/0.2$), and for the shield are large (fractional magnitudes $\simeq 0.02/0.03$), which is consistent with the initial-value calculations in table 3.2. (d12) shows that the difference $\langle\omega_1\rangle - \langle\omega_2\rangle$ is small as well (smaller than the values of $\langle\omega_j\rangle - \tilde{\omega}$, given in (e1) and (e2)), with a fractional magnitude that has a value $\simeq 0.002/0.1$.

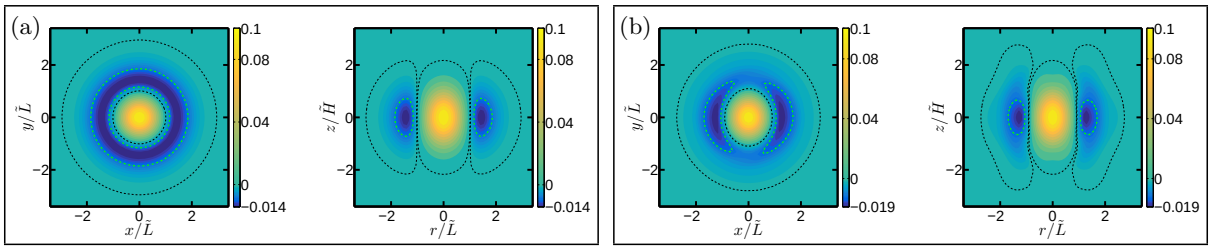

Figure 3.6: (Colour online) Similar to figure 3.5's panels (a) and (b), but for a group 2 vortex, with $\widetilde{Ro} = 0.1$, $\widetilde{Bu} = 0.6$, and $f/\bar{N} = 0.1$. Figure 3.5's panel (b) and the average final equilibrium that is shown here, resemble each other closely, with the iso-contours of $0.6\,\min[\omega]$ and the boundaries for the cores and shields, being similar for the two cases (the initial-value calculations for this group 2 case are in table 3.2).

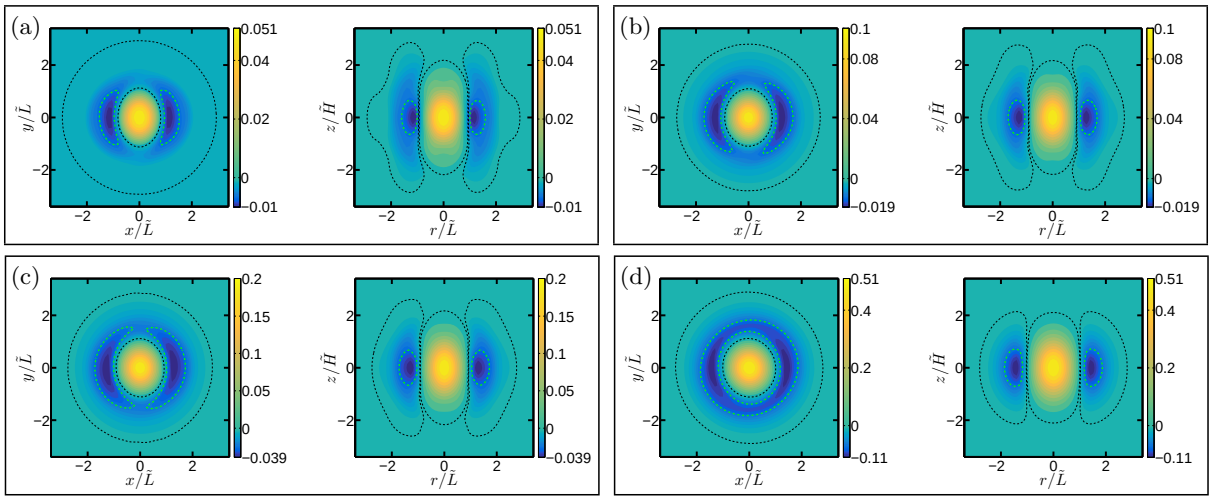

Figure 3.7: (Colour online) The average final equilibrium $\hat{\omega}$ for four vortices (panels a-d) in group 2 with $\widetilde{Ro} = 0.05$, 0.1, 0.2, and 0.5; and $\widetilde{Bu} = 0.45$, 0.6, 0.75, and 1.0. The panels are similar to panel (b) of figure 3.5. As $\widetilde{Bu}$ increases from (a) to (c), the broken region shown by the dashed-dotted curves (green, in colour) becomes smaller and the shield (contiguous) region becomes larger. As $\widetilde{Bu}$ increases, consistently, the values of S_{shield} (see §3.3) and D_s (see table 3.2) decrease, and the shield becomes more axisymmetric. For the last case in panel (d), the dashed-dotted curve (green, in colour) is shield-like (where the shield is nearly axisymmetric).

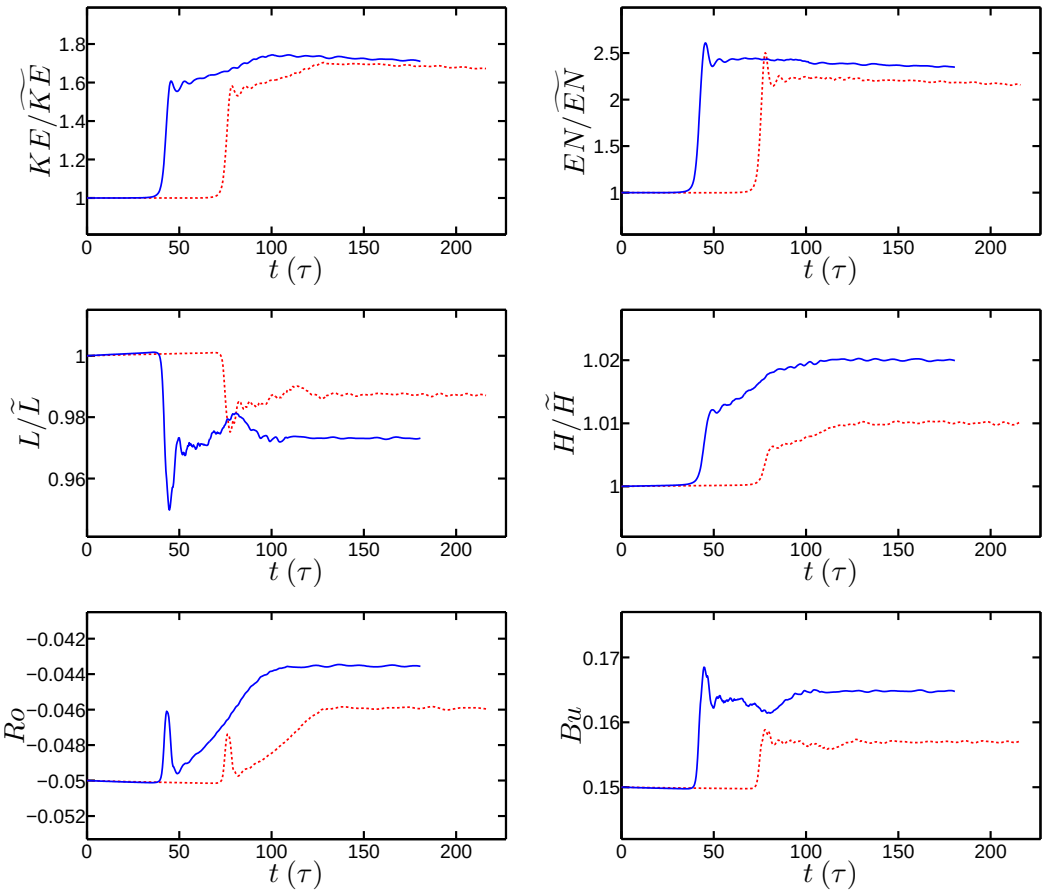

Figure 3.8: (Colour online) As in figure 3.1 again, but for a vortex in group 3a (midplane satellites only). Here $\widetilde{Ro} = -0.05$, and $\widetilde{Bu} = 0.15$. In this case, the dashed lines (red, in colour) have a perturbation amplitude of $A_{IC,N} = 10^{-2.5}$; and the solid lines (blue, in colour) have perturbation amplitudes of $A_{IC,S2} = 10^{-3}$, and $A_{IC,N} = 10^{-3.5}$. At quasi-steady state the fractional changes of all the quantities are smaller than ~ 0.04.

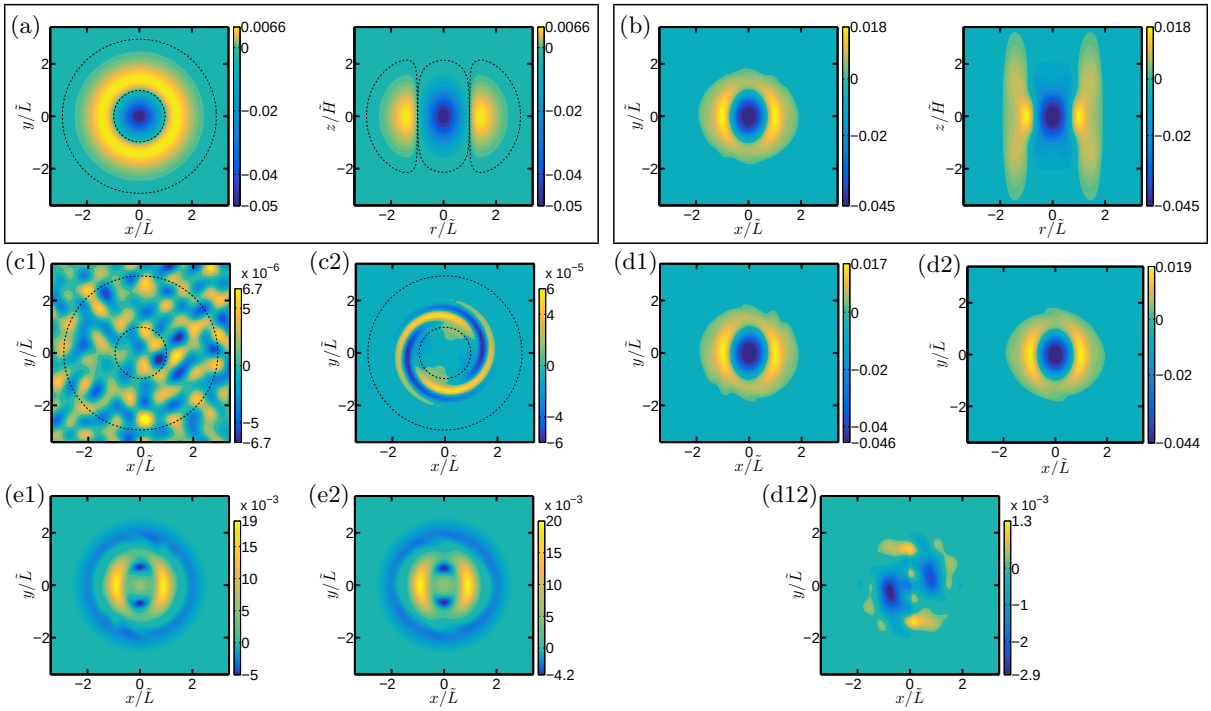

Figure 3.9: (Colour online) As in figure 3.2, but for a group 3a vortex with $\widetilde{Ro} = -0.05$, $\widetilde{Bu} = 0.15$, and $f/\bar{N} = 0.1$. The anticyclone shown in panel (b)† has two cyclonic satellites on the vortex midplane, with *neither* the core *nor* the shield remaining similar between the final and initial equilibria. In panel (b), the $(r - z)$ plane's azimuthal angle is where the satellite vortices have the largest ω magnitude. The black dashed lines in panels (a), (c1) and (c2) show the boundaries of the Gaussian equilibrium's core and shield. The perturbation amplitude(s) for panel (c1) is $A_{IC,N} = 10^{-2.5}$; and for panel (c2) are $A_{IC,S2} = 10^{-3}$, and $A_{IC,N} = 10^{-3.5}$. Panels (c1), (c2), and the following panels, are all on the $z = 0$ horizontal plane here. Similar to previous cases, here we find that panels (d1) and (d2)'s time-averaged final equilibria $\langle\omega_j\rangle$ are in fact very similar (we have not shown here, the final equilibria's core and shield, due to them being different than the core and shield of the axisymmetric equilibrium, shown in (a)). The differences $\langle\omega_j\rangle - \tilde{\omega}$ in (e1) and (e2) are large (i.e., fractional magnitudes $\simeq 0.02/0.03$), which is consistent with the initial-value calculations in table 3.3. (d12) shows that the difference $\langle\omega_1\rangle - \langle\omega_2\rangle$ is small, with a fractional magnitude $\simeq 0.003/0.03$. [†Note: Here, for the highly non-axisymmetric final equilibria of groups 3a and 3b, an average over different final equilibria can be defined only after implementing the required rotations and translations (see §3.2).]

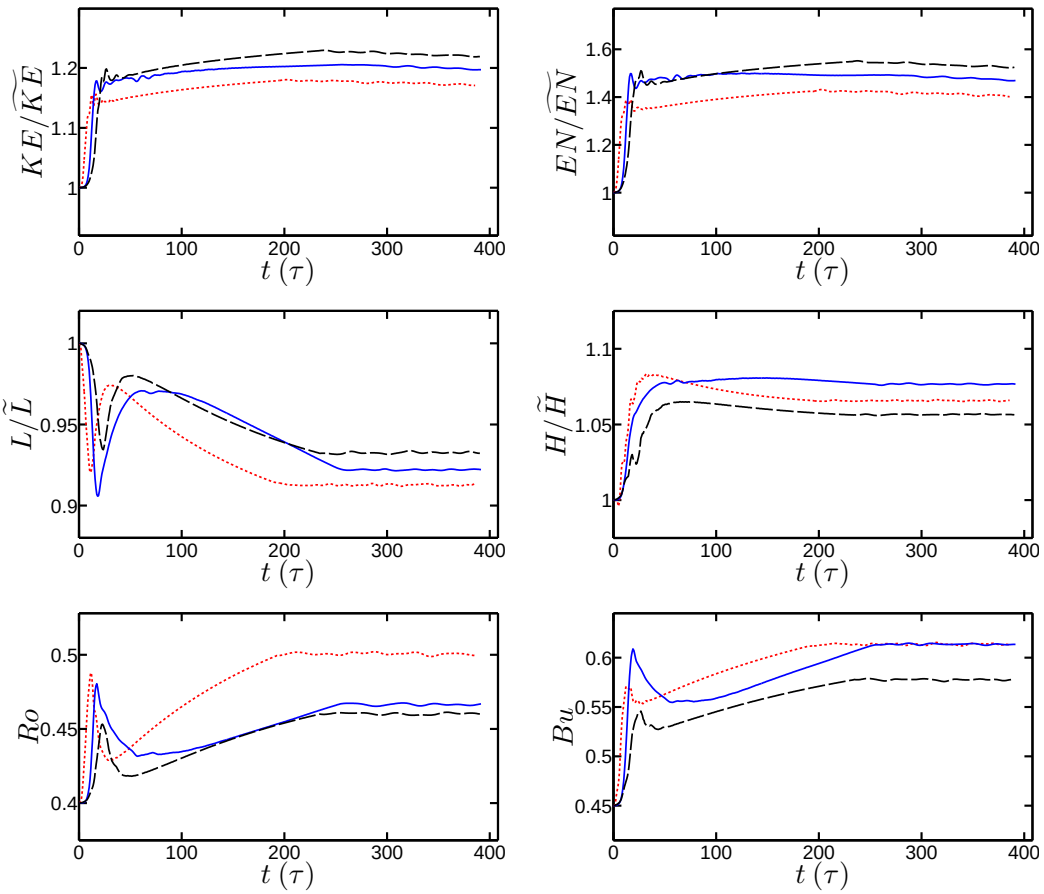

Figure 3.10: (Colour online) As in figure 3.1 again, but for a vortex in group 3b (which has satellites above and below vortex midplane). Here $\widetilde{Ro} = 0.4$, and $\widetilde{Bu} = 0.45$. Different lines here, are to demonstrate different perturbations. The short-dashed lines (red, in colour) have amplitudes of $A_{IC,A1} = 10^{-2}$, and $A_{IC,N} = 10^{-2.5}$; the black long-dashed lines have amplitudes of $A_{IC,S1} = 10^{-2}$, and $A_{IC,N} = 10^{-2.5}$; and the solid lines (blue, in colour) have amplitudes of $A_{IC,S2} = 10^{-2}$, and $A_{IC,N} = 10^{-2.5}$. In this case, at quasi-steady state the fractional changes of all the quantities are smaller than ~ 0.04.

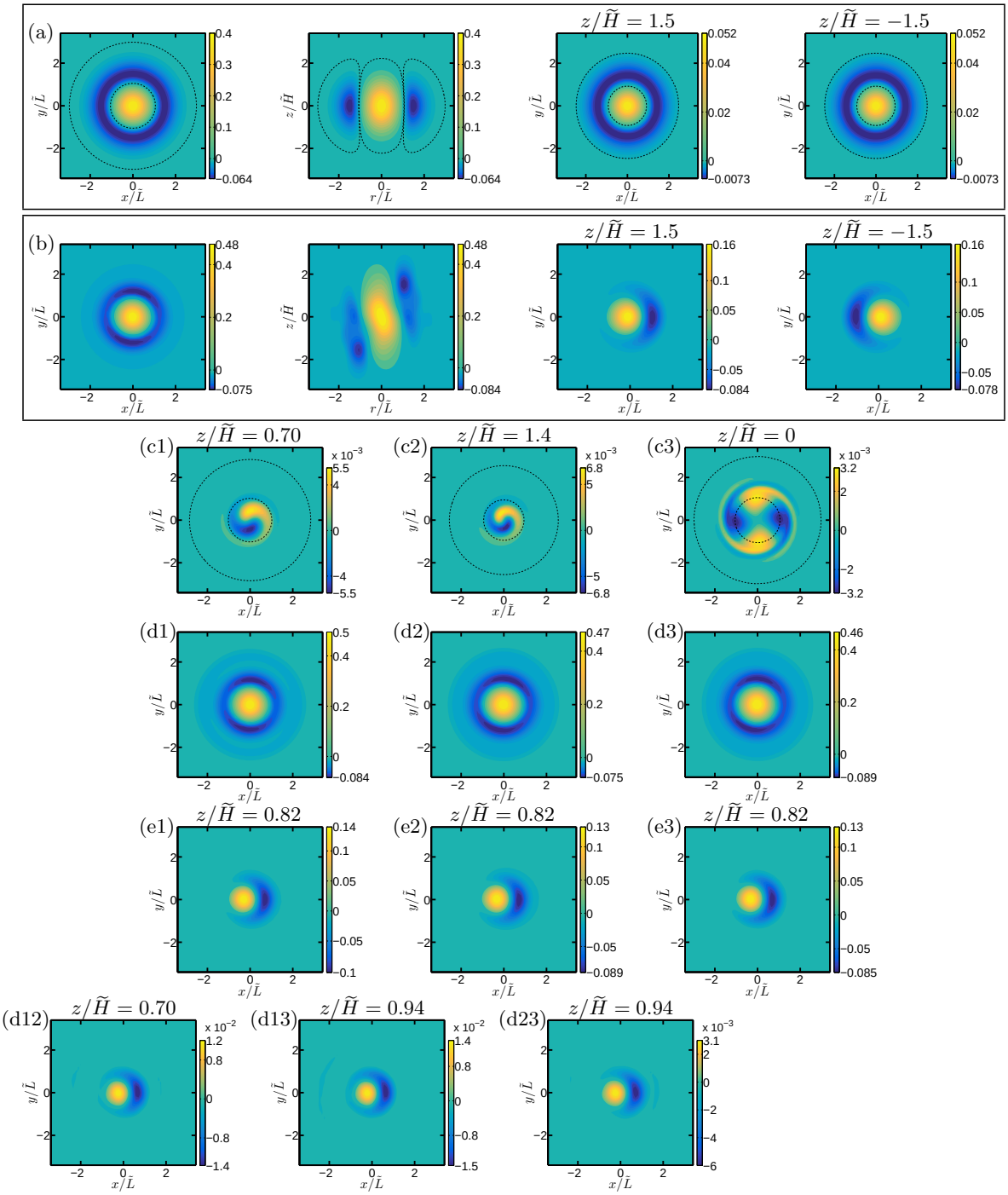

Figure 3.11: (Colour online) As in figure 3.2, but for a group 3b vortex with $\widetilde{Ro} = 0.4$, $\widetilde{Bu} = 0.45$, and $f/\tilde{N} = 0.1$. The cyclone in panel (b), not only has midplane satellites vortices, but also has a satellite vortex above $z = 0$ (and one below it as well), so in addition to the (a) and (b)'s first figures showing vortex midplane, two z = constant $\neq 0$ planes (i.e., where the satellites have their largest vorticity values) are added within panels (a) and (b), with the headers above each, demonstrating the plane on which the vortex is shown. The other parts of the figure are as in figure 3.9 (however here, the planes with maximum $|\omega|$ in panels (c1) to (c3), (e1) to (e3), and (d12) to (d23) can have $z \neq 0$ values, as shown by the headers above the figures). The perturbation amplitudes for panel (c1) are $A_{IC,A1} = 10^{-2}$, and $A_{IC,N} = 10^{-2.5}$; for panel (c2) are $A_{IC,S1} = 10^{-2}$, and $A_{IC,N} = 10^{-2.5}$; and for panel (c3) are $A_{IC,S2} = 10^{-2}$, and $A_{IC,N} = 10^{-2.5}$. For this case, the differences $\langle\omega_j\rangle - \tilde{\omega}$ in (e1) to (e3) are large (i.e., fractional magnitudes $\simeq 0.1/0.2$), which is consistent with the initial-value calculations in table 3.3. (d12), (d13), and (d23) show that the differences $\langle\omega_{j_1}\rangle - \langle\omega_{j_2}\rangle$, $j_1 \neq j_2$ are small, with fractional magnitudes $\simeq 0.02/0.3$.

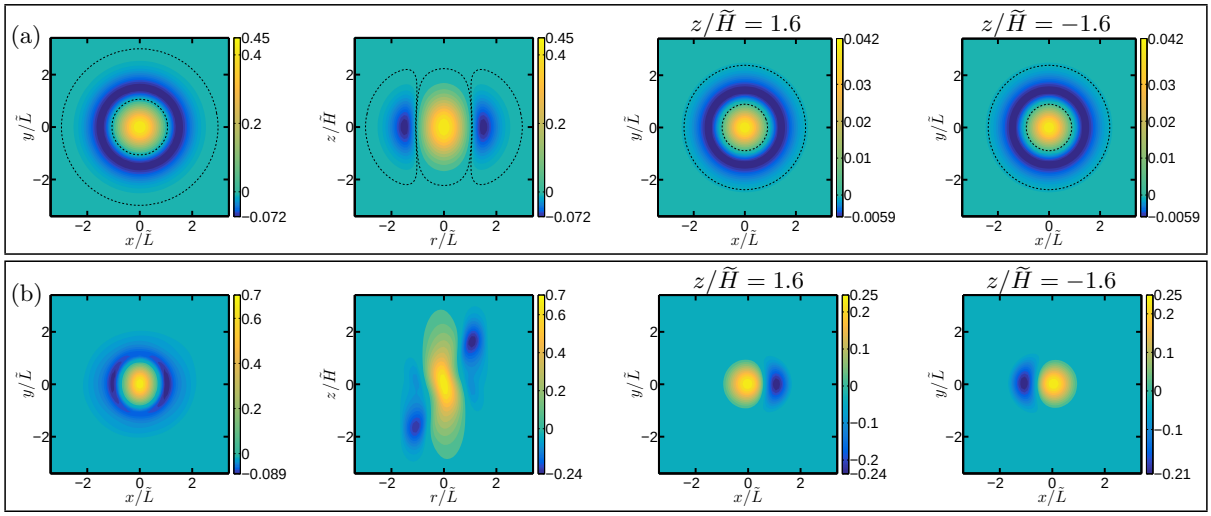

Figure 3.12: (Colour online) As panels (a) and (b) of figure 3.11, but for a group 3b vortex, with $\widetilde{Ro} = 0.45$, $\widetilde{Bu} = 0.3$, and $f/\bar{N} = 0.1$. The average final equilibrium has a satellite above its midplane, and one below it (the initial-value calculations for this group 3b case are in table 3.3).

the very fast growth rate shown for the group 4 vortex in table 3.4 ($\sigma \sim 1\,\tau^{-1}$). A group 4 vortex is illustrated in figure 3.13, by showing its different final equilibria; the equilibria in panels (b) and (c) are tripoles and pentapoles with two and four satellites, whereas for the cases shown in panels (d) and (e), the vortex splits into two tripoles moving away from the initial vortex's position in the radial direction. The initial and final equilibria in groups 1, 2, 3a, 3b, and 4, all have $N_c^2 > 0$.

Group 5

Group 5 includes vortices with $N_c^2 < 0$, that have heavy fluid over light fluid near their cores, for which the growth rate of the fastest-growing eigenmodes can be as large as $\sim 100\,\tau^{-1}$ (i.e., see chapter 2, §2.4, last paragraph, as well as figure 2.11). During a group 5 vortex's evolution, the core splits vertically into two similar parts that are approximately radially-aligned, and that are contained in the very vicinity of the initial vortex's core. Thus for group 5 vortices, the initial and final equilibria remain very close to each other. Our initial-value simulations in table 3.5 show that the d_j here are again small, $O(10^{-4})$, or even smaller, which is due to the small sizes of the attracting basins of the equilibria. The D_c, and D_s are of orders 10^{-3}, and 10^{-4} here indicating that for these cases, the final equilibrium remains close to the initial equilibrium. Note also that for group 5 cases, Ro and Bu are not defined, as these parameters' previous definitions cannot be implemented for group 5 vortices and their final equilibria (i.e., which have not one, but two cores). The vortices of group 5 have A4 fastest growing eigenmodes and S4 dominant symmetry difference flows (i.e., as indicated by the values of $\Gamma_{S4} \simeq 0.95$ shown for table 3.6's group 5 cases, with the contributions of

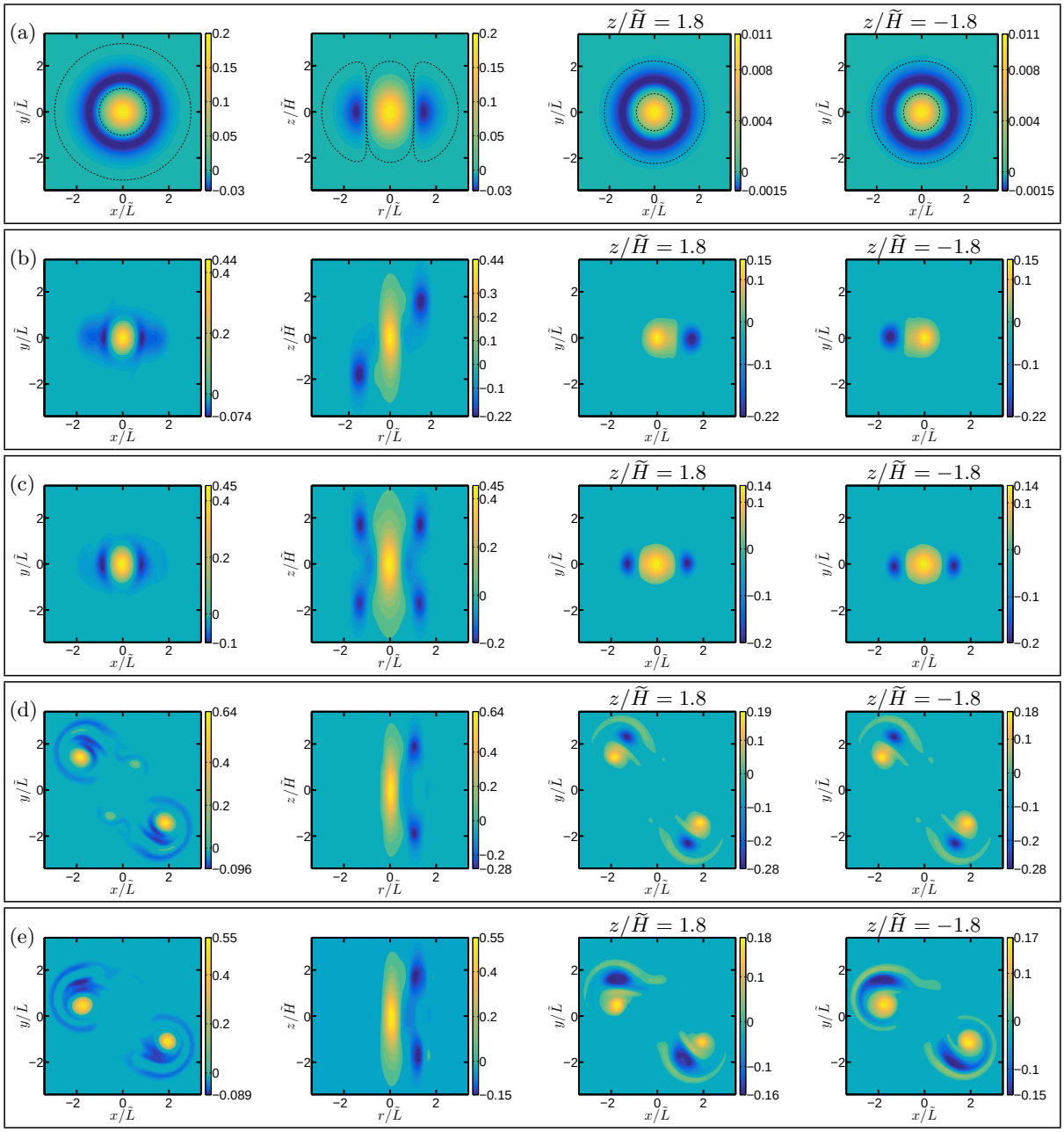

Figure 3.13: (Colour online) Vertical vorticity ω for a group 4 vortex, which can split into two tripoles that move radially away from the initial equilibrium. $\widetilde{Ro} = 0.2$, $\widetilde{Bu} = 0.1$, and $f/\bar{N} = 0.1$. (b) to (e) show four of the possible final equilibria ω_j to which the vortex can evolve. Panel (a) is as in panel (a) of figure 3.11, but shows the Gaussian equilibrium vortex $\tilde{\omega}$ here. Panels (b) and (c) are as in panel (b) of figure 3.11, but show two possible non-splitting equilibria ω_j for this case. On the other hand, the "final equilibria" in (d) and (e) result from splitting. Here, for the cases for which the vortex splits into tripoles, the tripoles' cores are on the $z = 0$ plane, and their satellites are on the $z =$ constant planes above and below $z = 0$, so (d) and (e)'s first figures show the $z = 0$ plane and their third and fourth figures, the satellites' planes. The second figure shows one of the tripoles in $(r - z)$ plane. The perturbation amplitude(s) for panel (b) is $A_{IC,A3} = 10^{-4}$; for panel (c) is $A_{IC,A2} = 10^{-4}$; for panel (d) are $A_{IC,S2} = 10^{-4}$, and $A_{IC,N} = 10^{-4.5}$; and for panel (e) are $A_{IC,S4} = 10^{-4}$, and $A_{IC,N} = 10^{-4.5}$, i.e., see table 3.4.

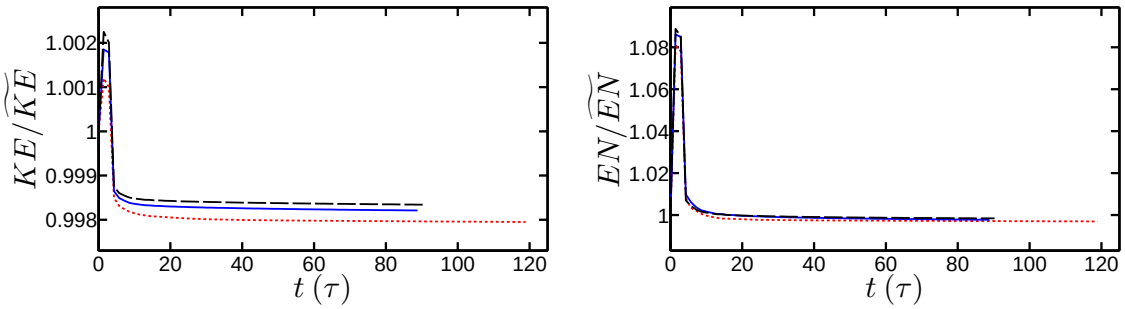

Figure 3.14: (Colour online) Kinetic energy $KE/\widetilde{KE}$, and enstrophy $EN/\widetilde{EN}$, for different perturbations of a group 5 vortex (i.e., $N_c^2 < 0$), showing that for all the cases demonstrated, the vortex quickly reaches quasi-steady state. $\widetilde{Ro} = -0.3$, and $\widetilde{Bu} = 0.17$. Note also that $L/\tilde{L}$, $H/\tilde{H}$, Ro, and Bu shown in figures 3.1, 3.4, 3.8, and 3.10 are not shown here, as their definitions do not lend themselves to the final equilibria of group 5 (as shown in figures 3.15 and 3.16). The black long-dashed lines have perturbation amplitude of $A_{IC,A4} = 10^{-4}$; the short-dashed lines (red, in colour) have perturbation amplitude of $A_{IC,N} = 10^{-4.5}$; and the solid lines (blue, in colour) have perturbation amplitudes of $A_{IC,A4} = 10^{-4}$, and $A_{IC,N} = 10^{-4.5}$. In this case again, at the quasi-steady state the fractional changes of the shown quantities are smaller than ~ 0.004.

$\Gamma_{A4} \simeq 0.03$ and $\Gamma_{S2} \simeq 0.02$ shown to be much smaller). It should be noted that groups 3a and 3b cases also have large Γ_{S4} enstrophies, but smaller than the values of the Γ_{S4} for the cases in group 5. The kinetic energy $KE/\widetilde{KE}$, and enstrophy $EN/\widetilde{EN}$ saturation for different perturbations (see table 3.5) of a group 5 vortex are in figure 3.14, indicating how the perturbations grow quickly, but then saturate quickly as the vortex attains its quasi-steady state. Two group 5 vortices are shown in figures 3.15 and 3.16.

Parameter map of stability

The parameter map of stability in the $Ro - Bu$ space is shown in figure 3.17. Gaussian anticyclones do not exist with $Ro < -0.5$ (see chapter 2, §2.2). The region to the lower left of the thick dashed black curve corresponds to equilibrium Gaussian vortices for which $N_c^2 < 0$ (i.e., the vortices of group 5), with $\widetilde{Bu} = -\widetilde{Ro}(1 + \widetilde{Ro})$ on the thick dashed black curve (see (3.2)). Almost all final equilibria's cores are on the vortex's midplane, except for group 5's final equilibria, with one core above vortex midplane and the second core below it.

Figure 3.17(a) shows the regions of the parameter space, where the most unstable eigenmodes have slow, or fast growth rates (i.e., $\sigma < 0.02\,\tau^{-1}$, or $\sigma > 0.02\,\tau^{-1}$). Vortices have slow growth rates in the unlabeled region (e.g., see chapter 2, §2.4), and the other four regions, indicated using large labels (red, in colour) have growth rates that are fast (where $\sigma > 0.02\,\tau^{-1}$) such that the vortices quickly evolve from their initial states. The labels show symmetries of the regions' most unstable eigenmodes, with the region labeled A having fastest-growing eigenmodes that are anti-symmetric in z with an azimuthal wave number m

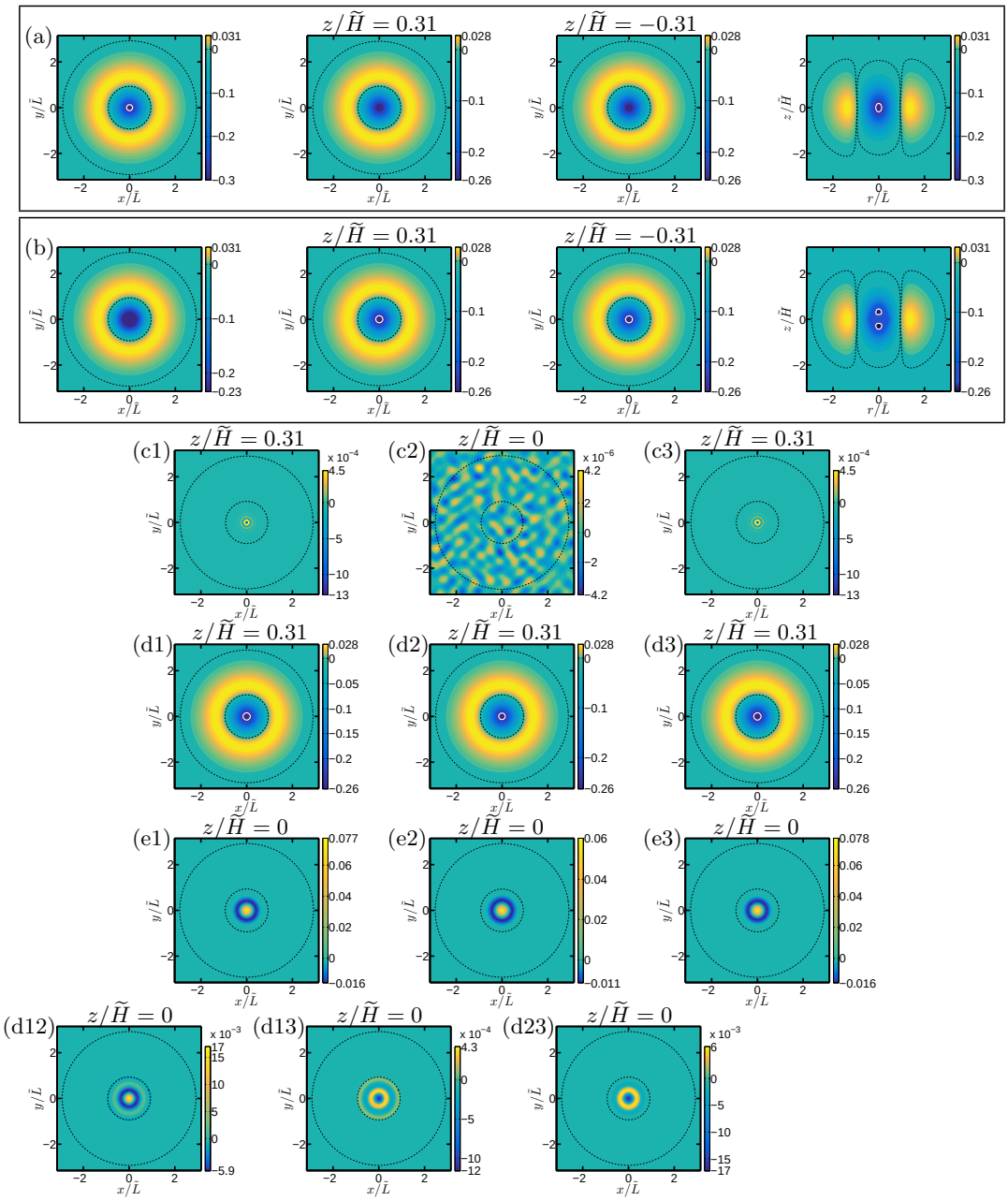

Figure 3.15: (Colour online) The initial equilibrium $\tilde{\omega}$, the average final equilibrium $\hat{\omega}$, and the numerical quantities, describing vortex evolution for the vortices of group 5, where the core splits vertically, into two cores radially-aligned at the initial vortex's center. For the vortex in this figure, $\widetilde{Ro} = -0.3$, $\widetilde{Bu} = 0.17$, and $f/\bar{N} = 0.1$. Here, once again, the first figure of (a) and (b) shows the vortex midplane (meaning $z = 0$), but the second and third figures are on the planes of the cores of the $\hat{\omega}$. Similarly, (d1) to (d3) show the time-averaged final equilibria $\langle\omega_j\rangle$ on the upper core's plane (the second and third figures of (b) show that the upper and lower cores are in fact similar). The white solid line(s) in (a), (b), and (d1) to (d3) are for $0.94\,\min[\omega]$ iso-contour(s) showing the initial core splits into two similar pieces. The fourth figure of (a) and (b) shows the vortex on the $(r-z)$ plane. The black dashed lines indicate the boundaries of the core and shield. Panels (c1) to (c3), (e1) to (e3), and (d12) to (d23) have the same interpretation, as those in figure 3.11. For all $(x-y)$ figures, their headers indicate the plane of the figure. The perturbation amplitude(s) for panel (c1) is $A_{IC,A4} = 10^{-4}$; for panel (c2) is $A_{IC,N} = 10^{-4}$; and for panel (c3) are $A_{IC,A4} = 10^{-4}$, and $A_{IC,N} = 10^{-4.5}$. For these three cases, (d1) to (d3) show that the time-averaged final equilibria $\langle\omega_j\rangle$ resemble each other closely and panel (b)'s $\hat{\omega}$. The differences $\langle\omega_j\rangle - \tilde{\omega}$ in (e1) to (e3) have fractional magnitudes of $\simeq 0.08/0.3$ (but consistent with the initial-value calculations in table 3.5 showing small D_c, and smaller D_s, their magnitude is large only close to the initial vortex's center). (d12) to (d23) show that the differences $\langle\omega_{j_1}\rangle - \langle\omega_{j_2}\rangle$, $j_1 \neq j_2$ are small, with fractional magnitudes $\simeq 0.02/0.3$.

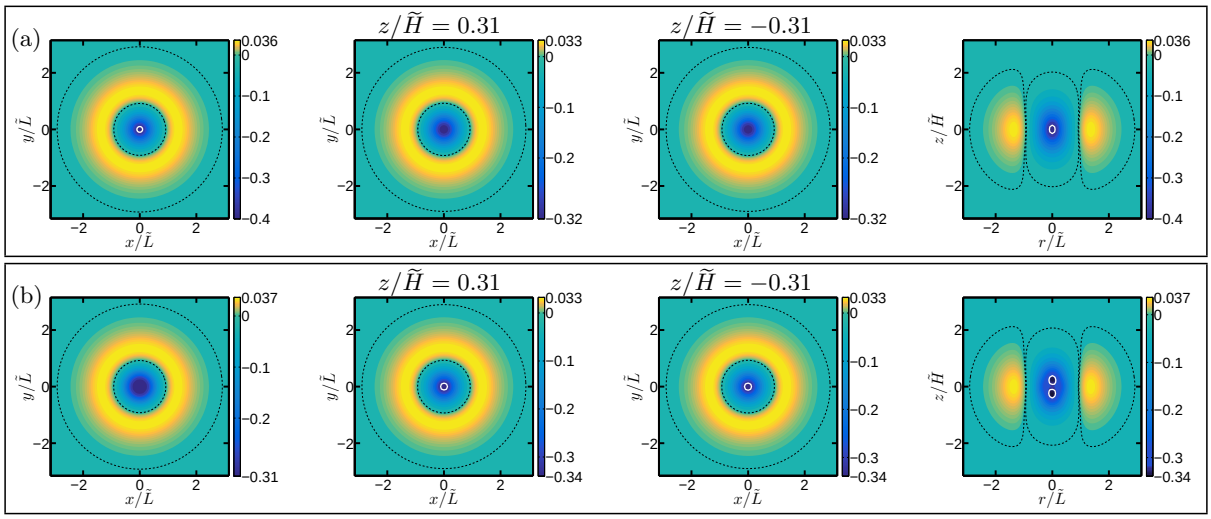

Figure 3.16: (Colour online) Similar to figure 3.15's panels (a) and (b), but for a group 5 vortex, with $\widetilde{Ro} = -0.4$, $\widetilde{Bu} = 0.2$, and $f/\bar{N} = 0.1$. Figure 3.15's panel (b) and the average final equilibrium that is shown here have one core above $z = 0$, and another core below it (the initial-value calculations for this group 5 case are in table 3.5).

of 1, 2, 3 or 4. Figure 3.17(b) shows the Gaussian equilibria in the $Ro - Bu$ parameter space and their vortex group (see previous subsection), with the vortices having final equilibria that can belong to the six different vortex groups 1, 2, 3a, 3b, 4, and 5.

Note that while for the vortices of groups 1 and 2, the growth rates are in fact very fast (as demonstrated in the '$\sigma\,(\tau^{-1})$' column of tables 3.1 and 3.2), their final equilibria remain close to their Gaussian equilibrium, and obviously linear stability cannot be implemented to explain the long lifetimes of the cyclonic vortices that are frequently observed in the ocean (the vortices of groups 1 and 2 are largely cyclonic). So one possible explanation for the robustness of the cyclones is therefore that, despite having fast growth rates, for these vortices the perturbations quickly saturate such that they remain close to their initial state, and the vortices are linearly unstable, but finite-amplitude stable. In §3.2 it was demonstrated that, for the vortices remaining close to their Gaussian equilibrium there should be $D_c \lesssim 0.1$ and $D_s \lesssim 0.4$, or $F_c \lesssim 0.1$ and $F_s \lesssim 0.4$, for the vortex core and shield. Thus, the cyclones in a large region of the parameter space (groups 1 and 2) have final equilibria that remain close to their Gaussian equilibrium (see figure 3.17(b)). Usually for these vortices the fastest-growing eigenmode symmetry and the difference flow dominant symmetry are the same (i.e., A1 symmetry for group 1 vortices and S2 symmetry for group 2 vortices). However, we find that there are several vortices (i.e., table 3.1's first four cases) with an S2 fastest growing eigenmode and an A1 dominant symmetry difference flow. Our calculations show that these cases' final equilibria are always within same attracting basins regardless of the initial conditions. These vortices are shown with symbols '1' within hollow circles in figure 3.17(b). Also our calculations show there is a vortex in group 2 with A1 fastest growing eigenmode and S2 difference flow dominant symmetry, as demonstrated by

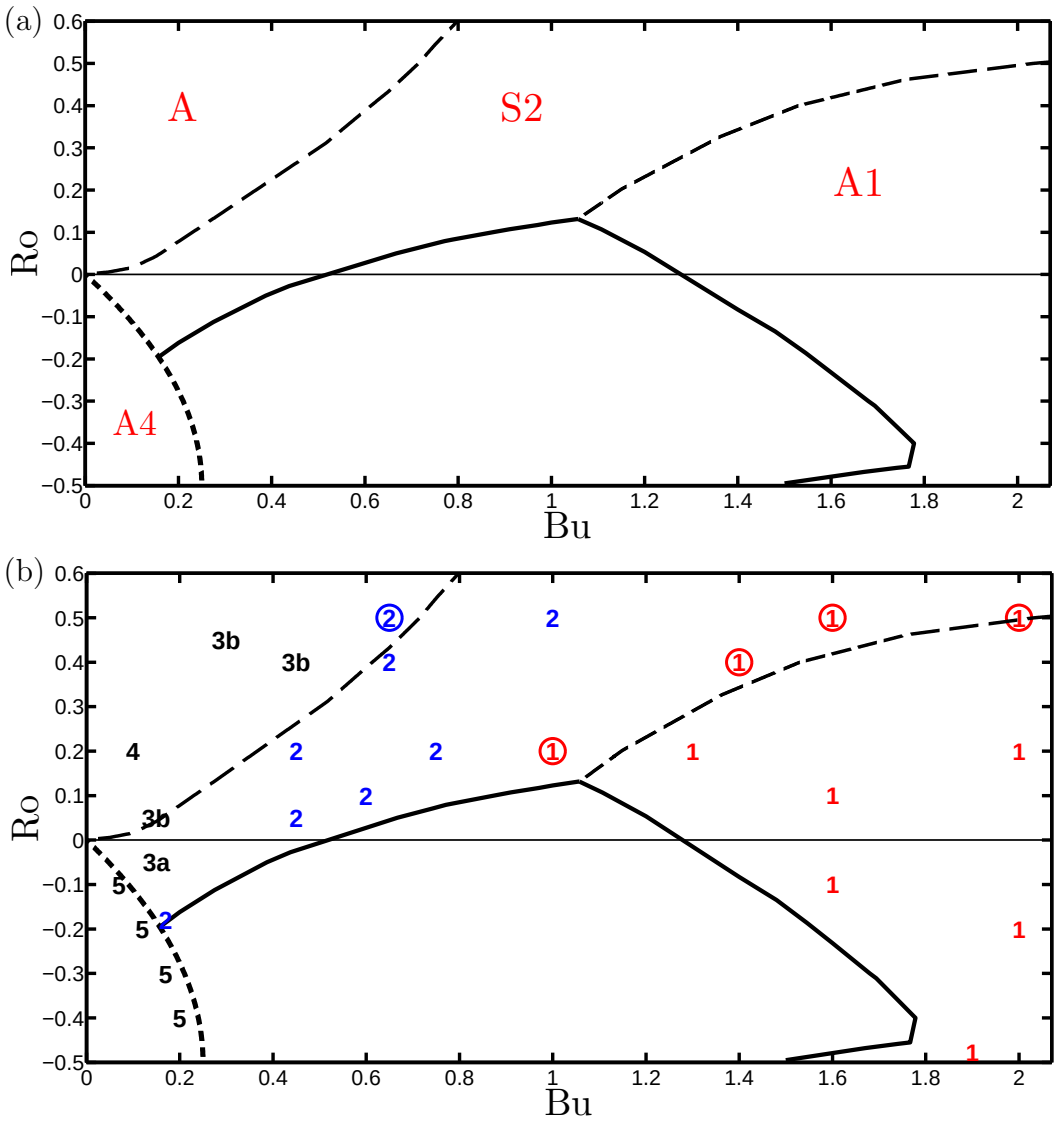

Figure 3.17: (Colour online) Parameter map of stability of the vortices and their equilibria in $Ro - Bu$ space. No equilibrium Gaussian vortices exist with $Ro < -0.5$. The thick black dashed line in the lower left corner of (a) and (b), indicates the locus over which $N_c^2 = 0$, or, $\widetilde{Bu} = -\widetilde{Ro}(1 + \widetilde{Ro})$, with $N_c^2 < 0$ for the points to its left (for their initial and final equilibria), which have small Ro and Bu. Panel (a): Regions of parameter space with fast, and slow growth rates (i.e., $\sigma > 0.02\,\tau^{-1}$, and $\sigma < 0.02\,\tau^{-1}$) and various eigenmode symmetries. The thick solid line indicates the iso-surface, where σ of the fastest-growing eigenmode is $0.02\tau^{-1}$. The region bounded by this iso-surface, the thick black dashed curve on the lower left corner (i.e., where $N_c^2 = 0$), and the bottom of the figure has $\sigma < 0.02\,\tau^{-1}$ (for more details see figures 2.8 and 2.13 of chapter 2). Outside this region (i.e., $\sigma > 0.02\tau^{-1}$), at the regions marked by the large labels (red, in colour) vortices evolve quickly from their initial state with the labels showing symmetries of each region's most unstable eigenmode. The fastest growing eigenmodes in the region labeled A are anti-symmetric in z and have azimuthal wave numbers of 1, 2, 3 or 4. Tables 3.1 to 3.5 show initial-value calculations for the regions' sample points. Panel (b): The labels show the Gaussian vortices and the groups their final equilibria belong to. For group 1 and group 2 vortices shown using symbols '1' (red, in colour) and '2' (blue, in colour), the difference between the initial and final equilibria has A1 and S2 dominant symmetry. The cases shown with symbols '1' in hollow circles (red, in colour) have dominant symmetry and fastest growing eigenmode of A1 and S2, and the case shown with symbol '2' in a hollow circle (blue, in colour) has dominant symmetry and fastest growing eigenmode of S2 and A1. For groups 3a and 3b the difference between the initial and final equilibria has no dominant symmetry. On the other hand, for the point $\widetilde{Ro} = 0.2$, $\widetilde{Bu} = 0.1$ shown with the '4', there is splitting. The cases with $N_c^2 < 0$ are shown with the '5's.

table 3.2's first case, and shown with symbol '2' in a hollow circle in figure 3.17(b)'s upper left corner. Figure 3.18 shows the basins of attraction for the final equilibria in this study. The basins are drawn for the final equilibria using boxes, that are to "guide the eye". Groups 1 and 2 have attracting basins, that are very close to their initial states (consistent with the above arguments), and for groups 3a, 3b, and 4, the attracting basins shown (which do not include the cases, where imposition of perturbations caused the vortex to split) are clearly far from their initial equilibrium. For the cases in figure 3.18(b), that is for groups 2, 3a, 3b, and 4, Ro generally increases in the final equilibria, relative to initial equilibria. For larger $\widetilde{Ro}$, the attracting basins become significantly larger for all vortices, and analogously for $\widetilde{Bu}$ more different than $Bu = 1$. For group 1 vortices, Ro evolves towards $Ro = 0$. For all cases Bu evolves towards unity.

For a group 3b vortex with initial conditions that are *purely symmetric*, the values of the symmetric and anti-symmetric enstrophies are shown in figure 3.19. The initially-minuscule anti-symmetric enstrophy grows with an exponential rate, saturating at constant values thereafter. Note that the flow symmetric and anti-symmetric enstrophies clearly remain constant (see figure 3.19(b)) with comparable magnitudes, but with the symmetric flow having enstrophies ($EN/\widetilde{EN} \sim 0.1$) one tenth smaller than the anti-symmetric part's enstrophy values ($EN/\widetilde{EN} \sim 1$).

For most cases in tables 3.1 to 3.5, we have used two sets of initial conditions. To show that the final equilibria within different groups and their attracting basins are independent of our choice for the number of the initial condition sets, we have further examined cases with more than two sets of initial conditions, that is e.g., for the case $\widetilde{Ro} = 0.4$, $\widetilde{Bu} = 1.4$ with 5 initial condition sets, or the case $\widetilde{Ro} = 0.2$, $\widetilde{Bu} = 1.3$ with 3 initial condition sets. Our calculations show that the sizes of the attracting basins for these cases remain consistent with the other cases in the same vortex group (i.e., see figure 3.18, where these two vortices' attracting basins have similar attributes as the other vortices' attracting basins in the same vortex group). The number of total simulation turnaround times t_f for the cases for different vortex group are in tables 1 to 5's captions. Furthermore, our calculations show that $EN'_{\infty,j}$ values are approximately-steady for groups 1, 2, 3a, 3b, and 5. Different vortex groups in this study and the properties are in table 3.7. For groups 1 and 2, it is shown that the initial and final equilibria remain similar, and are nearly axisymmetric. Only groups 3a, 3b, and 4 have final equilibria not similar to their initial equilibrium. Also for the anticyclones in group 5, the initial and final equilibria remain similar within their cores, and shields. However we note that their core splits vertically into two radially-aligned cores.

Figure 3.20 shows the vorticity profile of the initial equilibrium $\tilde{\omega}(z)$ and the average final equilibrium $\hat{\omega}(z)$ for a group 5 case (i.e., that is the equilibrium vortex in figure 3.16) on $r = 0$. Note that the profiles are vertically symmetric, with hardly-detectable anti-symmetric parts. The final equilibrium's profile shows two cores (where the profiles have maximum values) and at other z values, the initial and final equilibria remain similar to each other. Note also that we have not examined further group 5 cases with smaller Ro or Bu values, because of their very fast growth rates, which require using much smaller time step sizes and therefore can be computationally very expensive.

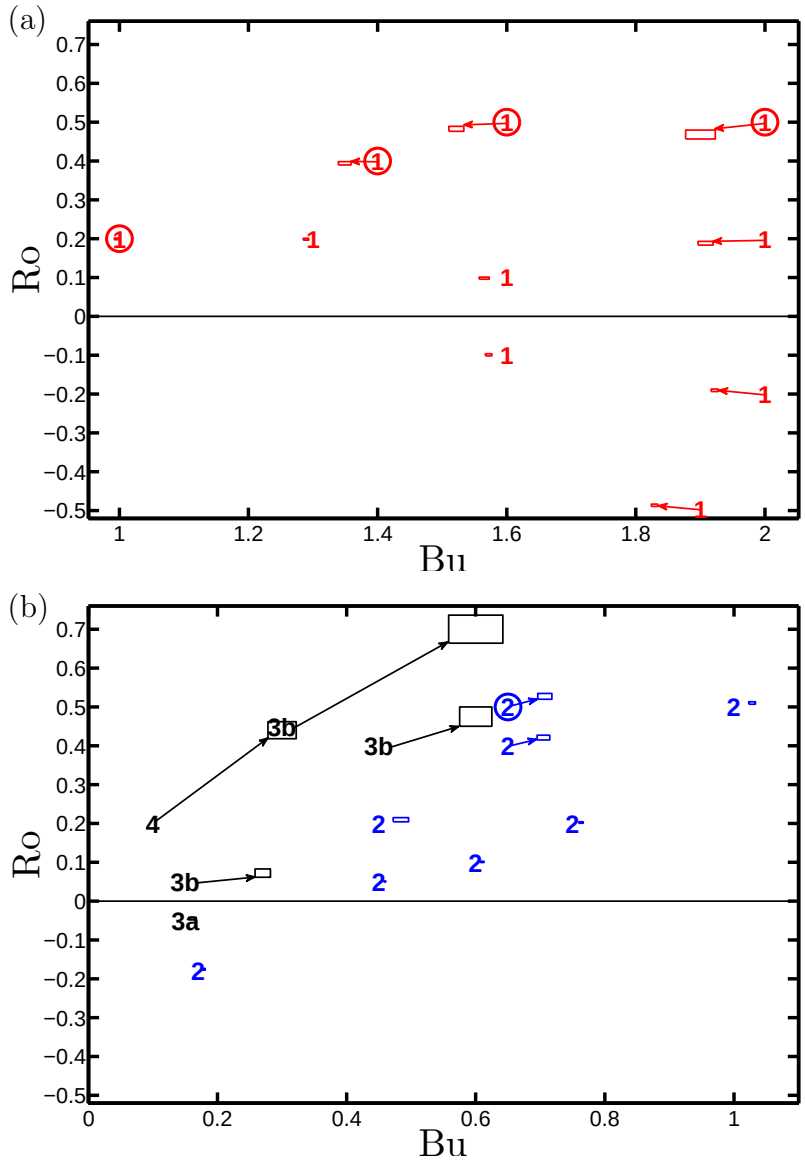

Figure 3.18: (Colour online) Basins of attraction for all the vortices in this study. Panel (a): The close up of the right side ($Bu \gtrsim 1$) of figure 3.17(b), showing the basins of attraction for the vortices of group 1. For each case, the initial equilibrium is denoted by a label '1' (red, in colour), and the attracting basins by the rectangles (red, in colour). The arrows denote the connection between the attracting basins, and the corresponding initial equilibria. For the four cases with no arrows the initial and final equilibria are very close. Panel (b): The close up of the left side ($Bu \lesssim 1$) of figure 3.17(b), showing the basins of attraction for the vortices of group 2; and groups 3a, 3b and 4 (which do not include the cases, where imposition of perturbations caused the vortex to split), where the initial equilibria are, respectively, denoted using labels '2' (blue, in colour); and black labels '3a', '3b' and '4'. The basins of attraction in these cases are shown by the rectangles (group 2's cases blue, in colour) (the boxes are to "guide the eye" and are calculated for the final equilibria, by the ΔRo, ΔBu, δRo_j, and δBu_j values shown in tables 3.1 to 3.4 for groups 1 to 4). For the seven panel (b) cases with no arrows the initial and final equilibria are very close. For cases in panel (b), Ro generally increases in final equilibria, relative to initial equilibria (i.e., all the arrows point upwards). In both panels, for larger $\widetilde{Ro}$, the attracting basins become significantly larger, and analogously for $\widetilde{Bu}$ more different than $Bu = 1$. For cases in panel (a), Ro evolves towards $Ro = 0$ [i.e., for $\widetilde{Ro} > 0$ ($\widetilde{Ro} < 0$) cases, the attracting basins' Ro values are smaller (larger) than initial unperturbed equilibrium's Ro]. For all cases Bu evolves towards unity [i.e., for $\widetilde{Bu} > 1$ ($\widetilde{Bu} < 1$) cases, the attractions basins' Bu values are smaller (larger) than initial unperturbed equilibrium's Bu, and do not pass $Bu = 1$].

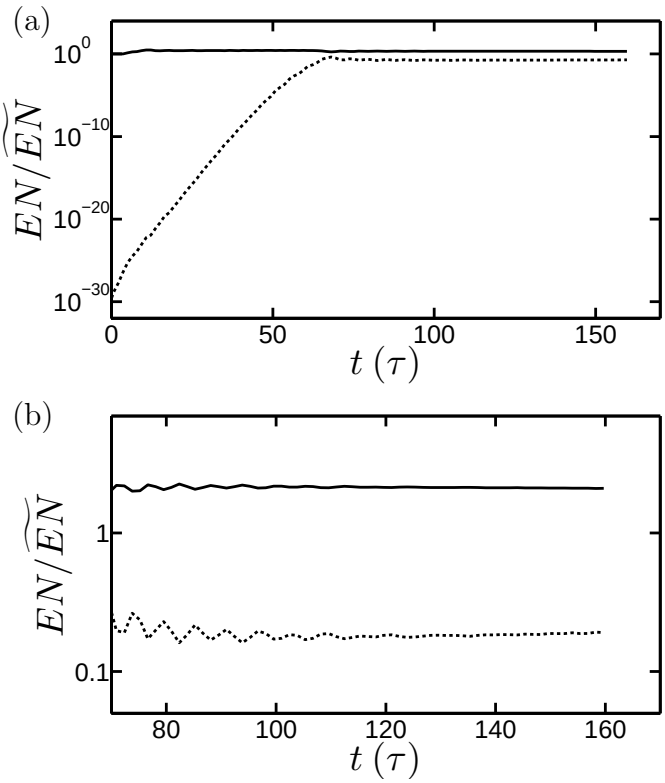

Figure 3.19: Symmetric and anti-symmetric enstrophies for a group 3b vortex with initial conditions that are purely symmetric shown, respectively, with the black solid and dashed lines. The example vortex equilibrium has $\widetilde{Ro} = 0.45$, $\widetilde{Bu} = 0.3$, and $f/\bar{N} = 0.1$, and the perturbation amplitude is $A_{IC,S2} = 10^{-3.5}$ (we note that the vortex equilibrium and the perturbation are purely-symmetric). Panel (a) is in logarithmic scale and shows that the anti-symmetric enstrophy that is initially-minuscule grows with an exponential rate from round-off, which afterwards, saturates at a constant value (i.e., for $t \gtrsim 80\tau$). Panel (b) shows that at later times, the symmetric and anti-symmetric enstrophies are in fact constant, with comparable magnitudes (but with the symmetric part having magnitudes one tenth smaller than the anti-symmetric enstrophy).

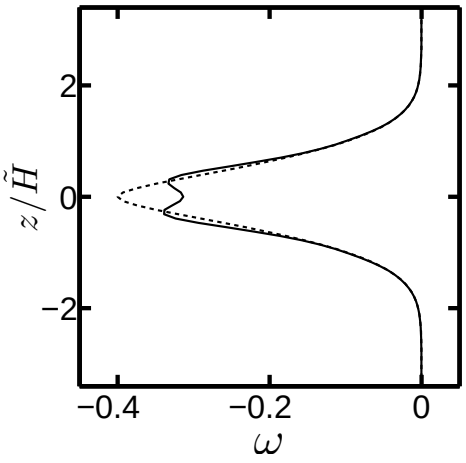

Figure 3.20: Vorticity profile for the initial equilibrium $\tilde{\omega}(z)$ and the average final equilibrium $\hat{\omega}(z)$ of the case in figure 3.16, on the line where $r = 0$. The dashed and solid curves show the initial and final equilibria, respectively. Note that, the profiles are vertically symmetric, and the maximum values for the final profile are at the position of the cores. At the other z values, the initial and final equilibria remain similar to each other.

Group	**Similar?**		**Gaussian?**			**Symm**	**Description**
	core	shield	core	shield	vortex		
1	✓	✓	✓	✓	G-L	A1	–
2	✓	I	✓	I	G-L	S2	–
3a	–	–	✓	–	N-G-L	–	two midplane satellites
3b	–	–	✓	–	N-G-L	–	$z = \pm$ constant satellites
4	–	–	–	–	N-G-L	–	the vortex can split
5	✓	✓	✓	✓	G-L	S4	$N_c^2 < 0$

Table 3.7: Different vortex groups in this study and their properties, where 'Similar?' shows if the core and shield of the initial and final equilibria remain similar, 'Gaussian?' shows if the core and shield of the initial and final equilibria remain Gaussian-like 'G-L', or are Non-Gaussian-like 'N-G-L'. 'I' is for the vortex families that have intermediate $D_s \lesssim 0.4$ (see the text describing these equilibria). 'Symmetry' shows the dominant symmetries of the difference flows for different vortex groups.

3.4 A simplified flow representation, and the Landau equation

Despite the fact that nonlinear vortex evolution is in most cases arduous to describe throughly, quantitative measures are often used to outline vortex evolution, as no analytical solution exist in such cases to describe the vortex evolution. For the vortices here, we utilize the enstrophy measures d_j, D_c, D_s, F_c, F_s, and the symmetry enstrophy measures, to identify the final equilibrium for each examined initial state, and show that there are six different vortex groups with different characteristics.

For the vortex groups with a dominant symmetry, here it is shown that the vortex evolution as well as the characteristics of the flow are represented entirely by the unperturbed equilibrium, its dominant symmetry eigenmode, and a complex coefficient $A(t)$ that is calculated numerically by minimizing the remainder's L2 norm; and analytically by the Landau equation, where the latter can provide closed-form solutions. For the cases for which the above representation holds, we demonstrate that the remainders' L2 norm decrease substantially (or remain small), as the numerical $A(t)$ values increase, and plateau for the flows that have reached their quasi-steady equilibrium state. We also show here that the $A(t)$ values calculated numerically and analytically have close values, as do the flow representations. Furthermore, it is illustrated that the cases that have small values of $|A(t)|$ – are the same as the group 1, and group 2 cases identified above, so that almost all vortices in the parameter space have similar final and *unperturbed* Gaussian equilibria.

Our previous description of the flow dynamics, given by (3.15) is simplified here, for the vortices of the groups that have dominant symmetry difference flows as

$$\boldsymbol{g}(\boldsymbol{x},t) = \tilde{\boldsymbol{g}}(r,z) + \frac{1}{2}\big[\boldsymbol{g}_{eig}(\boldsymbol{x})A(t) + \boldsymbol{g}^{\dagger}_{eig}(\boldsymbol{x})A^{\dagger}(t)\big] + \boldsymbol{R}'(\boldsymbol{x},t), \tag{3.21}$$

where $\tilde{\boldsymbol{g}}(r,z)$ shows the real unperturbed equilibrium, $\boldsymbol{g}_{eig}(\boldsymbol{x})$ represents the complex dominant symmetry eigenfunction, $A(t)$ is a complex valued coefficient, the superscript † denotes complex conjugate (note that $\boldsymbol{g}^{\dagger}_{eig}(\boldsymbol{x})$ is an eigenfunction also), and $\boldsymbol{R}'(\boldsymbol{x},t)$ denotes the remainder here (i.e., different than $\boldsymbol{R}(\boldsymbol{x},t)$ in (3.15)). For (3.21), the vertical vorticity representation is

$$\omega(\boldsymbol{x},t) = \tilde{\omega}(r,z) + \frac{1}{2}\big[\omega_{eig}(\boldsymbol{x})A(t) + \omega^{\dagger}_{eig}(\boldsymbol{x})A^{\dagger}(t)\big] + \omega_{R'}(\boldsymbol{x},t). \tag{3.22}$$

The way $\omega_{R'}$ and A are found, is by first calculating $\omega - \tilde{\omega}$, and then finding value of A that minimizes $\omega_{R'}$'s L2 norm. This process is carried out for each time instance to find $A(t)$ values. Furthermore, for an analytical solution $A_{\mathcal{L}}(t)$, we can use the Landau equation [Landau 1944]

$$\frac{\partial A_{\mathcal{L}}(t)}{\partial t} = \lambda A_{\mathcal{L}}(t) - \Lambda A_{\mathcal{L}}(t)|A_{\mathcal{L}}(t)|^2, \tag{3.23}$$

where $\lambda \equiv \sigma - imc$ shows the dominant symmetry eigenvalue (σ is the real growth rate, and c is the real azimuthal phase speed), and Λ shows the complex Landau coefficient. Multiplying

(3.23) by $A^{\dagger}_{\mathcal{L}}(t)$, and (3.23)'s complex conjugate by $A_{\mathcal{L}}(t)$, adding the resulting equations, and dividing by $2|A_{\mathcal{L}}(t)|$, we obtain here for $|A_{\mathcal{L}}(t)|$, the equation

$$\frac{\partial |A_{\mathcal{L}}(t)|}{\partial t} = \sigma |A_{\mathcal{L}}(t)| - \Re[\Lambda] |A_{\mathcal{L}}(t)|^3, \tag{3.24}$$

where $\Re[\Lambda]$ denotes the Landau coefficient Λ's real part. It can easily be shown that (3.24)'s solution is

$$|A_{\mathcal{L}}(t)| = \frac{A_{IC,\mathcal{L}}}{\sqrt{\frac{\Re[\Lambda]}{\sigma}|A_{IC,\mathcal{L}}|^2 + \left(1 - \frac{\Re[\Lambda]}{\sigma}|A_{IC,\mathcal{L}}|^2\right)\exp\left[-2\sigma t\right]}}, \tag{3.25}$$

where $A_{IC,\mathcal{L}} \equiv |A_{\mathcal{L}}(t=0)|$ is the initial $A_{\mathcal{L}}$'s amplitude. $A_{IC,\mathcal{L}}$ is calculated by finding $|A(t)|$ and $|A_{\mathcal{L}}(t)|$'s difference during linear growth stage (i.e., times when the differences between $|A(t)|$ and a linear fit are smaller than 10 percent), and minimizing its values. The Landau coefficient's real part $\Re[\Lambda]$ is calculated, *after* flow reaches quasi-steady state, by assuming $|A_{\mathcal{L}}(t \to \infty)| = \langle |A(t)| \rangle$ and using $\Re[\Lambda] = \sigma / |A_{\mathcal{L}}(t \to \infty)|^2$. The equation

$$\omega(\boldsymbol{x}, t) = \tilde{\omega}(r, z) + \frac{1}{2}\left[\omega_{eig}(\boldsymbol{x}) A(t) + \omega^{\dagger}_{eig}(\boldsymbol{x}) A^{\dagger}(t)\right], \tag{3.26}$$

where ω_{eig} shows the fastest growing dominant symmetry eigenmode's vertical vorticity, presents the simplified representation discussed above, and we show here that it is a good representation for the vortices of group 1 (i.e., for which ω_{eig} is the vortex's fastest growing eigenmode with A1 symmetry). Figure 3.21 shows that for an example group 1 vortex (the group 1 case shown in figure 3.2's panel (b)), the $\hat{\omega} - \tilde{\omega}$ and $\langle A \rangle \omega_{eig}$ representations of the flow are very close to each other, and therefore (3.26) presents an almost self-contained solution. For the case above, figure 3.22's top and bottom panels show, respectively, the remainder norms and $|A(t)|$ values. The remainder $\omega_{R'}$s' norms decrease, or remain small, and $|A(t)|$ values increase, such that at later times the remainder norms obtain small values, and $|A(t)|$ values plateau. The thick gray line in figure 3.22's bottom panel shows the $|A_{\mathcal{L}}(t)|$. At the late times, the values of $|A|$ and $|A_{\mathcal{L}}|$ are close, showing that the Landau equation holds in this case. The same results as above hold for the vortices of group 2 (i.e., with ω_{eig} here being the vortex's fastest growing eigenmode with S2 symmetry). Figure 3.23 shows that for an example group 2 vortex (the group 2 case presented in figure 3.5's panel (b)), the two representations of the flow are again very close and again (3.26) is almost self-contained. The remainder norms, $|A(t)|$, and $|A_{\mathcal{L}}(t)|$ for this case are shown in figure 3.24, where the remainder norms decrease, or remain small, and the numerically computed A's absolute values increase, and again at quasi-steady state the norms obtain small values, and $|A(t)|$ values plateau. The figure's bottom panel shows that the Landau equation holds in this case. For vortices of groups 3a, 3b, 4, and 5, a (3.26) representation clearly does not hold (i.e., the remainder norm, we find, is clearly large in such cases).

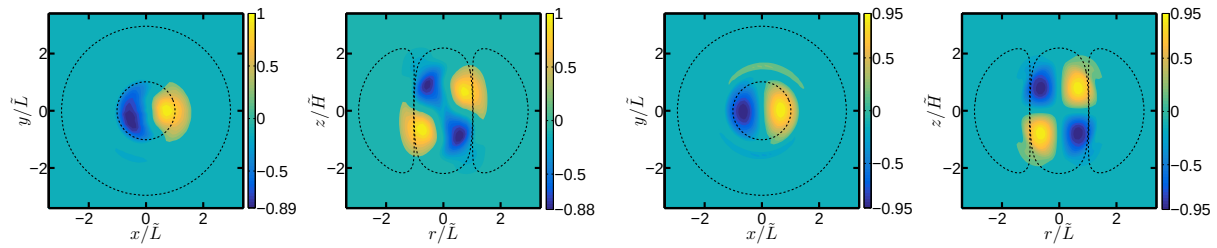

Figure 3.21: (Colour online) Vertical vorticity difference $\hat{\omega} - \tilde{\omega}$ (for the group 1 case shown in figure 3.2's panel (b)), and $\langle A \rangle \, \omega_{eig}$, normalized (i.e., via dividing by $|\hat{\omega} - \tilde{\omega}|$'s maximum), so the maximum value of the $|\hat{\omega} - \tilde{\omega}|$ is 1. The representations are very close to each other, showing that $\omega = \tilde{\omega} + \omega_{eig} A$ is an almost self-contained solution in this case (the remainder norm and $|A(t)|$ for this case are shown in figure 3.22). The broken lines denote the boundaries of the core and shield of the unperturbed Gaussian equilibrium, i.e., $\tilde{\omega}$. The left two panels show $\hat{\omega} - \tilde{\omega}$ and the right two show $\langle A \rangle \, \omega_{eig}$. The first and third panels of the figure show the flow in the x-y plane, that has a fixed-z (i.e., the z, where $|\hat{\omega} - \tilde{\omega}|$ obtains its maximum value). The second and fourth panels show each of the representations in the r-z plane for a fixed azimuthal angle ϕ. In all cases, ϕ is chosen so that it is the angle at which $\hat{\omega} - \tilde{\omega}$ of the flow obtains its maximum value.

Assuming that the flow goes to quasi-steady state, the Landau equation (3.24)'s steady state solution is given by

$$|A_{\mathcal{L}}(t \to \infty)| = \sqrt{\frac{\sigma}{\Re[\Lambda]}}, \tag{3.27}$$

where $\Re[\Lambda]$ denotes the Landau coefficient Λ's real part. For the vortices for which (3.26), and the Landau equation hold, the final and *unperturbed* Gaussian equilibria are similar, only in the cases that the $\Re[\Lambda]/\sigma$ is large, and otherwise, they can be different. We found, to our surprise, that the cases with large $\Re[\Lambda]/\sigma$ are the same as group 1, and group 2 cases examined here (i.e., $110 \lesssim \Re[\Lambda]/\sigma$ for group 1 cases, and $21 \lesssim \Re[\Lambda]/\sigma \lesssim 100$ for group 2 cases). Therefore, almost all vortices have similar final and unperturbed Gaussian equilibria. This is in agreement with group 1, and group 2 having Gaussian-like final equilibria (see §3.3). It should be noted here that we could not calculate the Landau coefficient Λ *a priori*. A Landau coefficient can be calculated, only after flow reaches quasi-steady state.

3.5 Discussion and summary

The 3D Gaussian vortices, and their evolution, along with their finite-amplitude stability have been examined here; with the vortex parameters including the Rossby number, Ro, and Burger number, Bu, over a relevant set of values that are found by examining observations ($-0.5 < Ro < 0.5$ and $0.07 < Bu < 2$). For each (Ro, Bu), and its different perturbations, the evolution of the unstable flow is examined numerically using an initial-value solver.

The results of the stability analysis are summarized in the $Ro - Bu$ parameter map (figure 2.8). The results of chapter 2 show that the cyclonic neutrally-stable vortices are in

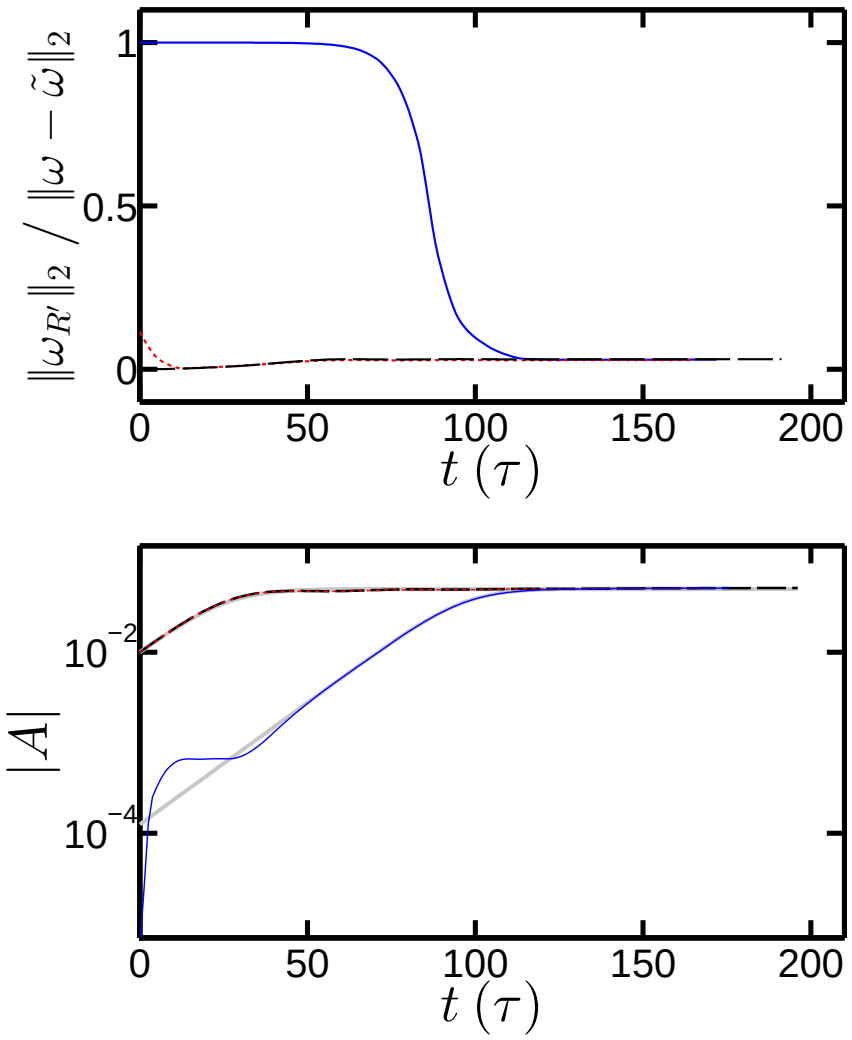

Figure 3.22: (Colour online) The remainder norm $\|\omega_{R'}\|_2/\|\omega-\tilde{\omega}\|_2$ and the $|A(t)|$ for the case shown in figure 3.21. The remainder norms decrease towards smaller values, and plateau (or remain small), as $|A(t)|$ values increase, and plateau. At quasi-steady state, the flow has remainder norms that are small, i.e. $\|\omega_{R'}\|_2/\|\omega-\tilde{\omega}\|_2 \lesssim 0.1$. Different line styles (and colours, in colour version) are for different perturbations, as shown in figure 3.1's caption (i.e., that is the perturbation amplitude(s) for the black long-dashed lines is $A_{IC,A1} = 10^{-2}$; for the short-dashed lines (red, in colour) are $A_{IC,A1} = 10^{-2}$, and $A_{IC,N} = 10^{-2.5}$; and for the solid lines (blue, in colour) are $A_{IC,S2} = 10^{-2}$, and $A_{IC,N} = 10^{-2.5}$) (the top panel's black long-dashed line, and short-dashed line (red, in colour) are very close, due to having very close values). For a case starting with the initial conditions of the Gaussian equilibrium and dominant symmetry eigenmode only (i.e., the black long-dashed line here); initially $\|\omega_{R'}\|_2(t=0) = 0$. The thin lines in the bottom panel demonstrate the $|A(t)|$, and the thick gray lines are for the $|A_{\mathcal{L}}(t)|$, given by (3.25). At the late times, the values of $|A|$ and $|A_{\mathcal{L}}|$ are close, showing that the Landau equation holds in this case (the bottom panel's black long-dashed line, short-dashed line (red, in colour), and their corresponding Landau solutions are very close, due to having very close values).

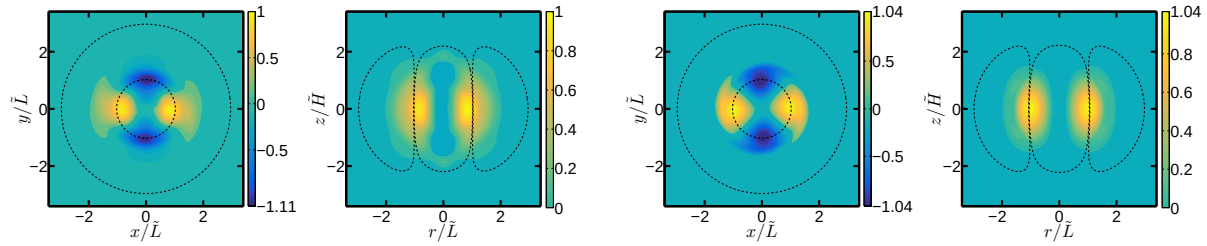

Figure 3.23: (Colour online) As in figure 3.21, but for the group 2 case shown in figure 3.5's panel (b). For the x-y planes here the fixed-z is $z = 0$.

a small parameter space region where $Ro \sim\ 0.02 - 0.05$ and $Bu \sim\ 0.85 - 0.95$. It is easy to show for these vortices that the final and initial unperturbed equilibria remain close, due to having $\sigma = 0$. Furthermore, it was shown in chapter 2 that over a large region of the $Ro - Bu$ parameter space (mainly $Ro < 0$ and $0.5 < Bu < 1.3$), the maximum growth rates of the vortices (mostly anticyclones) are smaller than 50 turnaround time (τ) of the vortex, showing that these vortices as well remain close to their initial unperturbed equilibrium (i.e., over times that are less than or equal to 50 vortex turnaround time). The unlabeled region within figure 2.8 shows where these vortices exist. Here our results are discussed in terms of six different vortex groups and their final equilibria (that are obtained using initial-value calculations). For group 1 vortices, the most unstable eigenmodes' growth rates are fast (i.e. $\sigma > 0.02\,\tau^{-1}$). These vortices have $Bu \gtrsim 1$, and their difference flow is almost anti-symmetric, with respect to the $z = 0$ plane and has $m = 1$ azimuthal wave number (denoted as A1 mode). Our initial-value calculations here show that any perturbations added to the initial vortex state, quickly saturate at small amplitudes, and the initial and final equilibria remain similar to each other. For group 2 vortices ($Bu \lesssim 1$), the most unstable eigenmodes have large growth rates ($\sigma > 0.02\,\tau^{-1}$) again, and the final and initial unperturbed equilibria remain close to each other again. After being perturbed, the flow evolves such that in these cases, the difference flow from the initial state can be demonstrated to be almost symmetric, with respect to the $z = 0$ plane and have $m = 2$ azimuthal wave number (S2 mode). Again our initial-value calculations here show that, any perturbations added to the initial vortex state quickly saturate at small amplitudes (and the initial and final equilibria remain similar to each other). For smaller Bu groups 3a and 3b have final equilibria where neither their core nor their shield remain similar to the core and shield of the unperturbed Gaussian equilibrium. It can be shown that the core of the final equilibrium is near a Gaussian state (but also that the initial shield breaks into multiple smaller satellite vortices, on, or above/below vortex's midplane, showing that the final equilibria are in fact non-Gaussian-like). The final equilibria of these vortices show no dominant symmetries. Furthermore, group 3a shows the anticyclones with two cyclonic satellite vortices that reside on the vortex's midplane ($z = 0$); and group 3b is to demonstrate initial cyclones which have one or two satellite vortices that are above vortex's midplane, and one or two that are below it. Group 4 shows the cases for which vortex can split. For group 5 vortices, the

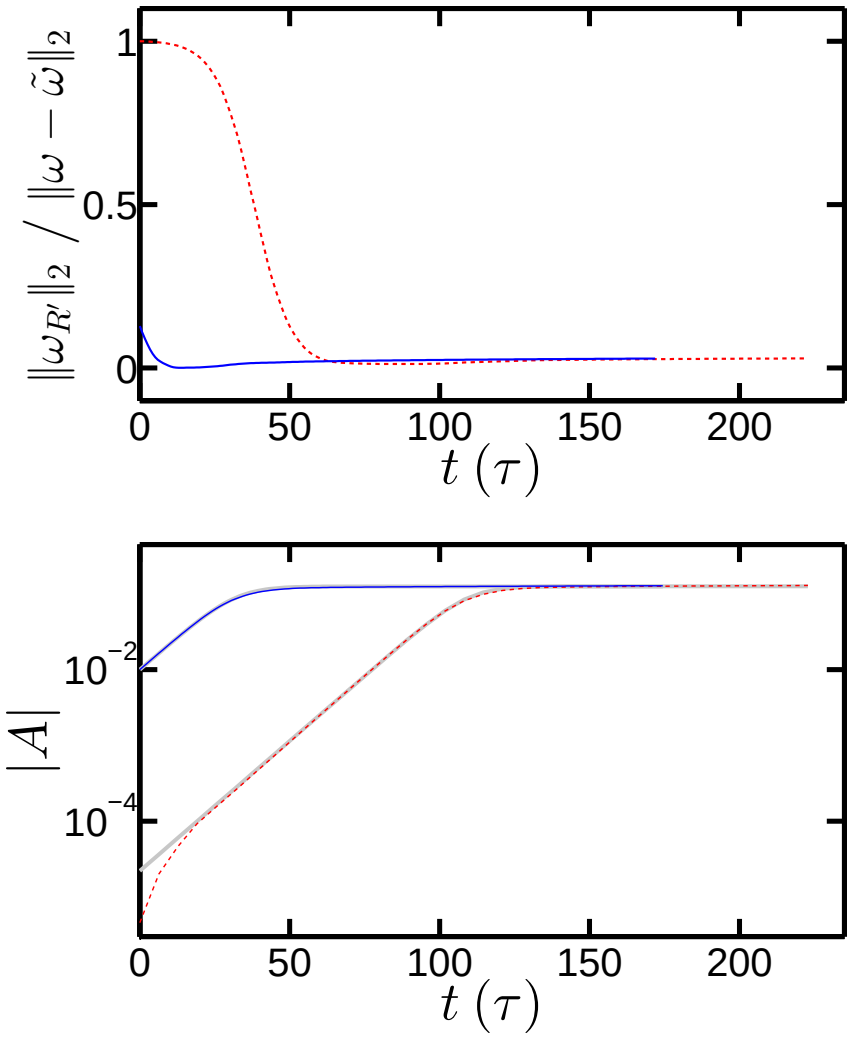

Figure 3.24: (Colour online) As in figure 3.22, but for the case shown in figure 3.23. Different line styles (and colours, in colour version) are for different perturbations, shown in figure 3.4's caption (i.e., that is the perturbation amplitude(s) for the dashed lines (red, in colour) is $A_{IC,N} = 10^{-2.5}$; and for the solid lines (blue, in colour) are $A_{IC,S2} = 10^{-2}$, and $A_{IC,N} = 10^{-2.5}$).

interior of the vortex is statically unstable. The growth rates of the most unstable mode for these anticyclones are much larger (by factors up to several thousand or more) compared to those of the anticyclones outside this region. Group 5's final equilibria have two radially-aligned cores, and the final equilibrium is statically unstable. Due to the large growth rates of these vortices, the perturbations quickly grow and quickly saturate, but the difference flow is confined to the vicinity of the initial vortex's core, and in the shield the flow remains unchanged from the initial equilibrium.

Our quantitative description above of the equilibria in this study is carried out mostly with the enstrophy measures (that is using equilibria's vertical vorticity). The nonlinear flow evolution, however, sometimes can be difficult to describe, specifically in the cases that an analytical closed-form solution does not exist. Focusing on the vortices that have close final and initial unperturbed equilibria, and are statically stable ($N_c^2 \geq 0$), we show that the flow is representable by the Gaussian equilibrium and its dominant symmetry eigenmode (see (3.26)), with any time dependence demonstrated entirely by a complex coefficient $A(t)$ ($A(t)$ is calculated numerically by minimizing the remainder's norm). Numerically computed $A(t)$ values then increase, as remainder norm values decrease, or remain small, such that deviations from the above representation become (or remain) small at quasi-steady state. Furthermore, the numerically calculated $|A(t)|$ values are shown to follow the Landau equation (see equation (3.24)), which can provide a closed-form analytical solution, i.e., $|A_{\mathcal{L}}(t)|$ (see equation (3.25)). Note that this solution can not be calculated *a priori*, given that the Landau coefficient Λ is calculable only after flow reaches quasi-steady state and remains at quasi-steady state.

Our study above can have further implications with regards to the fact that observations of oceanic vortices show that cyclones remain robust for long periods of time (see §3.1). Here we find that despite having fast growth rates, cyclones remain almost unchanged after flow reaches quasi-steady state. Although a fast instability growth rate can destroy a vortex via nonlinear, finite-amplitude instabilities, it also is possible that the perturbations quickly saturate, such that the initial and final equilibria remain close to each other. Our goal here has been to demonstrate the latter, with our results showing that over large regions of our parameter space vortices remain close to their initial unperturbed equilibrium. Nonetheless, it should be noted here that, our explanation for the equilibria's robustness does not require a direct forcing mechanism; it only involves damping of velocity and density far from the initial conditions' position (i.e., see Appendix B).

Appendix A

Definitions of *shield*, *satellites* and *core*

The qualitative definitions for *core*, *shield* and *satellites* were in §2.2, and §3.2. To avoid having the definitions for the above-mentioned regions, from including "large-r" areas (i.e., that is where there is possibly weak vorticity, vorticity filaments, and/or inertia-gravity waves with the boundary damping acting over) that are faraway form the vortex itself, we have to pick "cut-off" values, for the sake of excluding regions which have such "large" radii. For a cyclone, we define the *core* as the contiguous cyclonic region that includes the vortex center where ω is greater than a cut-off value of $0.01\Omega_{max}$, where Ω_{max} is the maximum vorticity of the vortex. The *shield* is defined as the contiguous region where $\omega < 0$ and $|\omega| > 0.01|\Omega_{min}|$, where Ω_{min} is the minimum value of ω in the vortex. The *satellites* have a similar definition to shield, but rather than being contiguous, have multiple regions. Our choice of 0.01 in these cut-off values is arbitrary, but the conclusions about the vortices' attraction basins, and the computed values of the enstrophies S_{core}, S_{shield}, D_s, D_c, F_s, and F_c are insensitive to the exact choice of cut-off value because the ω of the vortices, and the integrands in the definitions (2.27), (2.28), (3.8), (3.9), (3.12), and (3.13) are, by definition and our demonstrations above, very small in regions where ω is near the cut-off value.

Appendix B

Numerical sponge layer, and the energy calculations

To compute unbounded flows in a triply-periodic computational domain, we added an artificial "sponge layer" far from the vortices that were initially centered at the origin. This is accomplished by adding Rayleigh drag and Newtonian cooling terms in the form of $-f_{bd}\boldsymbol{v}$ and $-f_{bd}b$ to the right sides of the momentum and buoyancy equations in (2.1), respectively, where f_{bd} is a function that smoothly varies from zero inside a cylindrical surface to a value of one outside of the cylinder, i.e.,

$$f_{bd} = \left[1 - T(z, L_{z,bd}, s_z)T(r, L_{r,bd}, s_r)\right]/\tau_{bd}, \tag{B.1}$$

where $L_{r,bd}$ is the cylinder diameter, $L_{z,bd}$ is the height, s_r and s_z are the steepness in r and z, τ_{bd} is the damping time scale, $r = (x^2 + y^2)^{1/2}$, and

$$T(\gamma, w, s) \equiv 1/2\left(\tanh\left[(\gamma + w)/s\right] - \tanh\left[(\gamma - w)/s\right]\right), \tag{B.2}$$

is top hat function. T smoothly drops from a value of 1 to 0 for $|\gamma| > w/2$ over a distance s. We use $\tau_{bd} = 20\Delta t$, $s_{r,bd} = 0.01(L_x^2 + L_y^2)^{1/2}$, $L_{r,bd} = 0.85(L_x^2 + L_y^2)^{1/2}$, $s_{z,bd} = 0.01L_z$, and $L_{z,bd} = 0.85L_z$ for the numerical calculations that are carried out here.

For the nonlinear evolution processes that we studied above (i.e., as discussed in chapter 3), energy calculations for the initial conditions, unperturbed initial equilibria ($N_c^2 > 0$), and the differences between the initial and final equilibria for a few representative cases are given in table B.1 of the appendix. These results show that the differences between the initial and final equilibria's energies are due to the kinetic energy KE and potential energy PE damping, before, during, and after vortex evolution, by boundary damping and hyperdissipation. The potential energy damping $\Delta PE_{bd,j}$ is positive for groups 2 and 3, and negative for group 1. As the table indicates, the $\Delta PE_{bd,j}$ has the largest magnitude by far, with the KE hyperviscosity damping (i.e., $\Delta KE_{hv,j}$) also having values that are intermediate. Finally, we note that the kinetic energy boundary damping $\Delta KE_{bd,j}$ and potential energy hyperdiffusivity damping $\Delta PE_{hd,j}$ have the relatively smallest values.

Group	Unperturbed Eq.				Perturbations				Initial Cond.	Final Equilibria		B. D. and Hyperdissipation			
	$\widetilde{Ro}$	$\widetilde{Bu}$	$\frac{\widetilde{KE}}{\widetilde{E}}$	$\frac{\widetilde{PE}}{\widetilde{E}}$	P1	$\log_{10}[A_{IC,P1}]$	P2	$\log_{10}[A_{IC,P2}]$	$\frac{KE_{o,j}-\widetilde{KE}}{\widetilde{E}}$ (10^{-9})	$\frac{KE_{t_F,j}-\widetilde{KE}}{\widetilde{E}}$ (10^{-5})	$\frac{PE_{t_F,j}-\widetilde{PE}}{\widetilde{E}}$ (10^{-5})	$\frac{\Delta PE_{bd,j}}{\widetilde{E}}$ (10^{-5})	$\frac{\Delta KE_{bd,j}}{\widetilde{E}}$ (10^{-8})	$\frac{\Delta PE_{hd,j}}{\widetilde{E}}$ (10^{-11})	$\frac{\Delta KE_{hv,j}}{\widetilde{E}}$ (10^{-6})
1	+0.2	1.3	0.038	−1.038	A1	−2	-	-	3800	−13	10	−2.4	−21	3.6	−9.6
					A1	−2	N	−2.5	4000	−13	10	−2.4	−18	2.2	−8.3
					S2	−2	N	−2.5	4200	−14	10	−3.4	−19	−1.9	−8.4
	+0.1	1.6	0.018	−1.018	N	−2.5	-	-	110	−6.9	5.1	−1.4	−3.7	7.3	−3.6
					A1	−2	N	−2.5	2100	−7.2	5.4	−1.6	−6.3	−5.1	−3.7
2	+0.2	0.75	0.038	−1.038	N	−2.5	-	-	500	86	−53	37	−160	−2.7	−42
					S2	−2	N	−2.5	4200	88	−56	35	−200	−10	−32
	+0.1	0.6	0.018	−1.018	N	−2.5	-	-	140	44	−8.9	38	−21	4.8	−32
					S2	−2	N	−2.5	2100	45	−10	37	−47	−2.4	−20
3a	−0.05	0.15	0.0086	0.9914	N	−2.5	-	-	54	600	−140	510	−620	89	−500
					S2	−3	N	−3.5	12	610	−170	490	−710	−52	−530
3b	+0.45	0.3	0.091	−1.091	A2	−3.5	-	-	9.2	5900	−5000	1400	−14000	−900	−4900
					A3	−3.5	-	-	9.1	5500	−4800	1100	−8800	−3.8	−3900
					A4	−3.5	-	-	9.1	5400	−4600	1300	−8200	7200	−4800
					S2	−3.5	-	-	9.1	5800	−5000	1300	−11000	1.9	−4600
					S3	−3.5	-	-	12	5600	−4900	1100	−5600	−7400	−4200
					S4	−3.5	-	-	9.4	5400	−4700	1100	−7000	17000	−3900
					N	−3.5	-	-	34	5900	−5100	1200	−5700	−38000	−3700
	+0.4	0.45	0.080	−1.080	A1	−2	N	−2.5	8600	1500	−1200	400	−1500	−1.3	−680
					S1	−2	N	−2.5	9500	1500	−1200	400	−1400	180	−720
					S2	−2	N	−2.5	8800	1600	−1300	420	−2800	−32	−780

Table B.1: Energy calculations for several representative cases (of nonlinear evolution): for initial conditions, unperturbed initial equilibria ($N_c^2 > 0$), and the differences between the initial and final equilibria, which are due to the kinetic energy KE and potential energy PE damping, before, during, and after vortex evolution by boundary damping and hyperdissipation. For each group, one or two cases are indicated, with the energy calculations for each case given afterwards. For other vortices similar results (not shown here) are found. The values of KE and PE are normalized, by dividing by the magnitude of the energy $\widetilde{E} = \widetilde{KE} + \widetilde{PE}$ of the unperturbed initial equilibrium (i.e., in the table for all the cases $|\widetilde{KE}/\widetilde{E} + \widetilde{PE}/\widetilde{E}| = 1$). The quantities P1, P2, $A_{IC,P1}$, and $A_{IC,P2}$ in the table, as well as $\widetilde{Ro}$ and $\widetilde{Bu}$, have the same meaning as they do in tables 3.1, 3.2, and 3.3. We note that for these groups, $\widetilde{PE} < 0$, because the equilibria have heavy fluid below light fluid. The 'Initial Cond.' column shows the KE difference between the j^{th} perturbed and unperturbed equilibria $KE_{o,j} - \widetilde{KE}$ ($PE_{o,j} = \widetilde{PE}$, because our white noise does not have density perturbations, and the eigenmodes are m-fold symmetric azimuthally, so they do not have any potential energy). The 'Final Equilibria' column shows the KE and PE difference between the j^{th} final equilibrium at time t_F (where t_F is given in tables 3.1 to 3.3's captions) and the initial unperturbed equilibrium, $KE_{t_F,j} - \widetilde{KE}$ and $PE_{t_F,j} - \widetilde{PE}$. The difference $(KE_{t_F,j} + PE_{t_F,j}) - (KE_{o,j} + PE_{o,j})$ is due to the boundary damping and hyperdissipation. The 'B. D. and Hyperdissipation' column shows the total value, from before to after vortex evolution (i.e., the integral) of these terms, i.e., $\Delta PE_{bd,j}$, $\Delta KE_{bd,j}$, $\Delta PE_{hd,j}$ and $\Delta KE_{hv,j}$, respectively, show the PE boundary damping (can be positive or negative), KE boundary damping (always negative), PE hyperdiffusivity damping (can be positive or negative), and KE hyperviscosity damping (always negative). Furthermore, note that $(KE_{t_F,j}+PE_{t_F,j})-(KE_{o,j}+PE_{o,j}) \simeq \Delta PE_{bd,j} + \Delta KE_{bd,j} + \Delta PE_{hd,j} + \Delta KE_{hv,j}$, where the largest term by far is $\Delta PE_{bd,j}/\widetilde{E}$ (values $O(10^{-2})$, or smaller), with the KE hyperviscosity damping, i.e., $\Delta KE_{hv,j}/\widetilde{E}$ also having intermediate values (i.e., $O(10^{-3})$, or smaller). $\Delta KE_{bd,j}/\widetilde{E}$, and $\Delta PE_{hd,j}/\widetilde{E}$ have values, respectively, of $O(10^{-4})$, or smaller, and $O(10^{-7})$, or smaller.

Appendix C

Eigenmode solver and symmetrizer

We calculate the fastest-growing eigenmodes of the vortices by modifying our initial-value code into a "power method" analogous to the iterative method used for finding the eigenvector of a matrix whose eigenvalue has the greatest absolute value [Press et al. 2007], but we do not use the pre-conditioners developed by Tuckerman & Barkley [1988] to speed-up convergence. Rather, we use a spatial symmetrizer to speed up convergence. The rate of convergence of the power method to the fastest-growing eigenmode depends on the difference between the growth rate of the fastest-growing eigenmode and the growth rate of the second fastest-growing eigenmode. By examining only one spatial symmetry class at a time, we generally increase the difference between the growth rates of the fastest-growing and second fastest-growing eigenmodes, and thereby obtain faster convergence.

The easiest way to limit the solutions of the eigenmode solver to modes that are symmetric or anti-symmetric in z is to limit the initial-value solver used in the power method to those symmetries. Using our spatially triply periodic code, the z-dependence of the solutions are represented here with Fourier modes $e^{i2\pi kz/L_z}$, where $-L_z/2 \leq z < L_z/2$, and where k is an integer. Therefore, it is easy to compute "z-symmetric" solutions, where v_x, v_y, and p are symmetric about $z = 0$ and ρ, b, and v_z are anti-symmetric about $z = 0$ by restricting the former three variables to a cosine series $\cos(2\pi kz/L_z)$ and the latter three variables to a sine series $\sin(2\pi kz/L_z)$. For "z-anti-symmetric" solutions we swap sines with cosines.

When computing solutions in a cylindrical coordinate system (r, ϕ, z) with a spectral code, it is trivial to restrict solutions to have only one value of azimuthal wave number M along with its harmonics. With a spectral method, the velocity, pressure, buoyancy, and density are each represented with a truncated series of basis functions in which the ϕ dependence is expressed in terms of Fourier modes $e^{im\phi}$, and the r dependence is expressed in terms of the eigenmodes of a Sturm-Liouville equation chosen such that the truncated series converges exponentially and such that all of the basis functions are analytic at the origin (see, for example, the spectral expansions used by Matsushima & Marcus [1995] and by Matsushima & Marcus [1997]). Solutions can be forced to be M-fold symmetric in ϕ about the z-axis by restricting the basis functions $e^{im\phi}$ in the spectral expansion to wave numbers m that are divisible by M.

However, because we plan to add Cartesian shear to our future calculations, say, for example to represent the Great Red Spot of Jupiter embedded in a shearing zonal flow, we chose here to compute in Cartesian, rather than cylindrical, coordinates. None the less, it is still possible to force solutions to have only azimuthal wave numbers that are odd, or that are even and divisible by 4, or that are even and not divisible by 4. We can do this efficiently when the grid of collocation points of the Fourier modes in the horizontal direction is made of square cells and the horizontal computational domain is square. In this case, the grid of collocation points is invariant under rotations of 90° around the z-axis. To restrict the solution to azimuthal wave numbers that are even and divisible by 4 – without interpolation (which causes errors), and without dividing or multiplying by r (which is problematic near the origin), we do the following operations after each time step of an initial value code:

1. Compute v_r and v_ϕ at each grid point from the values of v_x and v_y at the grid point.
2. Compute a new value v_ϕ^{NEW} at each grid point (x, y, z) by "averaging" such that

$$v_\phi^{NEW}(x, y, z) \equiv [v_\phi(x, y, z) + v_\phi(-y, x, z) + v_\phi(-x, -y, z) + v_\phi(y, -x, z)]/4. \quad \text{(C.1)}$$

3. Do the same type of averaging to create new values v_r^{NEW}, v_z^{NEW}, ρ^{NEW}, b^{NEW}, and p^{NEW}.
4. Compute v_x^{NEW} and v_y^{NEW} at each grid point from v_r^{NEW} and v_ϕ^{NEW} at the grid point.
5. Compute the flow at the next time using the initial-value solver using the NEW values of all of the variables.

To restrict the solution to azimuthal wave numbers that are even and *not* divisible by 4, we carry out the same procedure as above, but we replace the averaging in (C.1) with

$$v_\phi^{NEW}(x, y, z) \equiv [v_\phi(x, y, z) - v_\phi(-y, x, z) + v_\phi(-x, -y, z) - v_\phi(y, -x, z)]/4. \quad \text{(C.2)}$$

To restrict the solution to azimuthal wave numbers that are odd, we carry out the same procedure as above, but we replace the averaging in (C.1) with

$$v_\phi^{NEW}(x, y, z) \equiv [v_\phi(x, y, z) - v_\phi(-x, -y, z)]/2. \quad \text{(C.3)}$$

Appendix D

Initial-value solver and symmetry calculations

We calculate the dynamics of the vortices using an initial-value solver that is analogous to Barranco & Marcus [2006]'s semi-analytic method for rotating stratified flows. Our initial-value calculations show that all but one of the vortices evolve towards well-defined attracting basins. In order to efficiently describe the remainder (the difference between the flow at any time t and the axisymmetric equilibrium) and its evolution, we define symmetry classes, such that different dominant symmetries indicate different vortex groups. For different perturbations, our calculations show that the vortex attains the same final dominant symmetry, regardless of the initial conditions implemented and therefore, is within the same vortex group (this argument is also valid for the vortices that have different fastest growing eigenmode and dominant symmetries).

Generally, it is easy to separate solutions into parts that are symmetric or anti-symmetric in z (for more details, see Appendix C). Also when computing solutions in cylindrical coordinates (r, ϕ, z) with a spectral code, it is trivial to separate solutions into parts that have only one value of azimuthal wave number M along with its harmonics (see Appendix C).

Note however that to avoid the difficulties of e.g., division by declining r at the origin $(r = 0)$, we choose here to compute in Cartesian, rather than cylindrical, coordinates. None the less, it is still possible to decompose solutions to parts having only azimuthal wave numbers that are odd, or that are even and divisible by 4, or that are even and not divisible by 4 (i.e., the possible symmetry groups in this study). We can do this efficiently when the grid of collocation points (i.e., see §3.2's text) of the Fourier modes in the horizontal direction is made of square cells and the horizontal computational domain is square. In this case, the grid of collocation points is invariant under rotations of 90° about the z-axis. To separate the solution to azimuthal wave numbers, that are odd, and those that are even, we carry out the following operations for a solution obtained from an initial value code:

(i) Compute v_r and v_ϕ at each grid point from the values of v_x and v_y at the grid point.

(ii) Compute the odd part $v_{\phi_{odd}}$ and the even part $v_{\phi_{even}}$ at each grid point (x, y, z) from

v_ϕ and v_ϕ at 180° such that

$$v_{\phi_{odd}} \equiv [v_\phi(x,y,z) - v_\phi(-x,-y,z)]/2, \tag{D.1}$$
$$v_{\phi_{even}} \equiv [v_\phi(x,y,z) + v_\phi(-x,-y,z)]/2, \tag{D.2}$$

where we note that $v_\phi = v_{\phi_{odd}} + v_{\phi_{even}}$.

(iii) Repeat the same sort of calculation to find v_{rodd}, v_{reven}, v_{zodd}, v_{zeven}, ρ_{odd}, ρ_{even}, b_{odd}, b_{even}, p_{odd}, and p_{even}.

(iv) Compute v_{xodd} and $v_{y_{odd}}$ at each grid point from v_{rodd} and $v_{\phi_{odd}}$ at the grid point; and v_{xeven} and $v_{y_{even}}$ from v_{reven} and $v_{\phi_{even}}$.

(v) Do steps (i) to (iv) as required for each solution, and/or time t of the initial-value solver.

To separate the even solution to the azimuthal wave numbers that are *not* divisible by 4 and those that are divisible by 4, we carry out the same procedure as above, but instead of v_ϕ at 180° we use v_ϕ at 90° and replace the calculations in (D.1) and (D.2) with

$$v_{\phi_{even,nd4}} \equiv [v_{\phi_{even}}(x,y,z) - v_{\phi_{even}}(-y,x,z)]/2, \tag{D.3}$$
$$v_{\phi_{even,d4}} \equiv [v_{\phi_{even}}(x,y,z) + v_{\phi_{even}}(-y,x,z)]/2, \tag{D.4}$$

where we note that $v_{\phi_{even}} = v_{\phi_{even,nd4}} + v_{\phi_{even,d4}}$.

Appendix E

Growth rate and symmetry of selected vortex eigenmodes

The growth rate σ and symmetry of the fastest-growing eigenmode of vortices with $\sigma > 0.02$ (τ^{-1}) and $N_c^2 > 0$ shown by symbols in figure 2.8(a) are presented in Table E.1.

Ro	Bu	Symmetry	σ	Ro	Bu	Symmetry	σ
+0.5	0.65	A1	0.26	+0.1	2.0	A1	0.081
+0.5	0.75	S2	0.21	+0.1	2.3	A1	0.091
+0.5	1.0	S2	0.20	+0.05	0.05	A1	1.0
+0.5	1.4	S2	0.18	+0.05	0.1	A1	0.44
+0.5	1.6	S2	0.17	+0.05	0.125	A1	0.28
+0.5	2.0	S2	0.16	+0.05	0.15	A1	0.16
+0.5	2.3	A1	0.16	+0.05	0.25	S2	0.072
+0.45	0.3	A3	1.5	+0.05	0.3	S2	0.067
+0.45	2.3	A1	0.15	+0.05	0.4	S2	0.054
+0.4	0.45	A1	0.4	+0.05	0.6	S2	0.028
+0.4	0.55	A1	0.24	+0.05	1.4	A1	0.040
+0.4	0.65	S2	0.18	+0.05	1.6	A1	0.054
+0.4	0.75	S2	0.17	+0.02	0.02	A1	1.21
+0.4	1.2	S2	0.14	+0.02	0.05	A1	0.58
+0.4	1.4	S2	0.13	+0.02	0.5	S2	0.029
+0.4	1.6	A1	0.13	+0.02	1.3	A1	0.025
+0.35	0.65	S2	0.16	+0.02	1.4	A1	0.034
+0.3	0.25	A1	0.77	+0.02	1.6	A1	0.049
+0.3	0.65	S2	0.13	−0.02	0.05	S2	0.065
+0.25	0.65	S2	0.11	−0.02	0.4	S2	0.029
+0.25	1.4	A1	0.082	−0.02	1.4	A1	0.028
+0.25	1.6	A1	0.092	−0.02	1.6	A1	0.043
+0.2	0.1	A4	2.9	−0.05	0.15	S2	0.053
+0.2	0.15	A2	1.1	−0.05	0.25	S2	0.041
+0.2	0.18	A1	0.76	−0.05	0.3	S2	0.032
+0.2	0.225	A1	0.54	−0.05	1.4	A1	0.024
+0.2	0.26	A1	0.41	−0.1	0.1	S2	0.048
+0.2	0.3	A1	0.29	−0.1	0.15	S2	0.041
+0.2	0.45	S2	0.11	−0.1	1.6	A1	0.032
+0.2	0.55	S2	0.099	−0.15	0.2	S2	0.023
+0.2	0.65	S2	0.089	−0.18	0.15	S2	0.024
+0.2	0.75	S2	0.079	−0.2	1.6	A1	0.023
+0.2	0.85	S2	0.070	−0.2	2.0	A1	0.042
+0.2	1.0	S2	0.058	−0.2	2.3	A1	0.051
+0.2	1.2	A1	0.054	−0.3	1.7	A1	0.021
+0.2	1.4	A1	0.070	−0.35	1.75	A1	0.021
+0.2	1.6	A1	0.081	−0.4	1.8	A1	0.021
+0.2	2.0	A1	0.097	−0.4	2.0	A1	0.028
+0.15	1.0	S2	0.033	−0.4	2.3	A1	0.035
+0.13	1.06	A1	0.02	−0.495	1.5	A1	0.020
+0.1	0.6	S2	0.049	−0.495	1.7	A1	0.029
+0.1	0.8	S2	0.027	−0.495	1.9	A1	0.036
+0.1	1.6	A1	0.062				

Table E.1: The growth rate σ (in units of τ^{-1}) and symmetry of the fastest-growing eigenmode of vortices with $\sigma > 0.02\,\tau^{-1}$ and $N_c^2 > 0$ shown by symbols in figure 2.8(a).

Bibliography

Armi, L. et al. "The history and decay of a Mediterranean salt lens". In: *Nature* 333 (1988), pp. 649–651.

Armi, L. et al. "Two years in the life of a Mediterranean salt lens". In: *J. Phys. Oceanogr.* 19 (1989), pp. 354–370.

Aubert, O. et al. "The universal aspect ratio of vortices in rotating stratfied flows: experiments and observations". In: *J. Fluid Mech.* 706 (2012), pp. 34–45.

Baey, J.-M. & X. Carton. "Vortex multipoles in two-layer rotating shallow-water flows". In: *J. Fluid Mech.* 460 (2002), pp. 151–175.

Barcilon, V. & J. Pedlosky. "On the steady motions produced by a stable stratification in a rapidly rotating fluid". In: *J. Fluid Mech.* 29 (1967), pp. 673–690.

Barge, P. & J. Sommeria. "Did planet formation begin inside persistent gaseous vortices?" In: *Astron. Astrophys.* 295 (1995), pp. L1–L4.

Barranco, J. A. & P. S. Marcus. "A 3D spectral anelastic hydrodynamic code for shearing, stratified flows". In: *J. Comput. Phys.* 219 (2006), pp. 21–46.

— "Three-dimensional vortices in stratified protoplanetary disks". In: *Astrophys. J.* 623 (2005), pp. 1157–1170.

Bashmachnikov, I. et al. "Properties and pathways of Mediterranean water eddies in the Atlantic". In: *Prog. Oceanogr.* 137 (2015), pp. 149–172.

Benilov, E. S. "Instability of quasi-geostrophic vortices in a two-layer ocean with a thin upper layer". In: *J. Fluid Mech.* 475 (2003), pp. 303–331.

— "On the stability of oceanic vortices: A solution to the problem?" In: *Dynam. Atmos. Oceans* 40 (2005), pp. 133–149.

— "Stability of vortices in a two-layer ocean with uniform potential vorticity in the lower layer". In: *J. Fluid Mech.* 502 (2004), pp. 207–232.

— "The effect of ageostrophy on the stability of thin oceanic vortices". In: *Dynam. Atmos. Oceans* 39 (2005), pp. 211–226.

Benilov, E. S. & J. D. Flanagan. "The effect of ageostrophy on the stability of vortices in a two-layer ocean". In: *Ocean Model.* 23 (2008), pp. 49–58.

Benilov, E. S., D. Broutman, & E. P. Kuznetsova. "On the stability of large-amplitude vortices in a continuously stratified fluid on the f-plane". In: *J. Fluid Mech.* 355 (1998), pp. 139–162.

Billant, P., D. G. Dritschel, & J.-M. Chomaz. "Bending and twisting instabilities of columnar elliptical vortices in a rotating strongly stratified fluid". In: *J. Fluid Mech.* 561 (2006), pp. 73–102.

Brunner-Suzuki, A. E. G., M. A. Sundermeyer, & M. P. Lelong. "Vortex stability in a large-scale internal wave shear". In: *J. Phys. Oceanogr.* 42 (2012), pp. 1668–1683.

Budéus, G. et al. "Structure and effects of a long lived vortex in the Greenland Sea". In: *J. Geophys. Res.* 31.L05304 (2004).

Carton, X. "Hydrodynamical modeling of oceanic vortices". In: *Surv. Geophys.* 22 (2001), pp. 179–263.

Carton, X. J. & J. C. McWilliams. "Barotropic and baroclinic instabilities of axisymmetric vortices in a quasigeostrophic model". In: *Elsevier Oceanography Series* 50 (1989), pp. 225–244.

Chang, K.-I. et al. "Circulation and currents in the southwestern East/Japan Sea: Overview and review". In: *Prog. Oceanogr.* 61 (2004), pp. 105–156.

Chelton, D. B., R. A. deSzoeke, & M. G. Schlax. "Geographical variability of the first baroclinic Rossby radius of deformation". In: *J. Phys. Oceanogr.* 28 (1998), pp. 433–460.

Chelton, D. B. et al. "Global observations of large oceanic eddies". In: *Geophys. Res. Lett.* 34.L15606 (2007).

Chelton, D. B., M. G. Schlax, & R. M. Samelson. "Global observations of nonlinear mesoscale eddies". In: *Prog. Oceanogr.* 91 (2011), pp. 167–216.

Cho, J. Y. K. & L. M. Polvani. "The morphogenesis of bands and zonal winds in the atmospheres on the giant outer planets". In: *Science* 273 (1996), pp. 335–337.

D'Asaro, E., S. Walker, & E. Baker. "Structure of two hydrothermal megaplumes". In: *J. Geophys. Res.* 99 (1994), pp. 20361–20373.

de Pater, I. et al. "Persistent rings in and around Jupiters anticyclones – Observations and theory". In: *Icarus* 210 (2010), pp. 742–762.

Dewar, W. K. & P. D. Killworth. "On the stability of oceanic rings". In: *J. Phys. Oceanogr.* 25 (1995), pp. 1467–1487.

Dewar, W. K., P. D. Killworth, & J. R. Blundell. "Primitive-equation instability of wide oceanic rings. Part II: Numerical studies of ring stability". In: *J. Phys. Oceanogr.* 29 (1999), pp. 1744–1758.

Dong, C. et al. "Global heat and salt transports by eddy movement". In: *Nat. Commun.* 5.3294 (2014).

Drazin, P. G. & W. H. Reid. *Hydrodynamic stability.* Cambridge University Press, 2004.

Dritschel, D. G. & M. De La Torre JuáRez. "The instability and breakdown of tall columnar vortices in a quasi-geostrophic fluid". In: *J. Fluid Mech.* 328 (1996), pp. 129–160.

Dritschel, D. G. & W. J. Mckiver. "Effect of Prandtl's ratio on balance in geophysical turbulence". In: *J. Fluid Mech.* 777 (2015), pp. 569–590.

Ertel, H. "Ein neuer hydrodynamischer Wirbelsatz". In: *Meteorol. Z.* 59 (1942), pp. 277–281.

Flierl, G. R. "On the instability of geostrophic vortices". In: *J. Fluid Mech.* 197 (1988), pp. 349–388.

Garate-Lopez, I. et al. “A chaotic long-lived vortex at the southern pole of Venus”. In: *Nat. Geosci.* 6 (2013), pp. 254–257.

Gascard, J.-C. et al. “Long-lived vortices as a mode of deep ventilation in the Greenland Sea”. In: *Nature* 416 (2002), pp. 525–527.

Gent, P. R. & J. C. McWilliams. “The instability of barotropic circular vortices”. In: *Geophys. Astro. Fluid* 35 (1986), pp. 209–233.

Graves, L. P., J. C. McWilliams, & M. T. Montgomery. “Vortex evolution due to straining: A mechanism for dominance of strong, interior anticyclones”. In: *Geophys. Astro. Fluid* 100 (2006), pp. 151–183.

Hassanzadeh, P. & Z. Kuang. “Blocking variability: Arctic Amplification versus Arctic Oscillation”. In: *Geophys. Res. Lett.* 42 (2015), pp. 8586–8595.

Hassanzadeh, P., Z. Kuang, & B. F. Farrell. “Responses of midlatitude blocks and wave amplitude to changes in the meridional temperature gradient in an idealized dry GCM”. In: *Geophys. Res. Lett.* 41 (2014), pp. 5223–5232.

Hassanzadeh, P., P. S. Marcus, & P. Le Gal. “The universal aspect ratio of vortices in rotating stratified flows: theory and simulation”. In: *J. Fluid Mech.* 706 (2012), pp. 46–57.

Hebert, D., N. Oakey, & B. Ruddick. “Evolution of a Mediterranean salt lens: Scalar properties”. In: *J. Phys. Oceanogr.* 20 (1990), pp. 1468–1483.

Helfrich, K. R. & U. Send. “Finite-amplitude evolution of two-layer geostrophic vortices”. In: *J. Fluid Mech.* 197 (1988), pp. 331–348.

Hoskins, B. J., M. E. McIntyre, & A. W. Robertson. “On the use and significance of isentropic potential vorticity maps”. In: *Q. J. Roy. Meteor. Soc.* 111 (1985), pp. 877–946.

Humphreys, Tom & Philip S. Marcus. “Vortex street dynamics: The selection mechanism for the areas and locations of Jupiter’s vortices”. In: *J. Atmos. Sci.* 64 (2007), pp. 1318–1333.

Ikeda, M. “Instability and splitting of mesoscale rings using a two-layer quasi-geostrophic model on an f-plane”. In: *J. Phys. Oceanogr.* 11 (1981), pp. 987–998.

Katsman, C. A. et al. “Stability of multilayer ocean vortices: A parameter study including realistic Gulf stream and Agulhas rings”. In: *J. Phys. Oceanogr.* 33 (2003), pp. 1197–1218.

Killworth, P. D., J. R. Blundell, & W. K. Dewar. “Primitive equation instability of wide oceanic rings. Part I: Linear theory”. In: *J. Phys. Oceanogr.* 27 (1997), pp. 941–962.

Kirillov, O. N. “Singular diffusionless limits of double-diffusive instabilities in magnetohydrodynamics”. In: *P. Roy. Soc. A-Math. Phy.* 473.2205 (2017).

Koszalka, I. et al. “Dynamics of wind-forced coherent anticyclones in the open ocean”. In: *J. Geophys. Res.* 114.C08011 (2009).

Kurian, J. et al. “Eddy properties in the California Current System”. In: *J. Geophys. Res.* 116.C08027 (2011).

Lahaye, N. & V. Zeitlin. “Centrifugal, barotropic and baroclinic instabilities of isolated ageostrophic anticyclones in the two-layer rotating shallow water model and their nonlinear saturation”. In: *J. Fluid Mech.* 762 (2015), pp. 5–34.

Lai, D. Y. & P. L. Richardson. “Distribution and movement of Gulf Stream rings”. In: *J. Phys. Oceanogr.* 7 (1977), pp. 670–683.

Landau, L. D. "On the problem of turbulence". In: *Dokl. Akad. Nauk SSSR* 44 (1944), pp. 339–349.

Lazar, A., A. Stegner, & E. Heifetz. "Inertial instability of intense stratified anticyclones. Part 1. Generalized stability criterion". In: *J. Fluid Mech.* 732 (2013a), pp. 457–484.

Lazar, A. et al. "Inertial instability of intense stratified anticyclones. Part 2. Laboratory experiments". In: *J. Fluid Mech.* 732 (2013b), pp. 485–509.

Lelong, M.-P. & M. A. Sundermeyer. "Geostrophic adjustment of an osolated diapycnal mixing event and its implications for small-scale lateral dispersion". In: *J. Phys. Oceanogr.* 35 (2005), pp. 2352–2367.

Lutjeharms, J. R. E., O. Boebel, & H. T. Rossby. "Agulhas cyclones". In: *Deep-Sea Res. Pt. II* 50 (2003), pp. 13–34.

Mac Low, M.-M. & A. P. Ingersoll. "Merging of vortices in the atmosphere of Jupiter: An analysis of Voyager images". In: *Icarus* 65 (1986), pp. 353–369.

Mahdinia, M. et al. "Stability of three-dimensional Gaussian vortices in an unbounded, rotating, vertically stratified, Boussinesq flow: linear analysis". In: *J. Fluid Mech.* 824 (2017), pp. 97–134.

Marcus, P. S. "Jupiter's Great Red Spot and other vortices". In: *Annu. Rev. Astron. Astr.* 31 (1993), pp. 523–573.

— "Prediction of a global climate change on Jupiter". In: *Nature* 428 (2004), pp. 828–831.

Marcus, P. S. & P. Hassanzadeh. "On the surprising longevity of Jupiter's centuries-old Great Red Spot". In: *APS Meeting Abstracts*. 2014.

Marcus, P. S. et al. "Three-dimensional vortices generated by self-replication in stably stratified rotating shear flows". In: *Phys. Rev. Lett.* 111.084501 (2013).

Marcus, P. S. et al. "Zombie vortex instability. I. A purely hydrodynamic instability to resurrect the dead zones of protoplanetary disks". In: *Astrophys. J.* 808.87 (2015).

Maslowe, S. A. "Critical layers in shear flows". In: *Annu. Rev. Fluid Mech.* 18 (1986), pp. 405–432.

Matsushima, T. & P. S. Marcus. "A spectral method for polar coordinates". In: *J. Comput. Phys.* 120 (1995), pp. 365–374.

— "A spectral method for unbounded domains". In: *J. Comput. Phys.* 137 (1997), pp. 321–345.

McWilliams, J. C. "Submesoscale, coherent vortices in the ocean". In: *Rev. Geophys.* 23 (1985), pp. 165–182.

Meschanov, S. L. & G. I. Shapiro. "A young lens of Red Sea Water in the Arabian Sea". In: *Deep-Sea Res. Pt. I* 45 (1998), pp. 1–13.

Mkhinini, N. et al. "Long-lived mesoscale eddies in the eastern Mediterranean Sea: Analysis of 20 years of AVISO geostrophic velocities". In: *J. Geophys. Res.* 119 (2014), pp. 8603–8626.

Morel, Y. & J. McWilliams. "Evolution of isolated interior vortices in the ocean". In: *J. Phys. Oceanogr.* 27 (1997), pp. 727–748.

Negretti, M. E. & P. Billant. "Stability of a Gaussian pancake vortex in a stratified fluid". In: *J. Fluid Mech.* 718 (2013), pp. 457–480.

Nguyen, H. Y. et al. “Slow quasigeostrophic unstable modes of a lens vortex in a continuously stratified flow”. In: *Geophys. Astro. Fluid* 106 (2012), pp. 305–319.

Olson, D. B. “Rings in the ocean”. In: *Annu. Rev. Earth Pl. Sc.* 19 (1991), pp. 283–311.

O’Neill, M. E., K. A. Emanuel, & G. R. Flierl. “Polar vortex formation in giant-planet atmospheres due to moist convection”. In: *Nature Geosci.* 8 (2015), pp. 523–526.

Ozorio de Almeida, A. M. *Hamiltonian systems: chaos and quantization*. Cambridge University Press, 1988.

Paillet, J. et al. “Dynamics and evolution of a northern meddy”. In: *J. Phys. Oceanogr.* 32 (2002), pp. 55–79.

Perret, G., T. Dubos, & A. Stegner. “How large-scale and cyclogeostrophic barotropic instabilities favor the formation of anticyclonic vortices in the ocean”. In: *J. Phys. Oceanogr.* 41 (2011), pp. 303–328.

Pingree, R. D. & B. Le Cann. “Structure of a meddy (Bobby 92) southeast of the Azores”. In: *Deep-Sea Res. Pt. I* 40 (1993), pp. 2077–2103.

Prater, M. D. & T. B. Sanford. “A meddy off Cape St. Vincent. Part I: Description”. In: *J. Phys. Oceanogr.* 24 (1994), pp. 1572–1586.

Press, W. H. et al. *Numerical recipes: The art of scientific computing*. Cambridge University Press, 2007.

Provenzale, A. “Transport by coherent barotropic vortices”. In: *Annu. Rev. Fluid Mech.* 31 (1999), pp. 55–93.

Smyth, W. D. & J. C. McWilliams. “Instability of an axisymmetric vortex in a stably stratified, rotating environment”. In: *Theor. Comp. Fluid. Dyn.* 11 (1998), pp. 305–322.

Stegner, A. & D. G. Dritschel. “A numerical investigation of the stability of isolated shallow water vortices”. In: *J. Phys. Oceanogr.* 30 (2000), pp. 2562–2573.

Sundermeyer, M. A. & M.-P. Lelong. “Numerical simulations of lateral dispersion by the relaxation of diapycnal mixing events”. In: *J. Phys. Oceanogr.* 35 (2005), pp. 2368–2386.

Sutyrin, G. “Why compensated cold-core rings look stable?” In: *Geophys. Res. Lett.* 42 (2015), pp. 5395–5402.

Tsang, Y.-K. & D. G. Dritschel. “Ellipsoidal vortices in rotating stratified fluids: beyond the quasi-geostrophic approximation”. In: *J. Fluid Mech.* 762 (2015), pp. 196–231.

Tuckerman, L. S. & D. Barkley. “Global bifurcation to traveling waves in axisymmetric convection”. In: *Phys. Rev. Lett.* 61 (1988), pp. 408–411.

Tyrlis, E. & B. J. Hoskins. “Aspects of a Northern hemisphere atmospheric blocking climatology”. In: *J. Atmos. Sci.* 65 (2008), pp. 1638–1652.

Vallis, G. K. *Atmospheric and oceanic fluid dynamics: fundamentals and large-scale circulation*. Cambridge University Press, 2006.

van Heijst, G. J. F. & H. J. H. Clercx. “Laboratory modeling of geophysical vortices”. In: *Annu. Rev. Fluid Mech.* 41 (2009), pp. 143–164.

Yim, E. & P. Billant. “On the mechanism of the Gent-McWilliams instability of a columnar vortex in stratified rotating fluids”. In: *J. Fluid Mech.* 780 (2015), pp. 5–44.

Yim, E., P. Billant, & C. Ménesguen. “Stability of an isolated pancake vortex in continuously stratified-rotating fluids”. In: *J. Fluid Mech.* 801 (2016), pp. 508–553.